Technische Universität Wien
Studienrichtung Vermessungswesen und Geoinformation

DISSERTATION

Precision Target Mensuration in Vision Metrology

ausgeführt zum Zwecke der Erlangung des akademischen Grades eines Doktors der technischen Wissenschaften unter der Leitung von

Professor Clive S. Fraser (BAppSc, MSurvSc, PhD)
Department of Geomatics, Melbourne University
und
O.Univ.Prof. Dipl.-Ing. Dr.techn. Karl Kraus
E122, Institut für Photogrammetrie und Fernerkundung, TU-Wien

eingereicht an der Technischen Universität Wien
Fakultät für Mathematik und Geoinformation

von

Dipl.-Ing. Johannes Otepka
Matrikelnummer 93 26 413
Ottensheimerstraße 64, 4040 Linz

Wien, im Oktober 2004

Acknowledgement

First, I want to thank my girlfriend, Gerhild, as well as both our families for their support. Moreover, I want to thank Professor Karl Kraus and Professor Clive Fraser for supervising my research topic. I also extend my gratitude to both for providing all required resources at their Departments in Vienna and Melbourne.

I also wish to extend special thanks to Harry Hanley and Danny Brizzi for their friendship and for their support, both technical and in regard to accommodation, during my visits to Australia. The very useful mathematical insights from Helmut Kager also deserve special recognition.

Additionally, I want to thank Ute, Tom, Camille, Cronksta, Georg R., Georg V., Gisela, Harrison, Hartwig, Laurie, Matt, Megan, Paul, and Takeshi all of whom are friends in Vienna, Linz and Melbourne. They have made my research time very pleasant and always interesting.

Finally, many thanks to the *Austrian Academy of Sciences* for honouring me with the *DOC* scholarship award. Without the scholarship, both the conduct of the doctoral research and the preparation of this thesis would not have been possible.

Abstract

Digital close-range photogrammetry, commonly referred to as vision metrology (VM), is regularly used as a flexible and highly accurate 3D measurement system. VM's most common applications lie within the manufacturing and precision engineering industries.

Through the use of triangulation combined with specialized targets to mark points of interest, accuracies exceeding 1:100,000 can be achieved with VM. In practical applications, circular targets are used to achieve the highest accuracy. Common types include: retro-reflective targets, which provide a high contrast image with flash photography, and white targets on a black background. Accuracy requirements and varying target reflective properties dictate which type of targeting is most suitable for a particular application.

The precise measurement of targets is one of the main factors within VM and directly influences the ability to achieve high accuracy. Mathematical algorithms are used to determine the centres of imaged targets in 2D space. These 2D centroids are then used in a triangulation process to calculate the target position in 3D space. This computational process assumes that the targets represent perfect points in space. In practice, however, target thickness and target diameter adversely effect this assumption. This can lead to the introduction of error and to incorrect calculation of the desired 3D positions. If the target plane is known, however, the 2D centroids can be corrected for these errors.

A central theme of the thesis is the development of a mathematical model and associated computational scheme for the automatic determination of the surface plane of circular targets. The target plane description is determined in two stages. First, the elliptical target images are analysed in each digital photograph. Then, the information gained is used to calculate the target plane via the method of least-squares estimation. The developed process has been implemented and evaluated in the photogrammetric software package *Australis*.

In addition to the development of the new technique for target plane determination, the research also included an investigation, using two groups of network simulations, of induced systematic errors within the photogrammetric measurement process. The first set of simulations investigated the image error effect on the determined target position in 3D space in instances where the derived image coordinate correction functions were not applied. The second group of simulations were conducted to quantify and assess the distortion induced in the 3D measurement process by curved targets. This aspect is especially relevant for the typical VM application of dimensional inspection of surfaces, where targets are directly affixed to the surfaces of interest.

An important component of the research was to analyse the practical relevance of the developed processes and algorithms. As it turns out, high accuracy application domains can benefit from the outcomes of the research conducted, through the enabling of higher measurement precision. In the case of medium-accuracy VM applications or 3D surface inspection, the new techniques for target plane orientation determination can be employed as part of the surface survey, as well as to assist visually in the interpretation of the 3D measurement results.

Zusammenfassung

Digitale Nahbereichsphotogrammetrie, im Englischen meist als „Vision Metrology“ bezeichnet, wird heutzutage als flexibles und hochgenaues 3D-Meßverfahren in unterschiedlichen industriellen Bereichen verwendet. Durch die Verwendung spezieller Zielmarken ist eine hochgenaue Punktbestimmung markierter Objektpunkte möglich. Die erzielbare Punktgenauigkeit dieser Messmethode liegt bei 1/100.000 der Objektgröße. In diesem Zusammenhang wird der Begriff „Triangulierungsgenauigkeit“ oft verwendet.

Üblicherweise werden für die Signalisierung der Punkte kreisrunde Zielmarken verwendet. Diese erlauben höchste Genauigkeit zu erzielen. Neben Zielmarken aus retro-reflektierendem Material werden auch einfache weiße Marken auf schwarzem Hintergrund benutzt. Die Wahl des Zielmarkenmaterials bzw. -typs richtet sich nach der geforderten Genauigkeit und dem notwendigen Reflektionsgrad der Signale bei der Aufnahme der Bilder.

Die Messgenauigkeit der Zielmarken ist einer der entscheidenden Faktoren für eine hohe Triangulierungsgenauigkeit. Mit Hilfe von speziellen Algorithmen werden die Zentren der Zielmarken im digitalen Bild ermittelt, welche es erlauben die Objektpunkte dreidimensional zu triangulieren. Dabei wird vorausgesetzt, dass Zielmarken „perfekte“ Punkte im Raum darstellen, was aufgrund der Stärke des Markenmaterials und der Größe des Zielmarkendurchmessers nur bedingt der Fall ist. Diese Tatsache führt zu Exzentrizitäten zwischen den Zentren der abgebildeten Zielmarken und ihren tatsächlichen Mittelpunkten. Daraus resultieren Fehler im Berechnungsprozess, welche zu einer verfälschten Raumlage der Punkte führen. Ist die Orientierung der einzelnen Zielmarken bekannt, so können die entsprechenden Exzentrizitäten rechnerisch ermittelt und damit die Raumlage der Punkte korrigiert werden.

Ein zentrales Ziel dieser Arbeit war die Entwicklung mathematischer Formeln und Algorithmen für die automatische Bestimmung der Kreisebenen der Zielmarken. Der dafür entworfene Prozess berechnet diese Ebenen in zwei Phasen. Zuerst wird die elliptische Form der abgebildeten Zielmarken aus den digitalen Bildern extrahiert. Anschließend wird diese Information für die eigentliche Berechnung der Kreisebene verwendet, wobei Ausgleichungsverfahren eingesetzt werden. Der dazu entwickelte Berechnungsprozess wurde in das photogrammetrische Softwarepaket *Australis* implementiert und anhand von praktischen Anwendungen evaluiert.

Im weiteren Verlauf der Arbeit werden die Ergebnisse von Simulationsrechnungen präsentiert, welche den Einfluss von zwei unterschiedlichen Fehlerarten aufzeigen. Der erste Teil der Simulationen untersucht die Auswirkung der oben angeführten Exzentrizität auf die Objektpunkte.

Die zweite Gruppe der Simulationsrechnungen analysiert den Fehlereinfluss von gekrümmten Zielmarken auf den Zielmarkenmessprozess. Dieser Einfluss ist vor allem bei der Vermessung von gewölbten Oberflächen interessant, da hier die Zielmarken direkt auf den zu bestimmenden Oberflächen fixiert werden.

Obwohl bei den vorliegenden Untersuchungen primär theoretische Fragestellungen im Vordergrund stehen, widmet sich ein Teil der Arbeit auch der praktischen Relevanz der entwickelten Prozesse und Algorithmen. Dabei konnte bewiesen werden, dass die Berücksichtigung der Exzentrizitäten entsprechende Genauigkeitsvorteile bei hochgenauen Vermessungen bringt. Zusätzlich werden Vorteile für Oberflächenanalysen sowie Aufgaben mittlerer Genauigkeit aufgezeigt.

Table of Contents

1. Introduction

1.1. Motivation

Photogrammetry has always been one of the author's research interests. In his masters thesis, the author concentrated on digital close-range photogrammetry, thus becoming aware of the high accuracy potential of this surveying method.

Digital close-range photogrammetry, commonly referred to as vision metrology (VM), makes use of circular targets to mark points of interest. After imaging the targets from different points of views, mathematical algorithms are used to determine the centres of imaged targets in 2D space. These 2D centroids are then used to triangulate the target position in 3D space. This computation process assumes that the centre of the imaged target is identical with the projected centre of the circle. Knowledge regarding perspectivity shows that this assumption is not strictly correct. There is a small offset which is universally ignored in today's VM systems because its magnitude is generally insignificant, especially for small targets.

Although this eccentricity is of no importance for medium accuracy applications, it is always unsatisfactory to knowingly introduce systematic errors into the triangulation process. The eccentricity limits the radius of the targets being used, which again limits the achievable accuracy. The main aim of the research has been to overcome these shortcomings by correcting the measured centres for the eccentricity.

1.2. General Aims

Ahn et al. (1999) have reported an eccentricity correction formula using the target orientation. Since the target plane is generally not known, this equation cannot be employed. As it will be shown, however, the target plane can be determined if the shape of the imaged target is extracted from at least two images. Hence, one major aim of the thesis research was to develop an automated target plane determination process, which first accurately extracts the imaged target shape in all digital photographs. Then, the information gained from all images is used to estimate the target orientation, always considering that only a precise target plane description will be subsequently usable.

By employing the target plane determination, it is now possible to correct the aforementioned eccentricity, which should enable higher precision photogrammetric surveys to be conducted, especially in high accuracy VM application domains. However, it will be shown that even medium accuracy applications can benefit from the target plane determination in the case of surface inspection.

Besides the mathematical derivations of the developed process, various simulation results will be reported in this thesis. For example, the distortional effects of the eccentricity on the triangulation process are analysed. Another group of simulations allow investigation of the distortion caused by curved targets of different materials. This will help in the selection of the correct target radius if curved surfaces are inspected. Therefore, the radiometric aspects of different target materials were investigated.

Although the main characteristic of this thesis is its mathematical derivations and theoretical considerations, the outcomes are always evaluated from a practical point of view as well.

1.3. Thesis Structure

All developed algorithms and processes were implemented and evaluated within the photogrammetric software package *Australis* (Photometrix 2004). Consequently, the implementation of algorithms in *Visual C++* was an essential part of this research. As mentioned, however, the main focus was upon mathematical derivations and the design of corresponding algorithms.

At this point, some details about the thesis structure and its chapters will be presented. The following chapter introduces VM. Here, the technology and history of digital close-range photogrammetry is described. Then, in the central chapter of the thesis, the mathematical relationship between a circular target and its perspective image is derived. In Chapter 4, algorithms to extract the shape of imaged targets are reported. Afterwards, results of simulations are presented. These investigate the distortional effect of the eccentricity in the triangulation process. A chapter about simulations of the distortional effect of curved targets then follows. In the second last chapter, an evaluation of the developed processes is made. There, accuracies of the target plane determination within real applications are presented and compared with simulated results. The thesis is concluded with a conclusions chapter with remarks for future research and a description of benefits from the outcomes for practical applications.

2. Vision Metrology

In the early 1980s, optical 3D coordinate measurement systems were introduced in the manufacturing and precision engineering sectors. Film-based photogrammetry and other 3D measuring devices became routine tools for high-accuracy dimensional inspection. Today, digital close-range photogrammetry, digital theodolites and laser trackers are the most commonly employed non-contact measurement methods. The first of these, digital close-range photogrammetry, is commonly referred to as vision metrology or VM in short, and it is regularly used in large-scale industrial manufacturing and engineering. Its flexible vision-based concept combined with new developments such as high-resolution digital cameras and new computational models have made digital close-range photogrammetry a highly-automated, high-precision 3D coordinate measurement technology.

Although there are many potential uses of VM, adoption of the technology by industry has been most pronounced in the automobile, aircraft and aerospace manufactioning sectors, as well as in shipbuilding and construction engineering. Dimensional inspection with VM is carried out to support such requirements as quality assurance, deformation measurement, conformance to design surveys and reverse-engineering

VM strategies employ triangulation to determine three dimensional (3D) object point coordinates. Therefore the geometric principle of images, central projection, is used. Every imaged point defines a three dimensional ray in space. Multiple images with different view angles allow triangulation of the required object feature points, as shown in Figure 2.1.

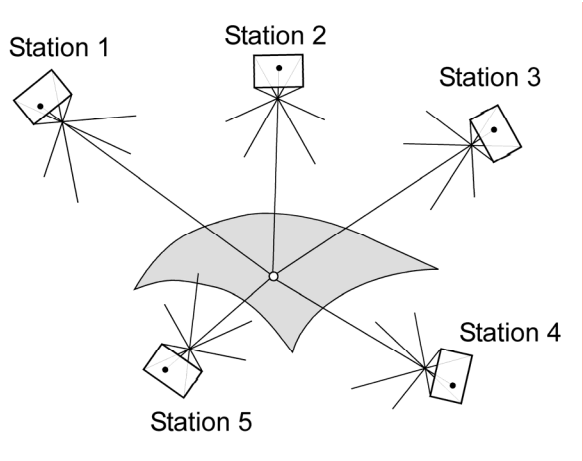

Figure 2.1: Triangulation principle of VM

To achieve high accuracies within the sub-millimetre range, VM strategies make use of special targets to mark points of interest. Various investigations have shown that circular targets deliver the most satisfying results regarding accuracy and automated centroid recognition and mensuration.

For such targets, retro-reflective material is widely used because on-axis illumination of these targets returns many times more light than a normal white textured surface. Using this property, high contrast imagery can be achieved even in bright light conditions, as indicated in Figure 2.2 and Figure 2.3. High contrast images are a key requirement for both high precision and a high level of measurement automation in VM.

Figure 2.2: Normal contrast image of car door

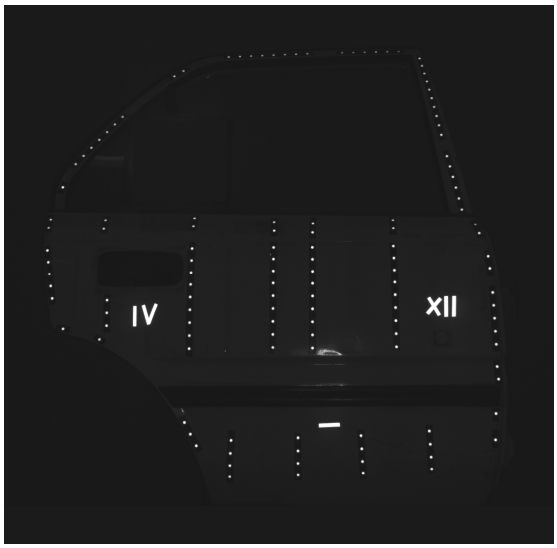

Figure 2.3: High contrast image of car door

Using the radiometric information of high contrast images, and fully utilising the geometric resolution of the camera, accuracies can be greatly increased. Besides retro-reflective signalisation, targets of various different materials are also available, for example plane white targets which can even result in higher accuracy than retro-reflective targets. Complexity with correct exposure, however, has meant that such targets are not often used. Another "target material" is structured light where illuminated spots or patterns are projected onto the surface of the object to be measured (Luhmann 2000, Kraus 1996).

2.1. Concepts of Automated VM

Nowadays, VM offers a high degree of automation, which has opened up a broad field of practical applications. Since results and outcomes of this thesis will improve and enhance the state-of-the-art strategies in VM, a short overview about its concepts will be presented in this section. For more details see e.g. Fraser (1997) or Otepka et al. (2002).

Though there are various strategies for the highly-automated VM measurement process, they all have a first stage in common, namely automated target recognition and measurement. This is the basic requirement for any measurement process which delivers the image coordinates of the target centres in all images.

The actual process which computes the 3D coordinates of the target centres and the exterior orientation (EO) of the camera stations is called bundle adjustment. Since the problem is highly non-linear, approximations of all unknowns have to be given. Whereas an operator can "guess" appropriate values, an automated algorithm has to solve the problem differently. In the early 1990s the idea of an exterior-orientation device (EO device) arose. An EO device is a target group, which defines a coordinate system for the network (Figure 2.4 and Figure 2.5). EO devices are designed for automatic detection and in conjunction with closed-form resection, approximations of the exterior orientation of the camera stations can be carried out.

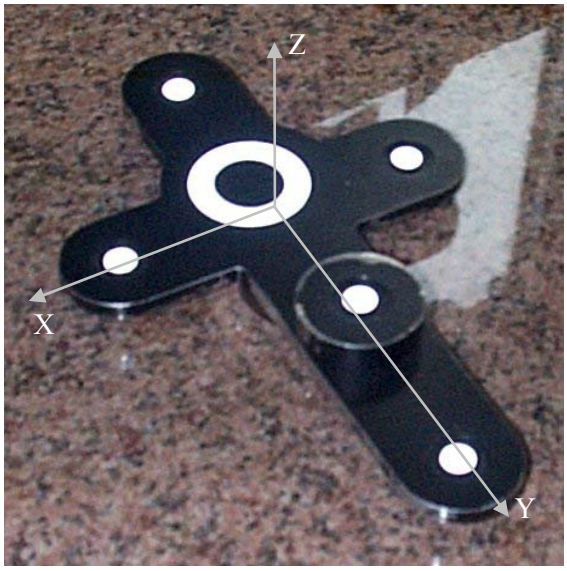

Figure 2.4: AutoBar – EO device in *V-STARS*

Figure 2.5: EO device in *Australis*

Although an EO device can provide EO approximations, there is still one major problem remaining before a triangulation can be performed. The image point correspondence determination was never an issue in manual measurement systems. The operator measured corresponding points in the images with the same point label. In an automated process the computer has measured all image points, but no image point correspondence information is immediately available. There are generally two techniques to solve this problem. First, coded targets can be identified and measured by image processing techniques. Various kinds of coded targets are in use. Their special design allows recognition and invariance of the perspective distortion. However, coded targets are always limited to supporting unique numbers.

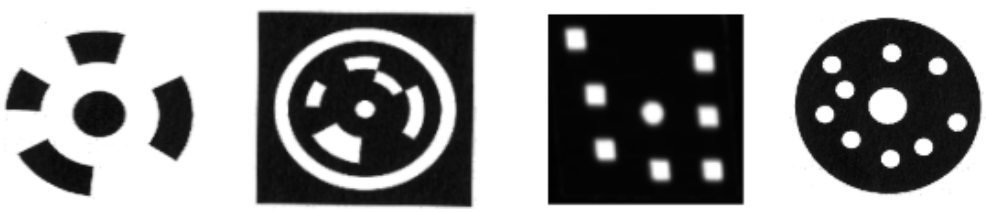

Figure 2.6: Various coded targets from different VM systems (e.g. Luhmann 2000)

As a second technique, epipolar geometry can be employed to locate corresponding image points (e.g. Dold and Maas 1994, Baltsavias and Stallmann 1991, Gruen and Baltsavias 1988). Whereas this technique is not limited to supporting point numbers, correspondence ambiguities can easily arise in the case of only two images or dense arrays of targets. Additionally, the usage of epipolar geometry requires approximations of the exterior orientation of the camera stations, which is problematical if the EO device is not seen in all images. However, using coded targets and epipolar geometry in combination allows the elimination of the disadvantages of each technique.

In summarizing, a fully automated photogrammetric process generally consists of the following stages:

- Automated detection and measuring of targets
- Automatic EO device detection
- Recognition of coded targets
- Solving the point correspondence problem
- Self-Calibrating bundle adjustment of the network

It is obvious that the first stage, detection and measuring of the targets, is the essential process to achieve high accuracy since it delivers the actual observation for the bundle adjustment. Hence, it is well worth investigating and improving state-of-the-art measurement procedures and algorithms, which may lead to better mathematical models and higher accuracy in the overall VM process.

2.2. State-of-the-art Target Measurement

Since the introduction of digital imagery, various algorithms have been developed for measuring targets. In VM, circular retro-reflective targets (Figure 2.7) are widely used because on-axis illumination of these targets returns many times more light than a normal textured surface. Additionally it should be mentioned that the circular shape has turned out to be satisfactory in respect to measuring precision and automatic detection (e.g. Fraser and Shao. 1997).

Figure 2.7: Images of various circular retro-reflective targets

The exact centre of the targets in Figure 2.7 can be computed by centroiding algorithms. Various approaches can be found in the literature, for example template matching, intensity-weighted centroiding and the best-fitting ellipse approach (e.g. Luhmann 2000, Shortis et al. 1994). As it

turns out, the intensity-weighted centroiding approach delivers precise target centres within a short computing time. Consequently this algorithm is mostly used in today's VM systems (e.g. in the *V-STARS* system from *Geodetic Systems Inc.*)

2.2.1. Intensity-Weighted Centroiding

In the following the exact procedure of the intensity-weighted centroiding approach will be described, since this supports the considerations of Section 4.2. Figure 2.8 shows an intensity image of a typical target within a high contrast image. Before the actual centroid is computed, a careful thresholding process is performed whereby pixels are classified as target information or as background noise. This step is responsible for the accuracy of the sub-pixel centroiding process, mainly because the target edge pixels preserve the important geometric information.

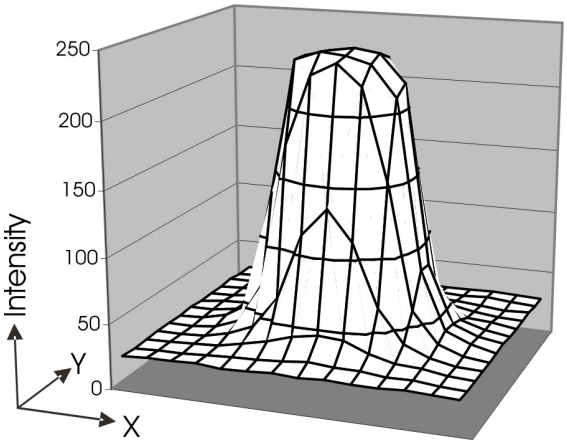

Figure 2.8: Intensity image of a target

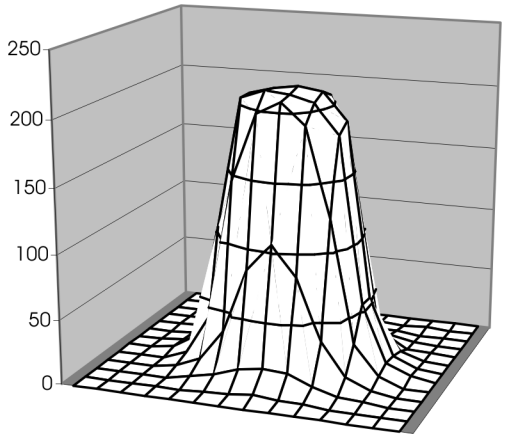

Figure 2.9: Intensity image after background thresholding

The actual thresholding process 'subtracts' a certain background intensity from the intensity image, as can be seen in Figure 2.9. The final centroid coordinates x_0, y_0 are then computed by

$$\begin{pmatrix} x_0 \\ y_0 \end{pmatrix} = \frac{\sum_{i=1}^{n}\sum_{j=1}^{m} g_{ij} \begin{pmatrix} x_i \\ y_j \end{pmatrix}}{\sum_{i=1}^{n}\sum_{j=1}^{m} g_{ij}} \tag{2.1}$$

where x_i, y_i are the pixel coordinates and g_{ij} are the grey values within a window of dimensions n x m covering the target.

By using this technique in conjunction with high contrast imagery, accuracies of 2 to 5 percent of the pixel size are achievable within the bundle adjustment as reported e.g. by Fraser (1997). This impressive precision has been one of the main reasons for the success of VM since the geometrical resolution of early digital cameras was rather poor compared to film-based cameras.

3. Geometric Aspects of Circular Target Measurement

The previous chapter described the possibility of calculating the centre of targets within digital imagery. However, no considerations regarding the shape of the imaged target were made. This aspect will be covered in the following.

As mentioned above, in high-precision VM surveys circular targets are most commonly used. For accuracy investigations, knowledge is required about the perspective properties of circular targets. From viewing directions other than normal to the target surface, a circle appears as an ellipse or in general as a conic section, as indicated by Figure 3.1.

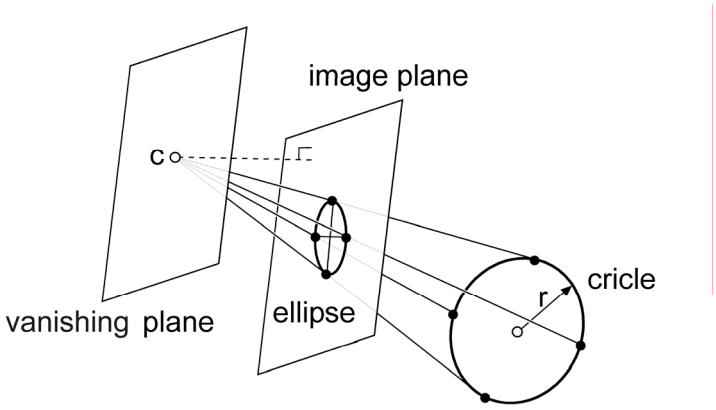

Figure 3.1: Perspective projection of a circle

Parabolic and hyperbolic curves appear only if the circle touches or intersects the “vanishing plane” (the plane parallel to image plane which includes the projection centre). Also, the circle projects as a line if the projection centre is contained by the plane of the circle. In all other cases the circle appears as an ellipse or, if the circle plane is parallel to the image plane, as a circle. Because of the typically small size of the targets employed (see e.g. Figure 2.3) and the limited field of view of the measuring devices, it is unlikely that these circular targets will appear as parabolic or hyperbolic curves. Therefore, only elliptical images will be considered further in this investigation.

In general, VM uses triangulation (angle and spatial direction measurements from different view angels) to determine three-dimensional coordinates of the targeted object points. The exact centres of the imaged ellipses are used for calculating the centre of the circular target. This computation process assumes that the centre of the ellipse is identical with the projected centre of the circle. Knowledge regarding perspectivity shows that this assumption is not strictly correct. There is a small offset which is universally ignored in today’s VM systems because its magnitude is typically insignificant, especially for small targets. This offset is illustrated in Figure 3.2. However, although the resulting image offset is most often ignored, it is nevertheless a systematic error which effects every measurement and which has a potential impact upon achievable VM accuracy. It is possible to correct each observation if the orientation of the circular plane is known (Ahn et al. 1999). The

difficulty in VM is the actual determination of this plane. From any perspective viewpoint there are two circles which project onto the same ellipse, as shown in Figure 3.2.

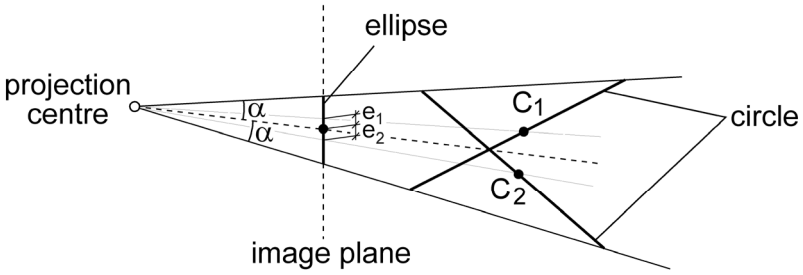

Figure 3.2: Two circles which project onto an identical ellipse, where e_i is the eccentricity between the projected circle centre and the centre of the ellipse.

Since the eccentricity vector is different for those two circles, the correct circular plane has to be known to compensate the image measurement for the offset vector. To solve the ambiguity, the circular target has to be seen from a second direction. There again two circular plane candidates can be determined. From the four candidates, two have to be identical, namely the sought-after circular planes. Kager (1981) has given a mathematical solution for the determination of the circular plane if the equation of the image ellipse is known. In his research, well-defined ellipses in a few images were considered. The case of VM, however, is different. It can be imagined that the ellipse parameters of a small imaged target (<20 pixels in diameter) cannot be so accurately determined. One aim of this research has been to formulate a new mathematical solution which uses, differently to Kager's method, the ellipse information from multiple images to achieve a maximum accuracy solution for the circular signalisation planes within VM imagery.

3.1. Mathematical Model of a 3D Circle and its Perspective Image

Ahn et al. (1999) have given a solution to calculate and correct the eccentricity if the elements of the target circle are given. This mathematical model describes the relationship between the ellipse centre and the circle parameters, considering a certain target-image-configuration. A previously given solution by Kager (1981) has demonstrated how to calculate a 3D circle from a given imaged ellipse by analysing resulting quadratic matrices. However, both solutions are unable to describe the parameters of the imaged conic section explicitly by the circle elements. If such a mathematical model can be found, it is simple to perform an adjustment of indirect observations using multiple images to determine the corresponding circle in space. This model, as described in the following, can also be employed to compute the eccentricity which has to be equal to the solution of Kager and Ahn.

As illustrated in Figure 3.3, a cone is given which touches the circular target and the apex of the cone is positioned at the projection centre **C** of the image. Then the cone is intersected with the image plane. If the resulting section figure can be put into the same mathematical form as an implicit ellipse equation (general polynomial of second degree) the problem is solved.

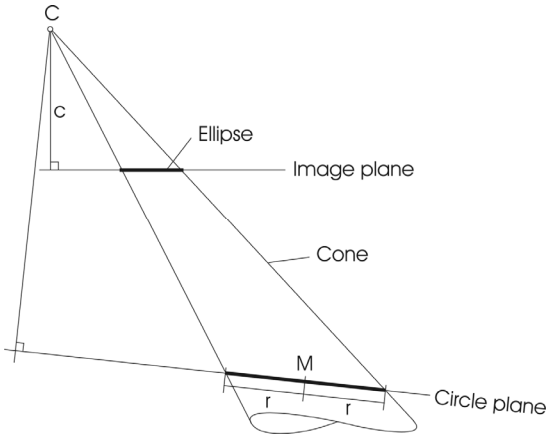

Figure 3.3: View cone which touches the circular target

In object space, the cone can be described by

$$\mathbf{X} = \mathbf{C} + \lambda \cdot r \cdot \left(\cos\alpha \cdot \mathbf{e_1} + \sin\alpha \cdot \mathbf{e_2}\right) + \lambda \cdot (\mathbf{M} - \mathbf{C}) \tag{3.1}$$

where **M** is the centre of the circle, *r* defines the circle radius, $\mathbf{e_1}$ and $\mathbf{e_2}$ are arbitrary orthogonal unit vectors within the circle plane and λ and α are the cone parameters. To transform the cone into image space the well-known collinearity condition is used.

$$\mathbf{x} = \begin{pmatrix} x \\ y \\ -c \end{pmatrix} = \mathbf{R} \cdot \left(\mathbf{X} - \mathbf{C}\right) = \begin{pmatrix} \mathbf{R}_1 \\ \mathbf{R}_2 \\ \mathbf{R}_3 \end{pmatrix} \cdot \left(\mathbf{X} - \mathbf{C}\right) = \begin{pmatrix} R_{11} & R_{12} & R_{13} \\ R_{21} & R_{22} & R_{23} \\ R_{31} & R_{32} & R_{33} \end{pmatrix} \cdot \begin{pmatrix} X_x - C_x \\ X_y - C_y \\ X_z - C_z \end{pmatrix} \tag{3.2}$$

where x and y are the images coordinates, c is the focal length, **R** is the rotation matrix and **X** are coordinates in object space. Hence, the cone in image space follow as

$$\mathbf{x} = \lambda \cdot r \cdot \mathbf{R} \cdot \left(\cos\alpha \cdot \mathbf{e_1} + \sin\alpha \cdot \mathbf{e_2}\right) + \lambda \cdot \mathbf{R} \cdot (\mathbf{M} - \mathbf{C}) \tag{3.3}$$

The intersection of equation (3.3) with the image plane is simple. The plane is defined by $z = -c$. Thus, λ can be described by

$$\lambda = -\frac{c}{\mathbf{R}_3 \cdot (r \cdot \cos\alpha \cdot \mathbf{e_1} + r \cdot \sin\alpha \cdot \mathbf{e_2} + \mathbf{M} - \mathbf{C})} \tag{3.4}$$

and the coordinates of the intersection figure follow as

$$\begin{aligned} x &= -c\frac{\mathbf{R}_1 \cdot (r \cdot \cos\alpha \cdot \mathbf{e_1} + r \cdot \sin\alpha \cdot \mathbf{e_2} + \mathbf{M} - \mathbf{C})}{\mathbf{R}_3 \cdot (r \cdot \cos\alpha \cdot \mathbf{e_1} + r \cdot \sin\alpha \cdot \mathbf{e_2} + \mathbf{M} - \mathbf{C})} = -c\frac{\mathbf{R}_1 \cdot \mathbf{g}}{\mathbf{R}_3 \cdot \mathbf{g}} \\ y &= -c\frac{\mathbf{R}_2 \cdot (r \cdot \cos\alpha \cdot \mathbf{e_1} + r \cdot \sin\alpha \cdot \mathbf{e_2} + \mathbf{M} - \mathbf{C})}{\mathbf{R}_3 \cdot (r \cdot \cos\alpha \cdot \mathbf{e_1} + r \cdot \sin\alpha \cdot \mathbf{e_2} + \mathbf{M} - \mathbf{C})} = -c\frac{\mathbf{R}_2 \cdot \mathbf{g}}{\mathbf{R}_3 \cdot \mathbf{g}} \end{aligned} \tag{3.5}$$

If the equations (3.5) can be transformed so that the parameter α gets eliminated, the problem is solved. First the equations are transformed as shown below:

$$\begin{aligned} -\mathbf{R}_3 \cdot \mathbf{g} \cdot x &= c \cdot \mathbf{R}_1 \cdot \mathbf{g} \\ -\mathbf{R}_3 \cdot \mathbf{g} \cdot y &= c \cdot \mathbf{R}_2 \cdot \mathbf{g} \end{aligned} \Rightarrow \tag{3.6}$$

$$\begin{aligned} r\cos\alpha\left(-x\cdot\mathbf{R}_3\cdot\mathbf{e_1}-c\cdot\mathbf{R}_1\cdot\mathbf{e_1}\right)+r\sin\alpha\left(-x\cdot\mathbf{R}_3\cdot\mathbf{e_2}-c\cdot\mathbf{R}_1\cdot\mathbf{e_2}\right)&=(x\cdot\mathbf{R}_3+c\cdot\mathbf{R}_1)\cdot(\mathbf{M}-\mathbf{C}) \\ r\cos\alpha\left(-y\cdot\mathbf{R}_3\cdot\mathbf{e_1}-c\cdot\mathbf{R}_2\cdot\mathbf{e_1}\right)+r\sin\alpha\left(-y\cdot\mathbf{R}_3\cdot\mathbf{e_2}-c\cdot\mathbf{R}_2\cdot\mathbf{e_2}\right)&=(y\cdot\mathbf{R}_3+c\cdot\mathbf{R}_2)\cdot(\mathbf{M}-\mathbf{C}) \end{aligned} \tag{3.7}$$

equation (3.7) can also be described as

$$\begin{aligned} r\cos\alpha\cdot x_1 + r\sin\alpha\cdot y_1 &= c_1 \\ r\cos\alpha\cdot x_2 + r\sin\alpha\cdot y_2 &= c_2 \end{aligned} \quad \begin{vmatrix} \cdot x_2 \\ \cdot -x_1 \end{vmatrix} + \quad \begin{vmatrix} \cdot -y_2 \\ \cdot y_1 \end{vmatrix} + \tag{3.8}$$

or, after the proposed transformations, the following two equations are generated:

$$\begin{aligned} r\sin\alpha\left(y_1x_2-y_2x_1\right) &= c_1x_2-c_2x_1 \\ r\cos\alpha\left(y_1x_2-y_2x_1\right) &= c_2y_1-c_2y_2 \end{aligned} \quad \begin{vmatrix} 2 \\ 2 \end{vmatrix} + \tag{3.9}$$

After squaring and adding equations (3.9) the final sought-after equation without an α term is found:

$$r^2\left(y_1x_2-y_2x_1\right)^2=\left(c_1x_2-c_2x_1\right)^2+\left(c_2y_1-c_2y_2\right)^2 \tag{3.10}$$

This equation can be transformed into a general polynomial of the second degree in x and y as

$$a_1\cdot x^2+a_2\cdot xy+a_3\cdot y^2+a_4\cdot x+a_5\cdot y-1=0 \tag{3.11}$$

where the corresponding coefficients are

$$\begin{aligned} a_1 &= \frac{r^2\cdot i_1^{\,2}-j_1^{\,2}-k_1^{\,2}}{d} \\ a_2 &= 2\frac{r^2\cdot i_1\cdot i_2-j_1\cdot j_2-k_1\cdot k_2}{d} \\ a_3 &= \frac{r^2\cdot i_2^{\,2}-j_2^{\,2}-k_2^{\,2}}{d} \\ a_4 &= 2\cdot c\frac{j_1\cdot j_3+k_1\cdot k_3-r^2\cdot i_1\cdot i_3}{d} \\ a_5 &= 2\cdot c\frac{j_2\cdot j_3+k_2\cdot k_3-r^2\cdot i_2\cdot i_3}{d} \end{aligned} \tag{3.12}$$

using the following auxiliary variables

$$d=c^2\left(j_3^{\,2}+k_3^{\,2}-r^2\cdot i_3^{\,2}\right) \tag{3.13}$$

$$\begin{aligned} \mathbf{i} &= \begin{pmatrix} i_1 & i_2 & i_3 \end{pmatrix}^T = \left(\mathbf{R}\cdot\mathbf{e}_1\right)\times\left(\mathbf{R}\cdot\mathbf{e_2}\right)=\mathbf{R}\cdot\left(\mathbf{e_1}\times\mathbf{e_2}\right)=\mathbf{R}\cdot\mathbf{n} \\ \mathbf{j} &= \begin{pmatrix} j_1 & j_2 & j_3 \end{pmatrix}^T = \left(\mathbf{R}\cdot\mathbf{e}_1\right)\times\left(\mathbf{R}\cdot\left(\mathbf{C}-\mathbf{M}\right)\right)=\mathbf{R}\cdot\left(\mathbf{e}_1\times\left(\mathbf{C}-\mathbf{M}\right)\right)=\mathbf{R}\cdot\left(\mathbf{e}_1\times\mathbf{v}\right) \\ \mathbf{k} &= \begin{pmatrix} k_1 & k_2 & k_3 \end{pmatrix}^T = \left(\mathbf{R}\cdot\mathbf{e}_2\right)\times\left(\mathbf{R}\cdot\left(\mathbf{C}-\mathbf{M}\right)\right)=\mathbf{R}\cdot\left(\mathbf{e}_2\times\left(\mathbf{C}-\mathbf{M}\right)\right)=\mathbf{R}\cdot\left(\mathbf{e}_2\times\mathbf{v}\right) \end{aligned} \tag{3.14}$$

It is permitted to use the distributive law in equations (3.14) since **R** is a rotation matrix.

While infinite sets of the vectors $\mathbf{e_1}$ and $\mathbf{e_2}$ exist to describe the same circle in space, the polynomial coefficients (3.12) have to be invariant regarding the selected vector set. Since the normal vector of the circle plane (**n** in object space; **i** in image space) is invariant to $\mathbf{e_1}$ and $\mathbf{e_2}$ as well, it has to be possible to find a description of equations (3.12) using only the vectors **i** and **v** (= **C** - **M**). It is noticeable that the elements of the vectors **j** and **k** always appear combined and in quadratic form within the coefficients. If these 6 quadratic sums can be expressed by **i** and **v** the problem is solved. For the following derivation the unit vectors $\mathbf{e_1}$ and $\mathbf{e_2}$ in image space are defined by using rotation matrices as

$$\begin{aligned}\overline{\mathbf{e_1}} &= \mathbf{RX}_\alpha\mathbf{RY}_\beta\mathbf{RZ}_\gamma \cdot \begin{pmatrix}1\\0\\0\end{pmatrix} = \begin{pmatrix}\cos\beta\cos\gamma\\ \sin\alpha\sin\beta\cos\gamma-\cos\alpha\sin\gamma\\ \cos\alpha\sin\beta\cos\gamma+\sin\alpha\sin\gamma\end{pmatrix}\\ \overline{\mathbf{e}_2} &= \mathbf{RX}_\alpha\mathbf{RY}_\beta\mathbf{RZ}_{\gamma+\frac{\pi}{2}} \cdot \begin{pmatrix}1\\0\\0\end{pmatrix} = \begin{pmatrix}-\cos\beta\sin\gamma\\ -\sin\alpha\sin\beta\sin\gamma-\cos\alpha\cos\gamma\\ -\cos\alpha\sin\beta\sin\gamma+\sin\alpha\cos\gamma\end{pmatrix}\end{aligned} \tag{3.15}$$

where γ describes the degrees of freedom within the circle plane and **RX**, **RY** and **RZ** are rotation matrices, as defined by

$$\begin{aligned}\mathbf{RX}_\alpha &= \begin{pmatrix}1 & 0 & 0\\ 0 & \cos\alpha & \sin\alpha\\ 0 & -\sin\alpha & \cos\alpha\end{pmatrix} \quad \mathbf{RY}_\beta = \begin{pmatrix}\cos\beta & 0 & -\sin\beta\\ 0 & 1 & 0\\ \sin\beta & 0 & \cos\beta\end{pmatrix}\\ \mathbf{RZ}_\gamma &= \begin{pmatrix}\cos\gamma & \sin\gamma & 0\\ -\sin\gamma & \cos\gamma & 0\\ 0 & 0 & 1\end{pmatrix}\end{aligned} \tag{3.16}$$

Substituting vectors $\overline{\mathbf{e_1}}$ and $\overline{\mathbf{e_2}}$ in equations (3.14) it follows that

$$\mathbf{i} = \overline{\mathbf{e_1}} \times \overline{\mathbf{e_2}} = \begin{pmatrix}\sin\beta\\ -\sin\alpha\cos\beta\\ -\cos\alpha\cos\beta\end{pmatrix} \tag{3.17}$$

$$\begin{aligned}\mathbf{j} &= \overline{\mathbf{e_1}} \times (\mathbf{R}\cdot\mathbf{v}) = \overline{\mathbf{e_1}} \times \overline{\mathbf{v}} =\\ &= \begin{pmatrix}\overline{v_3}(\sin\alpha\sin\beta\cos\gamma-\cos\alpha\sin\gamma)+\overline{v_2}(-\cos\alpha\sin\beta\cos\gamma-\sin\alpha\sin\gamma)\\ \overline{v_1}(\cos\alpha\sin\beta\cos\gamma+\sin\alpha\sin\gamma)-\overline{v_3}\cos\beta\cos\gamma\\ \overline{v_1}(-\sin\alpha\sin\beta\cos\gamma+\cos\alpha\sin\gamma)+\overline{v_2}\cos\beta\cos\gamma\end{pmatrix}\end{aligned} \tag{3.18}$$

$$\begin{aligned}\mathbf{k} &= \overline{\mathbf{e_2}} \times (\mathbf{R}\cdot\mathbf{v}) = \overline{\mathbf{e_2}} \times \overline{\mathbf{v}} =\\ &= \begin{pmatrix}\overline{v_3}(-\sin\alpha\sin\beta\sin\gamma-\cos\alpha\cos\gamma)+\overline{v_2}(\cos\alpha\sin\beta\sin\gamma-\sin\alpha\cos\gamma)\\ \overline{v_1}(-\cos\alpha\sin\beta\sin\gamma+\sin\alpha\cos\gamma)+\overline{v_3}\cos\beta\sin\gamma\\ \overline{v_1}(\sin\alpha\sin\beta\sin\gamma+\cos\alpha\cos\gamma)-\overline{v_3}\cos\beta\sin\gamma\end{pmatrix}\end{aligned} \tag{3.19}$$

where it can be seen that the normal vector **i** does not depend on γ. However, the vectors **j** and **k** still contain γ terms. The next step is to compute the aforementioned quadratic sums using equation (3.18) and (3.19). As an example the following sum will be fully derived.

$$j_1^2 + k_1^2 = \overline{v_3}^2 \left(\sin^2\beta + \cos^2\alpha\cos^2\beta\right) + \overline{v_2}^2 (1 - \cos^2\alpha\cos^2\beta) + 2\overline{v_3}\,\overline{v_2}\cos\alpha\sin\alpha\cos^2\beta \quad (3.20)$$

As expected all γ terms are eliminated. Now, the angle terms can be substituted by the elements of the vector **i** (3.17) which results in

$$\begin{aligned} j_1^2 + k_1^2 &= \overline{v_3}^2 \left(i_1^2 + i_3^2\right) + \overline{v_2}^2 (1 - i_3^2) + 2\overline{v_3}\,\overline{v_2}\, i_2 i_3 = \\ &= \left(\overline{v_2} i_2 + \overline{v_3} i_3\right)^2 + i_1^2 \left(\overline{v_2}^2 + \overline{v_3}^2\right) \end{aligned} \quad (3.21)$$

considering that **i** is a unit vector. This substitution can also be carried out for the other five remaining quadratic sums. The final results are listed below.

$$\begin{aligned} j_2^2 + k_2^2 &= -\left(\overline{v_1} i_3 - \overline{v_3} i_1\right)^2 + \overline{v_1}^2 + \overline{v_3}^2 \\ j_3^2 + k_3^2 &= -\left(\overline{v_2} i_1 - \overline{v_1} i_2\right)^2 + \overline{v_1}^2 + \overline{v_2}^2 \\ j_1 j_2 + k_1 k_2 &= \left(\overline{v_3} i_1 - \overline{v_1} i_3\right)\left(\overline{v_3} i_2 - \overline{v_2} i_3\right) - \overline{v_1}\,\overline{v_2} \\ j_1 j_3 + k_1 k_3 &= \overline{v_1}\,\overline{v_3}\left(i_2^2 - 1\right) + \overline{v_2}\left(-\overline{v_1} i_2 i_3 + \overline{v_2} i_1 i_3 - \overline{v_3} i_1 i_2\right) \\ j_2 j_3 + k_2 k_3 &= \left(\overline{v_1} i_3 - \overline{v_3} i_1\right)\left(\overline{v_1} i_2 - \overline{v_2} i_1\right) - \overline{v_2}\,\overline{v_3} \end{aligned} \quad (3.22)$$

Using equation (3.22) the polynomial coefficients (3.12) can be finally described using *r*, *c*, **i** and **v** as parameters only.

$$\begin{aligned} a_1 &= \frac{r^2 \cdot i_1^2 - \left(\overline{v_2} i_2 + \overline{v_3} i_3\right)^2 - i_1^2 \left(\overline{v_2}^2 + \overline{v_3}^2\right)}{d} \\ a_2 &= 2\frac{r^2 \cdot i_1 \cdot i_2 - \left(\overline{v_3} i_1 - \overline{v_1} i_3\right)\left(\overline{v_3} i_2 - \overline{v_2} i_3\right) + \overline{v_1}\,\overline{v_2}}{d} \\ a_3 &= \frac{r^2 \cdot i_2^2 + \left(\overline{v_1} i_3 - \overline{v_3} i_1\right)^2 - \overline{v_1}^2 - \overline{v_3}^2}{d} \\ a_4 &= 2 \cdot c\frac{\overline{v_1}\,\overline{v_3}\left(i_2^2 - 1\right) + \overline{v_2}\left(-\overline{v_1} i_2 i_3 + \overline{v_2} i_1 i_3 - \overline{v_3} i_1 i_2\right) - r^2 \cdot i_1 \cdot i_3}{d} \\ a_5 &= 2 \cdot c\frac{\left(\overline{v_1} i_3 - \overline{v_3} i_1\right)\left(\overline{v_1} i_2 - \overline{v_2} i_1\right) - \overline{v_2}\,\overline{v_3} - r^2 \cdot i_2 \cdot i_3}{d} \end{aligned} \quad (3.23)$$

where *d* is

$$d = c^2\left(-\left(\overline{v_2} i_1 - \overline{v_1} i_2\right)^2 + \overline{v_1}^2 + \overline{v_2}^2 - r^2 \cdot i_3^2\right) \quad (3.24)$$

The derivation above proves that the perspective image of a circle is a general polynomial of the second degree which describes a conic section. This does not come as a surprise since we were

intersecting a cone with a plane. For completnees it should be mentioned that this is also valid for oblique cones as no limitations were set on the view cone at the beginning.

The conversion of the implicit ellipse equation (3.11) to its parametric from is described in Appendix A1. This allows computation of the centre coordinates of the ellipse. By projecting the circle centre **M** into the image the eccentricity vector can be calculated. Using discreet values the derived model was compared with the formula given by Ahn et al. (1999) and Kager (1981). All three methods turned out to yield identical results.

3.2. Special Geometric Aspects of Retro-Reflective Targets

So far, the geometric aspects of circular target measurement have been discussed in general terms. The eccentricity appears at any circular target independent of its material and pointing method (total stations, laser tracker, etc.). For retro-reflective targets, however, additional offsets appear and these must be taken into account. To gain an understanding of these offsets the structure of a retro-reflective target needs to be known. This structure is illustrated in Figure 3.4.

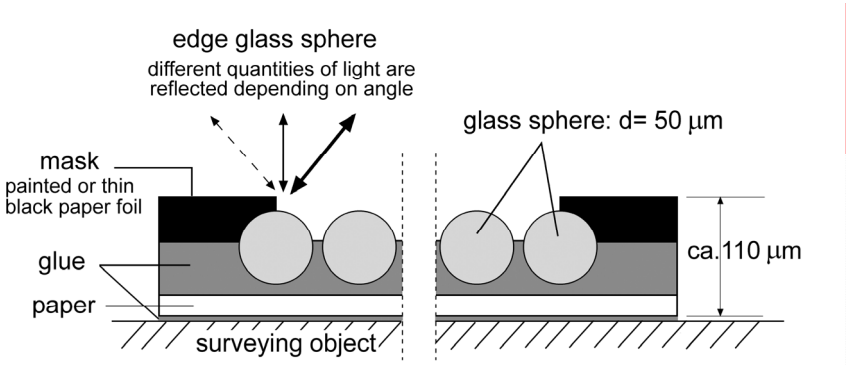

Figure 3.4: Cross section of retro-reflective target (Zumbrunn 1995)

Small glass spheres, usually of 50-100 µm diameter, glued onto a base paper are responsible for reflecting light rays back in the same direction from which they came, with very little scattering. To create circular targets, a circular mask is painted or glued (thin black foil) onto the retro-reflective material. The resulting sharp-edged circular target delivers high contrast images if it is illuminated by a strobe light positioned very close to the camera's optical axis. The visible edge of the glass spheres changes if the target is viewed from different angles. In the case of Figure 3.4 the apparent target centre is shifted to the right if it is viewed from the left, and vice versa. This shift is only caused by the changing degree of light reflection of edge spheres (compare Figure 6.10). If the edge mask is thicker than about 10 µm, additional shadowing effects will further affect the shift. Zumbrunn (1995) has shown that this error effect is independent of target size and pointing method. He estimated the shift in object space to

$$s[\mu m] \approx 0.8 \cdot \alpha[^\circ] \tag{3.25}$$

where α is the angle between the target plane normal and the direction from the target to the projection centre. The direction of the shift is described as transverse to the line of sight and points towards the more distant target edge. Since Zumbrunn was employing a video-theodolite for his investigations, his derived direction of the shift is not valid for Photogrammetry, as shown below.

To analyse the shift direction a virtual target is defined where glass spheres are positioned along the target edge, since these spheres are responsible for the centre shift. Viewed from the top, one hemisphere of each sphere is visible whereas the other half is covered from the mask, as indicated in Figure 3.5.

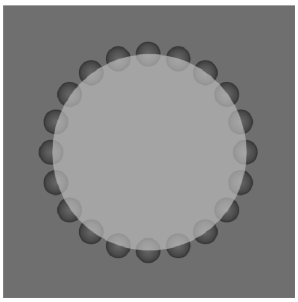

Figure 3.5: Top view of virtual target with transparent target mask

If this target is now viewed from different directions (Figure 3.6), some spheres are more or less visible than before. This is exactly the effect Zumbrunn described in 1995 since the visible sphere area is responsible for the degree of light reflection.

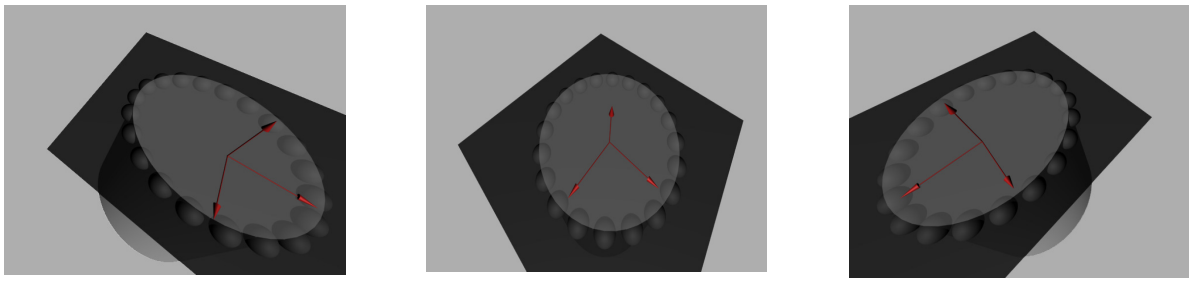

Figure 3.6: Virtual target viewed from different directions

Within the image the shift can be rigorously described by

$$\mathbf{s} = \begin{pmatrix} \overline{x_S} \\ \overline{y_S} \end{pmatrix} - \begin{pmatrix} x_E \\ y_E \end{pmatrix} \tag{3.26}$$

$$\overline{x_s} = \frac{\sum_S \bar{x} \cdot A_v}{\sum_S A_v}$$
$$\overline{y_s} = \frac{\sum_S \bar{y} \cdot A_v}{\sum_S A_v} \qquad (3.27)$$

where x_E and y_E are the centre coordinates of the ellipse, A_v is the visible area of a glass sphere and $\bar{x}$ and $\bar{y}$ are the corresponding area centre coordinates. However, this equation cannot be employed in practise because the real ellipse centre is not known and the glass spheres are glued in irregular dense patterns on to the carrier material. Hence, an approximation of the shift direction is proposed using the following geometric considerations. We define a cylinder which touches the mask edge and its axis is normal to the target plane (Figure 3.7). From now on this cylinder be will called a target cylinder.

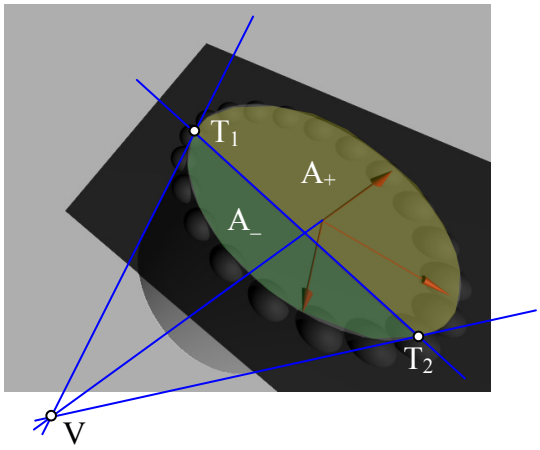

Figure 3.7: Virtual target and corresponding target cylinder

The two outline generatrix of the target cylinder intersect in the vanishing point V (parallel lines in space project perspectively onto lines that on extension intersect at a single point in the image plane called vanishing point or point at infinity) and touch the target ellipse at the points T_1 and T_2. A line between the two points separates the target ellipse into two areas A_+ and A_-. Within A_- less of the glass spheres are visible whereas A_+ will reflect more than half of the light. Considering that VM uses small targets, the scale of all spheres will be nearly the same within the image. Consequently the shift direction will approximately point from the centre of A_- to the centre of A_+. The line which contain the two centres must also contain the ellipse centre. This leads to the conclusion that the shift direction maybe estimated by a line from the vanishing point V to the ellipse centre. This line represents the image of the target normal positioned at the ellipse centre or the target centre, considering that this eccentricity is small, which will have even minor impact onto the image of the target normal. Employing all described approximations and equation (3.25) the shift can be computed by

$$\mathbf{x}_1 = \begin{pmatrix} x_1 \\ y_1 \\ -c \end{pmatrix} = \mathbf{R} \cdot (\mathbf{X} - \mathbf{C})$$

$$\mathbf{x}_2 = \begin{pmatrix} x_2 \\ y_2 \\ -c \end{pmatrix} = \mathbf{R} \cdot (\mathbf{X} + 0.8 \cdot \alpha \cdot \mathbf{n} - \mathbf{C}) = \mathbf{R} \cdot \left(\mathbf{X} + 0.8 \cdot \arccos\left(\frac{(\mathbf{C} - \mathbf{X}) \cdot \mathbf{n}}{|\mathbf{C} - \mathbf{X}|} \right) \cdot \mathbf{n} - \mathbf{C} \right) \quad (3.28)$$

$$\mathbf{s} \approx \mathbf{x}_2 - \mathbf{x}_1$$

where **X** are the object space coordinates of the target centre and **n** is the target normal as unit vector.

Whereas the eccentricity adds an offset towards the less distant target edge, the edge shift of retro-reflective targets points towards the more distant target edge, though the two offset vectors are only roughly parallel. Theoretically, there is an ideal target size where the two error offsets mostly cancel out since the eccentricity depends on the target size and the edge shift is diameter independent. Unfortunately, the target size for photogrammetric applications is defined by the size of the object being surveyed. However, both error effects can be corrected if the target plane is known.

4. Target Plane Determination within Digital Images

In this chapter the actual target plane determination process will be described. The general concept can be divided into two stages. First, the ellipse parameters of all imaged targets are determined. Then the ellipse information from multiple images of one circular target is used to compute its target plane. For the second stage the geometry of the photogrammetric network has to be known which means that a bundle adjustment is required within the target plane determination process.
Since the target plane determination is dealing with stochastic variables, least-squares adjustment is an appropriate method to determine the estimates. Though least-squares strategies are well-known for redundant engineering problems, basic knowledge about least-squares, which is necessary to understand derivations within the current chapter, will be discussed in the following.

4.1. Least-Squares Adjustment

In a statistical sense, adjustment is a method of deriving estimates for stochastic variables and their distribution parameters from observed samples. Of the different adjustment methods least squares is by far the most common. Its principles are based on derivations for an astronomical problem by C.F. Gauss. Its practical importance has recently been enhanced by the introduction of electronic computers, by the formulation of techniques in matrix notation, and by connecting its concept to statistics (Mikhail et al. 1996).

In the following, the special case of adjustment of indirect observations is described. First a model has to be found which connects stochastic variables. These can be differentiated into observations and parameters. The group of observations is given with a priori precision values, whereas the parameters should be determined in the adjustment process. In this special adjustment case, a mathematical description of each observation using only parameters is given. Since an adjustment system has to be redundant, there have to be more observations than parameters. To find a unique solution, however, only a subset of n_{obs} observations is needed to determine the n_{par} parameters. Consequently, multiple solutions can be computed. To overcome this problem least-squares methods add corrections, so called residuals, to each observation. This allows the observation equations to be written as

$$\mathbf{l} + \mathbf{v} = F(\mathbf{x}) \tag{4.1}$$

where $\mathbf{l}$ is the vector of observations, $\mathbf{v}$ the residual vector and $\mathbf{x}$ the sought-after vector of parameters. The equation system is solved using the constraint below (This is where the name least-squares comes from).

$$\Phi = \mathbf{v}^T \mathbf{W} \mathbf{v} \rightarrow \text{minimum} \tag{4.2}$$

The weight matrix $\mathbf{W}$ allows observations of different precision, as well as of different type to be treated correctly in a statistical sense. In simple adjustment problems the $\mathbf{W}$ matrix is often replaced by the identity matrix.

Whereas it is a straightforward matter to solve linear problems, non-linear systems have to be linearised and solved in iterations. Using matrix notation, linear and linearised problems can be described as

$$\mathbf{l} + \mathbf{v} = F(\mathbf{x_0}) + \frac{\partial F(\mathbf{x})}{\partial \mathbf{x}} \cdot \mathbf{\Delta} = \mathbf{l_0} + \mathbf{B} \cdot \mathbf{\Delta} \tag{4.3}$$

where $\mathbf{\Delta}$ represents $\mathbf{x}$ in linear systems and corrections to $\mathbf{x}$ in non-linear adjustments and $\mathbf{B}$ is the Jacobian matrix of the observation equations with respect to $\mathbf{x}$. In the non-linear case approximations of the parameters have to be known and the final estimates of the parameters are found iteratively by employing

$$\mathbf{x_{i+1}} = \mathbf{x_i} + \mathbf{\Delta} \tag{4.4}$$

after each iteration. Using equations (4.2) and (4.3), $\mathbf{\Delta}$ can be computed by

$$\begin{aligned} \mathbf{Q}_x &= \mathbf{N}^{-1} = \left(\mathbf{B}^T\mathbf{W}\mathbf{B}\right)^{-1} \\ \mathbf{\Delta} &= \mathbf{Q}_x \cdot \mathbf{B}^T\mathbf{W}\mathbf{l} \end{aligned} \tag{4.5}$$

In the presented adjustment model it is assumed that a minimum set of parameters are chosen which are all independent. However, in certain circumstances the mathematical description of the functional model is easier and more flexible if it is over-parameterised. In these cases the introduced degrees of freedom can be eliminated by added constraints to the adjustment model. The linearised constraints can be described by

$$\mathbf{C} \cdot \mathbf{\Delta} = \mathbf{g} \tag{4.6}$$

Consequently the main quadratic minimum condition (4.2) has to be extended

$$\Phi = \mathbf{v}^T\mathbf{W}\mathbf{v} - 2 \cdot \mathbf{k}^T\left(\mathbf{C} \cdot \mathbf{\Delta} - \mathbf{g}\right) \rightarrow \text{minimum} \tag{4.7}$$

where $\mathbf{k}$ is a vector of Lagrange multipliers. Considering the new minimum condition the equation system can be solved by

$$\begin{aligned} \overline{\mathbf{Q}} &= \begin{pmatrix} \mathbf{Q}_x & \mathbf{Q}_{cx}^T \\ \mathbf{Q}_{cx} & \mathbf{Q}_c \end{pmatrix} = \begin{pmatrix} \mathbf{B}^T\mathbf{W}\mathbf{B} & \mathbf{C}^T \\ \mathbf{C} & 0 \end{pmatrix}^{-1} \\ \begin{pmatrix} \mathbf{\Delta} \\ \mathbf{k} \end{pmatrix} &= \overline{\mathbf{Q}} \cdot \begin{pmatrix} \mathbf{B}^T\mathbf{W}\mathbf{l} \\ \mathbf{g} \end{pmatrix} \end{aligned} \tag{4.8}$$

Beside the determination of the parameters, least-squares provide accuracy estimations of the computed parameters and adjusted observations. The first quantity is σ_0^2, the variance of unit weight or also called the reference variance.

$$\begin{aligned} \sigma_0^2 &= \frac{\mathbf{v}^T\mathbf{W}\mathbf{v}}{r} \\ r &= n_{Observations} - n_{Parameters} + n_{Constraints} \end{aligned} \tag{4.9}$$

Above r is called the redundancy which depends on the number of observations, parameters and constraints. Using σ_0, the variance-covariance matrix of the estimated parameters can be described as

$$\boldsymbol{\Sigma}_x = \sigma_0^2 \mathbf{Q}_x \tag{4.10}$$

Often, not only the estimated standard error of the parameter is interesting, but also the standard error of variables, which can be described as a function of the parameters. Assuming variable(s) f

$$f = F(\mathbf{x}) \tag{4.11}$$

its linearisation can be described as

$$\partial \mathbf{f} = \mathbf{F} \cdot \boldsymbol{\Delta} \tag{4.12}$$

Using error propagation the variance-covariance matrix of the variables f is defined by

$$\boldsymbol{\Sigma}_f = \mathbf{F}\boldsymbol{\Sigma}_x\mathbf{F}^T = \sigma_0^2\mathbf{F}\mathbf{Q}_x\mathbf{F}^T \tag{4.13}$$

The observations can be described as formula (4.11) , hence its variance-covariance matrix follows as

$$\boldsymbol{\Sigma}_l = \mathbf{B}\boldsymbol{\Sigma}_x\mathbf{B}^T = \sigma_0^2\mathbf{B}\mathbf{Q}_x\mathbf{B}^T \tag{4.14}$$

Now, all necessary formulas are represented. The exact derivation of equations (4.1) to (4.14) can be found in the literature (e.g. Mikhail et al. 1996).

4.2. Ellipse-Fitting of Imaged Targets

As derived in Chapter 3.1, a plane circular target projects as a conic section into the image. However, in the case of VM it is justified to only consider ellipses as images (see Chapter 3). Because of lens distortion and other deformations (e.g. unflatness of the CCD chip) a target projects as an ellipse only by approximation, if the problem is analysed rigorously. This distortional effects may be neglected in the case of small target images since the central projection condition is very well fulfilled in small image patches.

The main issue in the ellipse-fitting process is to derive continuous ellipse parameters from a discreet image. In the following, two developed methods will be described which vary in computation speed and in the accuracy of the obtained ellipse parameters.

4.2.1. Best-Fit Ellipse of Intensity Levelled Points

Luhmann (2000) describes a solution where, from a rough ellipse centre, profile lines in various directions are computed. Then points on all profile lines at a certain intensity level are determined which are finally used to perform a best-fit ellipse adjustment. Using the new centre the process is repeated until convergence of the centre coordinates. In my research a slightly different approach

has been adopted, which can be solved without iterations and without computing profile lines of any orientation.

Any raster image can be interpreted as a 3D surface using the intensity value as the third coordinate, by connecting neighbouring pixel centres with lines. That way skewed quadrangles arise.

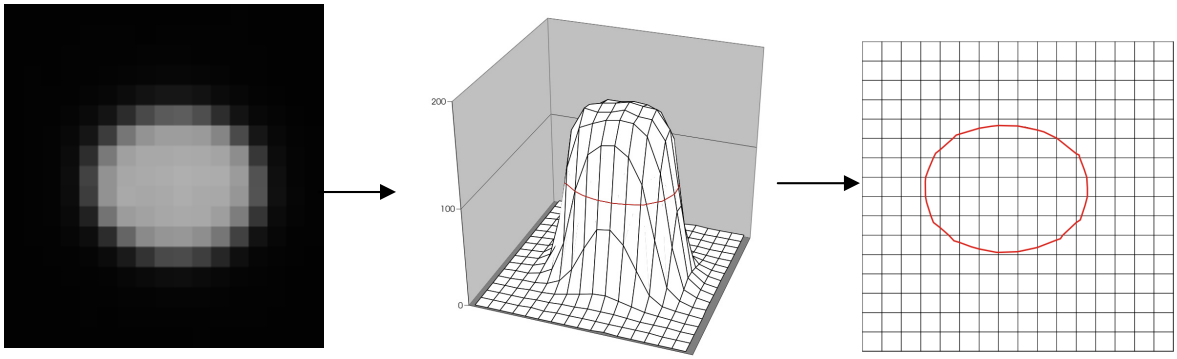

Figure 4.1: Real sample target displayed as 3D surface (so called intensity image) and intersected with a horizontal plane

The created surface intersected with an intensity levelled plane is used to determine the ellipse parameters. In a mathematical sense, points, which result from intersecting grid lines (right image of Figure 4.1) with a horizontal plane, are used for a best-fit ellipse adjustment. The intensity of the intersection plane should be approximately at the average of the targets maximum intensity and the background intensity. There, the gradient of the surface has a maximum. Consequently intensity errors of the pixels have minimal influence on the resulting intersection figure.

It is a straightforward matter to implement the grid line intersection and the best-fit ellipse adjustment (as it is described in Appendix A3) can be solved in one iteration. Thus the presented algorithm is highly efficient and very fast in computation. As it turns out the quality of the ellipse parameters is only satisfying for bigger targets (diameter >15 pixels). Two explanations can be found for the shortcomings of the algorithm when applied to small targets. First the process does not really meet the requirement to use as much pixel information as possible which is done for example by the intensity-weighted centroiding (see Chapter 2.2.1). Second, the edge of the target image is not as sharp as it theoretically should be. On the average, the edge of real targets is stretched up to four pixels (see Figure 4.1). This effect is based on shortcomings of the camera lens and the CCD chip.

To overcome these problems a second ellipse-fitting algorithm was developed. This will be described in the next section.

4.2.2. 2D Gaussian Distribution Fitting

The idea of using the 2D Gaussian distribution to find the centre of gravity of a 2D object appears widely in the literature. However, all derivations which were found, could not provide the required ellipse parameters because they only focussed on centre determination. Additionally, a visual analysis of the Gaussian distribution (Figure 4.3) and intensity images of real targets (Figure 4.2) indicates that the Gaussian distribution fits to small targets only. Bigger targets have an intensity plateau, which cannot be described by the Gaussian distribution.

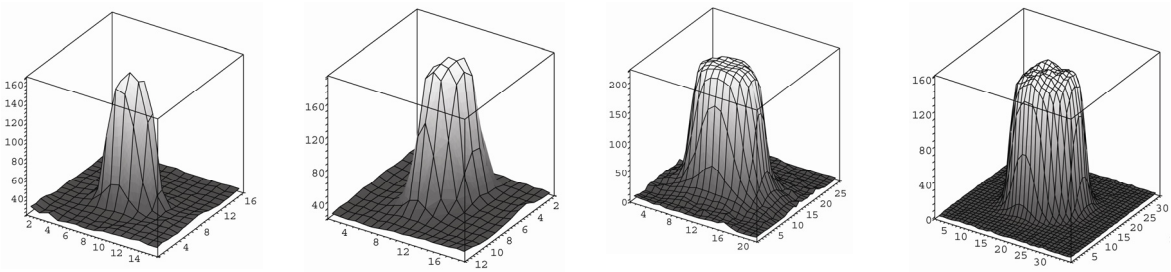

Figure 4.2: Various intensity images of real targets

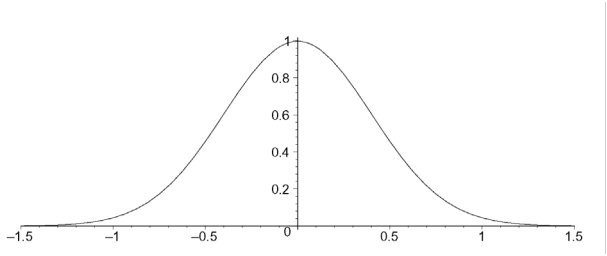

Figure 4.3: Well-known Gaussian (normal) distribution, also called bell curve

Thus, it was necessary to design a new continuously differentiable function, which can describe an ellipse shaped ‘mountain’ with a plateau.

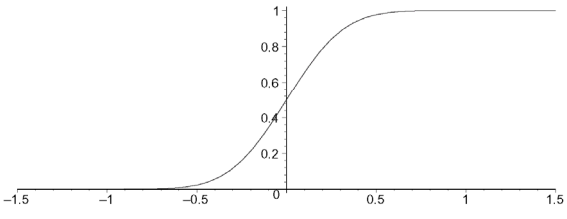

Figure 4.4: Cumulative Gaussian distribution (CGD)

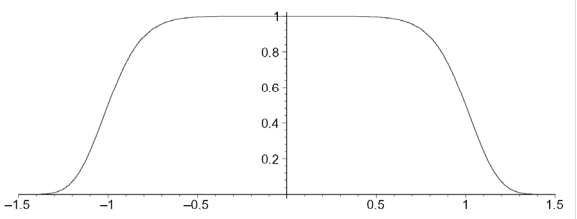

Figure 4.5: Target function derived from the CGD

It turned out that the cumulative Gaussian distribution (CGD) is an appropriate base function (Figure 4.4). It is defined by integrating the Gaussian distribution

$$\Omega(x) = c\int_{-\infty}^{x} \mathrm{G}(x)dx = \frac{1}{\sqrt{2\pi\sigma^2}}\int_{-\infty}^{x} e^{-\frac{(x-\mu)^2}{2\sigma^2}}dx = \frac{1}{2}\mathrm{erf}\left(\frac{(x-\mu)}{\sqrt{2}\sigma}\right)+\frac{1}{2} \tag{4.15}$$

where σ is the standard deviation and μ the expectation. Substituting x by $-(\bar{x}^2-1)$ in equation (4.15) leads to a 1D function which has the sought-after properties (Figure 4.5). The next step is to substitute x by an implicit ellipse equation, which finally results in the desired equation:

$$\begin{pmatrix}\bar{x}\\ \bar{y}\end{pmatrix} = \begin{pmatrix}\cos\phi & \sin\phi\\ -\sin\phi & \cos\phi\end{pmatrix}\begin{pmatrix}x-c_x\\ y-c_y\end{pmatrix} \tag{4.16}$$

$$\mathrm{E} = \frac{\bar{x}^2}{a^2}+\frac{\bar{y}^2}{b^2}-1 \tag{4.17}$$

$$\mathrm{T}(s,\beta,c_x,c_y,a,b,\phi,\sigma,\mu=0) = s\cdot\Omega(-\mathrm{E})+\beta \tag{4.18}$$

Whereas equation (4.16) describes a transformation, its usage in the implicit ellipse equation (4.17) allows interpretation of c_x and c_y as the centre of the ellipse and ϕ as the bearing of the semi major axis. Formula (4.18) describes, for the adjustment used, the best-fit equation where s defines a scale factor (Ω can only provide values between 0 and 1) and β the background noise. By modelling the background, a thresholding process, as needed for the intensity-weighted centroiding, can be cut out. In the following, different graphs of function T are listed to show the properties of its parameters and how well this function describes real targets. Special attention should be drawn onto the last parameter σ which defines the sharpness of the target signal.

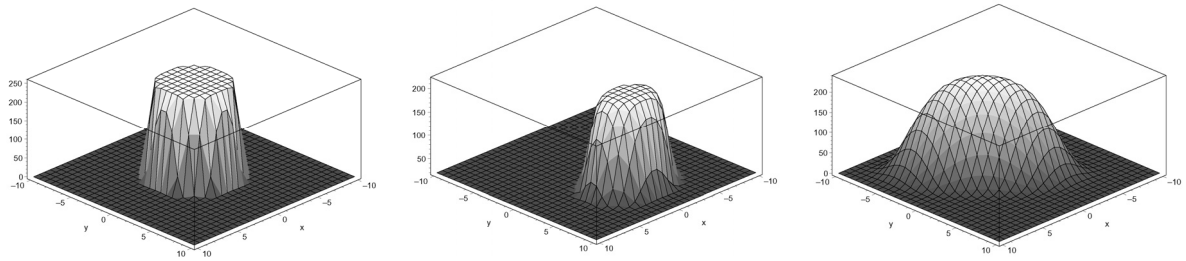

T(255, 0, 0 , 0, 4, 4, 0, 0.1) T(200, 20, 0 , 4, 4, 3, 0, 0.3) T(255, 0, 1 , -1, 6, 3, -π/4, 0.7)

Figure 4.6: Variation of the parameter values of equation $\mathrm{T}(s,\beta,c_x,c_y,a,b,\phi,\sigma)$ and their effects on the resulting graph.

To perform a best-fit adjustment the grey values of the pixels are taken as observations and the parameters of T as unknown. As can be seen, it is a non-linear problem and therefore the partial derivatives of T with respect to each parameter are required. Though there is a closed-form solution of the integral in equation (4.15) (by using the so called error function), its solution is not required for most of the partial derivations. Assuming that p_e is a parameter of the ellipse, the partial of T with respect to p_e can be described as

$$\frac{\partial \mathrm{T}}{\partial p_e} = \frac{\partial\left(s \cdot c \int \mathrm{G}(x)dx + \beta\right)}{\partial p_e} = s \cdot c \frac{\partial(\int \mathrm{G}(x)dx)}{\partial p_e} = s \cdot c \frac{\partial(\int \mathrm{G}(x)dx)}{\partial x}\frac{\partial x}{\partial p_e} = \\ = s \cdot c \cdot \mathrm{G}(x)\frac{\partial x}{\partial p_e} = -s \cdot c \cdot \mathrm{G}(-E)\frac{\partial E}{\partial p_e} \tag{4.19}$$

Because the partial of the implicit ellipse equation with respect to p_e is straightforward, only the final derivation is presented here:

$$\frac{\partial \mathrm{T}}{\partial c_x} = h\left(\frac{\bar{x}\cos\phi}{a^2} - \frac{\bar{y}\sin\phi}{b^2}\right) \\ \frac{\partial \mathrm{T}}{\partial c_y} = h\left(\frac{\bar{x}\sin\phi}{a^2} + \frac{\bar{y}\cos\phi}{b^2}\right) \tag{4.20}$$

$$\frac{\partial \mathrm{T}}{\partial a} = h\left(\frac{\overline{x^2}}{a^3}\right) \\ \frac{\partial \mathrm{T}}{\partial b} = h\left(\frac{\overline{y^2}}{b^3}\right) \tag{4.21}$$

$$\frac{\partial \mathrm{T}}{\partial \phi} = h \cdot \overline{\overline{xy}}\left(\frac{1}{b^2} - \frac{1}{a^2}\right) \tag{4.22}$$

where h can be described as

$$h = 2s \cdot c \cdot \sigma \cdot \mathrm{G}(-\mathrm{E}) \tag{4.23}$$

The partial derivatives with respect to σ, s and β are

$$\frac{\partial \mathrm{T}}{\partial \sigma} = -E \cdot s \cdot \mathrm{G}(-\mathrm{E}) \\ \frac{\partial \mathrm{T}}{\partial s} = \Omega(-\mathrm{E}) \\ \frac{\partial \mathrm{T}}{\partial \beta} = 1 \tag{4.24}$$

Thus, all necessary derivations to perform a best-fit adjustment are made. As will be shown in Chapter 7.2, this method of determining the ellipse parameters delivers satisfying results even for small targets. In the case of very small targets (diameter <5 pixels), however, there is a high correlation between σ and a. This is why the adjustment mostly diverges. This shortcoming can be passed over by 'observing' σ in the adjustment.

4.3. Target Plane Adjustment

In this section the actual target plane determination stage is described using the ellipse information gained from ellipse-fitting adjustments. As mentioned, the problem can be solved if the geometry of the network configuration is known.

Whereas the plane determination method described by Kager (1981) uses information of only one ellipse, the new method needed to use the ellipse information of all photos where the target was imaged. This is necessary since the target images are small in diameter, which results in low accuracy of the extracted ellipse parameters. For the thesis, two rigorous methods were developed, which met the stated requirements. The method, which will be reported next, was developed first. Compared to the second method, the required formulas are relatively simple. However, it has also two disadvantages regarding matrix sizes and error propagation as described below.

4.3.1. Target Plane Adjustment by Point Projection

The general idea of this method is that ellipse points project onto the circle of the target as indicated in Figure 4.7. Using this constraint an adjustment can be performed to solve for the parameters of the circle.

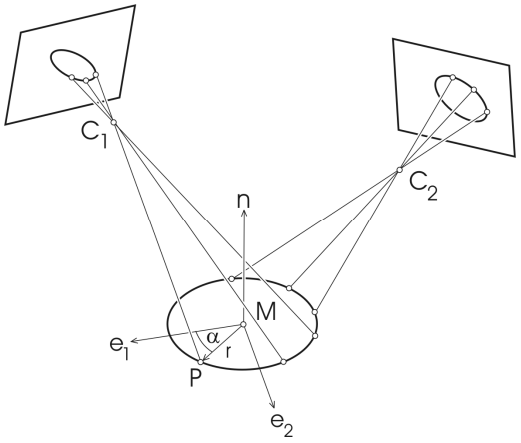

Figure 4.7: Ellipse points projected onto the target circle

The problem can be solved by employing an adjustment of indirect observations, where the image coordinates of the ellipse points are the observations. The function which describes the observations depends upon the parameters. This will be derived below.

A point on a circle in 3D space can be described by

$$\mathbf{P} = \mathbf{M} + r \cdot \cos\alpha \cdot \mathbf{e_1} + r \cdot \sin\alpha \cdot \mathbf{e_2} \tag{4.25}$$

where $\mathbf{M}$ is the midpoint of the circle, r the radius and $\mathbf{e_1}$ and $\mathbf{e_2}$ are arbitrary vectors, which represent a ortho-normalised basis (including the vector $\mathbf{n}$). Using the collinearity condition (3.2) equation (4.25) can be transformed into image space.

$$x = -c\frac{\mathbf{R}_1(\mathbf{P}-\mathbf{C})}{\mathbf{R}_3(\mathbf{P}-\mathbf{C})} = -c\frac{\mathbf{R}_1(\mathbf{M}-\mathbf{C}+r\cdot\cos\alpha\cdot\mathbf{e_1}+r\cdot\sin\alpha\cdot\mathbf{e_2})}{\mathbf{R}_3(\mathbf{M}-\mathbf{C}+r\cdot\cos\alpha\cdot\mathbf{e_1}+r\cdot\sin\alpha\cdot\mathbf{e_2})} = -c\frac{\mathbf{R}_1\mathbf{v}}{\mathbf{R}_3\mathbf{v}}$$
$$y = -c\frac{\mathbf{R}_2(\mathbf{P}-\mathbf{C})}{\mathbf{R}_3(\mathbf{P}-\mathbf{C})} = -c\frac{\mathbf{R}_2(\mathbf{M}-\mathbf{C}+r\cdot\cos\alpha\cdot\mathbf{e_1}+r\cdot\sin\alpha\cdot\mathbf{e_2})}{\mathbf{R}_3(\mathbf{M}-\mathbf{C}+r\cdot\cos\alpha\cdot\mathbf{e_1}+r\cdot\sin\alpha\cdot\mathbf{e_2})} = -c\frac{\mathbf{R}_1\mathbf{v}}{\mathbf{R}_3\mathbf{v}} \qquad (4.26)$$

Because the system is non-linear, the partial derivatives with respect to the circle parameters (**M**, r, $\mathbf{e_1}$ and $\mathbf{e_2}$) and angle parameter α have to be calculated. It should be mentioned that each point has its own angle parameter.

$$\overline{\mathbf{v}} = \mathbf{R}\cdot\mathbf{v}$$
$$\overline{\mathbf{e_1}} = \mathbf{R}\cdot(\cos\alpha\cdot\mathbf{e_1}+\sin\alpha\cdot\mathbf{e_2}) \qquad (4.27)$$
$$\overline{\mathbf{e_2}} = \mathbf{R}\cdot(\cos\alpha\cdot\mathbf{e_2}-\sin\alpha\cdot\mathbf{e_1})$$

$$\frac{\partial x}{\partial C_x} = \frac{c}{\overline{v_3}^2}\left(R_{31}\cdot\overline{v_1}-R_{11}\cdot\overline{v_3}\right) \qquad \frac{\partial y}{\partial C_x} = \frac{c}{\overline{v_3}^2}\left(R_{31}\cdot\overline{v_2}-R_{21}\cdot\overline{v_3}\right)$$
$$\frac{\partial x}{\partial C_y} = \frac{c}{\overline{v_3}^2}\left(R_{32}\cdot\overline{v_1}-R_{12}\cdot\overline{v_3}\right) \qquad \frac{\partial y}{\partial C_y} = \frac{c}{\overline{v_3}^2}\left(R_{32}\cdot\overline{v_2}-R_{22}\cdot\overline{v_3}\right)$$
$$\frac{\partial x}{\partial C_z} = \frac{c}{\overline{v_3}^2}\left(R_{33}\cdot\overline{v_1}-R_{13}\cdot\overline{v_3}\right) \qquad \frac{\partial y}{\partial C_z} = \frac{c}{\overline{v_3}^2}\left(R_{33}\cdot\overline{v_2}-R_{23}\cdot\overline{v_3}\right)$$

$$\frac{\partial x}{\partial e_{1x}} = \frac{c\cdot r\cdot\cos\alpha}{\overline{v_3}^2}\left(R_{31}\cdot\overline{v_1}-R_{11}\cdot\overline{v_3}\right) \qquad \frac{\partial y}{\partial e_{1x}} = \frac{c\cdot r\cdot\cos\alpha}{\overline{v_3}^2}\left(R_{31}\cdot\overline{v_2}-R_{21}\cdot\overline{v_3}\right)$$
$$\frac{\partial x}{\partial e_{1y}} = \frac{c\cdot r\cdot\cos\alpha}{\overline{v_3}^2}\left(R_{32}\cdot\overline{v_1}-R_{12}\cdot\overline{v_3}\right) \qquad \frac{\partial y}{\partial e_{1y}} = \frac{c\cdot r\cdot\cos\alpha}{\overline{v_3}^2}\left(R_{32}\cdot\overline{v_2}-R_{22}\cdot\overline{v_3}\right)$$
$$\frac{\partial x}{\partial e_{1z}} = \frac{c\cdot r\cdot\cos\alpha}{\overline{v_3}^2}\left(R_{33}\cdot\overline{v_1}-R_{13}\cdot\overline{v_3}\right) \qquad \frac{\partial y}{\partial e_{1z}} = \frac{c\cdot r\cdot\cos\alpha}{\overline{v_3}^2}\left(R_{33}\cdot\overline{v_2}-R_{23}\cdot\overline{v_3}\right)$$

$$\frac{\partial x}{\partial e_{2x}} = \frac{c\cdot r\cdot\sin\alpha}{\overline{v_3}^2}\left(R_{31}\cdot\overline{v_1}-R_{11}\cdot\overline{v_3}\right) \qquad \frac{\partial y}{\partial e_{2x}} = \frac{c\cdot r\cdot\sin\alpha}{\overline{v_3}^2}\left(R_{31}\cdot\overline{v_2}-R_{21}\cdot\overline{v_3}\right)$$
$$\frac{\partial x}{\partial e_{2y}} = \frac{c\cdot r\cdot\sin\alpha}{\overline{v_3}^2}\left(R_{32}\cdot\overline{v_1}-R_{12}\cdot\overline{v_3}\right) \qquad \frac{\partial y}{\partial e_{2y}} = \frac{c\cdot r\cdot\sin\alpha}{\overline{v_3}^2}\left(R_{32}\cdot\overline{v_2}-R_{22}\cdot\overline{v_3}\right)$$
$$\frac{\partial x}{\partial e_{2z}} = \frac{c\cdot r\cdot\sin\alpha}{\overline{v_3}^2}\left(R_{33}\cdot\overline{v_1}-R_{13}\cdot\overline{v_3}\right) \qquad \frac{\partial y}{\partial e_{2z}} = \frac{c\cdot r\cdot\sin\alpha}{\overline{v_3}^2}\left(R_{33}\cdot\overline{v_2}-R_{23}\cdot\overline{v_3}\right)$$

$$\frac{\partial x}{\partial r} = \frac{c}{\overline{v_3}^2}\left(\overline{e_{1z}}\cdot\overline{v_1}-\overline{e_{1x}}\cdot\overline{v_3}\right) \qquad (4.28) \qquad \frac{\partial y}{\partial r} = \frac{c}{\overline{v_3}^2}\left(\overline{e_{2z}}\cdot\overline{v_2}-\overline{e_{2x}}\cdot\overline{v_3}\right) \qquad (4.29)$$

$$\frac{\partial x}{\partial \alpha} = \frac{c\cdot r}{\overline{v_3}^2}\left(\overline{e_{2z}}\cdot\overline{v_1}-\overline{e_{2x}}\cdot\overline{v_3}\right) \qquad \frac{\partial y}{\partial \alpha} = \frac{c\cdot r}{\overline{v_3}^2}\left(\overline{e_{1z}}\cdot\overline{v_2}-\overline{e_{1x}}\cdot\overline{v_3}\right)$$

Using six parameters within the vectors $\mathbf{e_1}$ and $\mathbf{e_2}$ to described the circle plane, the system is over-parameterised since two angles are sufficient to described any target plane orientation. To eliminate

the four degrees of freedom within the parameterisation, constraints have to be introduced into the adjustment. The following three constrains secure the ortho-normalised basis

$$\begin{aligned} c_1 &= \left\|\mathbf{e_1}\right\| - 1 = 0 \\ c_2 &= \left\|\mathbf{e_2}\right\| - 1 = 0 \\ c_3 &= \mathbf{e_1} \cdot \mathbf{e_2} = 0 \end{aligned} \quad \Rightarrow \quad \begin{aligned} &\frac{1}{2}\partial c_1 = e_{1x} \cdot \partial e_{1x} + e_{1y} \cdot \partial e_{1y} + e_{1z} \cdot \partial e_{1z} = 0 \\ &\frac{1}{2}\partial c_2 = e_{2x} \cdot \partial e_{2x} + e_{2y} \cdot \partial e_{2y} + e_{2z} \cdot \partial e_{2z} = 0 \\ &\partial c_3 = e_{2x} \cdot \partial e_{1x} + e_{2y} \cdot \partial e_{1y} + e_{2z} \cdot \partial e_{1z} + e_{1x} \cdot \partial e_{2x} + e_{1y} \cdot \partial e_{2y} + e_{1z} \cdot \partial e_{2z} = 0 \end{aligned} \tag{4.30}$$

The final constraint has to prevent $\mathbf{e_1}$ and $\mathbf{e_2}$ from rotation within the target plane, which can be defined in multiple ways. E.g. $\mathbf{e_1}$ has to be normal to the y axis. However, the implemented adjustment uses the following differential constraint:

$$\partial c_4 = e_{2x} \cdot \partial e_{1x} + e_{2y} \cdot \partial e_{1y} + e_{2z} \cdot \partial e_{1z} = 0 \tag{4.31}$$

As mentioned, each point has its own angle parameter (4.25). Hence the size of the equation system depends on the number of 'observed' points. It turns out that five points per ellipse (=10 observations) are needed to achieve appropriate results. If there are less than four ellipses available, 10 points per ellipse (=20 observations) should be used. This is an unsatisfactory fact since an ellipse can only provide five independent observations. Additionally, it is not possible to directly introduce the covariance information from previous ellipse-fitting adjustments. To overcome these two shortcomings a second, mathematically more complex target plane adjustment was developed, as described in the next section.

4.3.2. Target Plane Adjustment by Observing Implicit Ellipse Parameters

This adjustment model is based on the derivations made in Chapter 3.1. There a description of the implicit ellipse parameters depending on the target elements (see equation 3.23) was found which can be used for an adjustment of indirect observations. Since the formula uses the normal vector **n** rather than the ortho-normalised basis $\mathbf{e_1}$ and $\mathbf{e_2}$, the adjustment has to solve for 7 unknowns only (target centre **M**, radius r and vector **n**).

Again, it is a non-linear system and partial derivations are required. Since the final formulas are lengthy, the derivation is presented in stages and auxiliary variables are introduced. The five observation equations can be written in the following form

$$a_j = \frac{b_j}{d} \tag{4.32}$$

Using the quotient rule, the partials regarding the target centre, the target normal and the radius follow as

$$\frac{\partial a_j}{\partial M_k} = \frac{\frac{\partial b_j}{\partial M_k} d - b_j \frac{\partial d}{\partial M_k}}{d^2} \tag{4.33}$$

$$\frac{\partial a_j}{\partial n_k} = \frac{\frac{\partial b_j}{\partial n_k} d - b_j \frac{\partial d}{\partial n_k}}{d^2} \tag{4.34}$$

$$\frac{\partial a_j}{\partial r} = \frac{\frac{\partial b_j}{\partial r} d - b_j \frac{\partial d}{\partial r}}{d^2} \tag{4.35}$$

The required partial derivations of the coefficients b_j and d are straightforward and listed below. First the partial derivatives regarding the circle centre coordinates M_k are determined:

$$\frac{\partial b_1}{\partial M_k} = -2\left(\left(\overline{v_2} i_2 + \overline{v_3} i_3\right)\left(R_{2k} i_2 + R_{3k} i_3\right) + i_1^2 \left(R_{2k} \overline{v_2} + R_{3k} \overline{v_3}\right)\right)$$

$$\frac{\partial b_2}{\partial M_k} = 2\left(\left(1 - i_3^2\right)\left(R_{2k} \overline{v_1} + R_{1k} \overline{v_2}\right) + R_{3k} i_3 \left(i_2 \overline{v_1} + i_1 \overline{v_2}\right) + \overline{v_3}\left(R_{1k} i_2 i_3 + R_{2k} i_1 i_3 - 2R_{3k} i_1 i_2\right)\right)$$

$$\frac{\partial b_3}{\partial M_k} = 2\left(\left(\overline{v_1} i_3 - \overline{v_3} i_1\right)\left(R_{1k} i_3 - R_{1k} i_1\right) - R_{1k} \overline{v_1} - R_{3k} \overline{v_3}\right) \tag{4.36}$$

$$\frac{\partial b_4}{\partial M_k} = 2c\left(\left(i_1^2 - 1\right)\left(R_{1k} \overline{v_3} + R_{3k} \overline{v_1}\right) - R_{2k}\left(i_2\left(\overline{v_3} i_1 + \overline{v_1} i_3\right) - 2 i_1 i_3 \overline{v_2}\right) - \overline{v_2} i_2 \left(R_{3k} i_1 + R_{1k} i_3\right)\right)$$

$$\frac{\partial b_5}{\partial M_k} = 2c\left(\left(i_1^2 - 1\right)\left(R_{3k} \overline{v_2} + R_{2k} \overline{v_3}\right) - R_{1k} i_1 \left(i_3 \overline{v_2} + i_2 \overline{v_3}\right) + \overline{v_1}\left(2R_{1k} i_2 i_3 - R_{3k} i_1 i_2 - R_{2k} i_1 i_3\right)\right)$$

$$\frac{\partial d}{\partial M_k} = 2c^2\left(\left(\overline{v_2} i_1 - \overline{v_1} i_2\right)\left(R_{1k} i_2 - R_{2k} i_1\right) + R_{1k} \overline{v_1} + R_{2k} \overline{v_2}\right)$$

Next, the partial derivations required for the target normal parameters n_k are derived:

$$\frac{\partial b_1}{\partial n_k} = 2\left(R_{1k} i_1 \left(r^2 - \overline{v_2}^2 - \overline{v_3}^2\right) - \left(\overline{v_2} i_2 + \overline{v_3} i_3\right)\left(R_{2k} \overline{v_2} + R_{3k} \overline{v_3}\right)\right)$$

$$\frac{\partial b_2}{\partial n_k} = 2\left(\left(r^2 - \overline{v_3}^2\right)\left(R_{1k} i_2 + R_{2k} i_1\right) + \overline{v_3} i_3 \left(R_{1k} \overline{v_2} + R_{2k} \overline{v_1}\right) + R_{3k}\left(\overline{v_1}\,\overline{v_3} i_2 + \overline{v_2}\,\overline{v_3} i_1 - 2\overline{v_1}\,\overline{v_2} i_3\right)\right)$$

$$\frac{\partial b_3}{\partial n_k} = 2\left(R_{2k} r^2 i_2 + \left(\overline{v_1} i_3 - \overline{v_3} i_1\right)\left(R_{3k} \overline{v_1} - R_{1k} \overline{v_3}\right)\right)$$

$$\frac{\partial b_4}{\partial n_k} = 2c\left(\overline{v_2}\left(R_{1k}\left(\overline{v_2} i_3 - \overline{v_3} i_2\right) - R_{2k}\left(\overline{v_1} i_3 + \overline{v_3} i_1\right) + R_{3k}\left(\overline{v_2} i_1 - \overline{v_1} i_2\right)\right) + 2R_{2k}\,\overline{v_1}\,\overline{v_3} i_2\right) \tag{4.37}$$

$$\frac{\partial b_5}{\partial n_k} = 2c\left(\left(\overline{v_1}^2 - r^2\right)\left(R_{3k} i_2 + R_{2k} i_3\right) - \overline{v_1} i_1 \left(R_{3k} \overline{v_2} + R_{2k} \overline{v_3}\right) + R_{1k}\left(2\overline{v_2}\,\overline{v_3} i_1 - \overline{v_1}\,\overline{v_3} i_2 - \overline{v_1}\,\overline{v_2} i_3\right)\right)$$

$$\frac{\partial d}{\partial n_k} = -2c^2\left(\left(\overline{v_2} i_1 - \overline{v_1} i_2\right)\left(R_{1k} \overline{v_2} - R_{2k} \overline{v_1}\right) + R_{3k} r^2 i_3\right)$$

Finally the simple partial derivatives regarding the radius r are given as

$$\frac{\partial b_1}{\partial r} = 2ri_1^2 \qquad \frac{\partial b_4}{\partial r} = -2cri_1i_3$$
$$\frac{\partial b_2}{\partial r} = 2ri_1i_2 \qquad \frac{\partial b_5}{\partial r} = -2cri_2i_3 \tag{4.38}$$
$$\frac{\partial b_3}{\partial r} = 2ri_2^2 \qquad \frac{\partial d}{\partial r} = -2c^2ri_3^2$$

For this adjustment model only one constrain is needed which secures that the target normal is a unit vector.

$$c_1 = \|\mathbf{n}\| - 1 = 0 \quad \Rightarrow \quad \frac{1}{2}\partial c_1 = n_x \cdot \partial n_x + n_y \cdot \partial n_y + n_z \cdot \partial n_z = 0 \tag{4.39}$$

Compared to the first target plane adjustment (see Chapter 4.3.1), this model offers several advantages. The full information for the ellipse is introduced by only five observations, comparing to ≥10 observations in the previous model. Secondly, the normal equation matrix always has the same size, namely 8 by 8 (7 unknowns + 1 constraint), whereas the normal equation matrix size in the first model usually exceeded 40. Hence, the second model clearly offers a better computation performance.

However, this model provides a statistical advantage also. It allows the introduction of the full variance-covariance information from the ellipse-fit adjustment. It only has to be considered that the ellipse-fit adjustment uses different ellipse parameters than this adjustment model. The necessary conversion of the variance matrix is described in Appendix A2.

Since the described adjustment model is a non-linear equation system, approximations of the unknowns are required (see Chapter 4.1). Whereas approximations of the target centre are directly given from the previously performed bundle adjustment, appropriate starting values for the target normal are much more difficult to obtain. A neat solution can be found if the derived equations from Kager (1981) are employed. As described in his work, it is possible to determine the target normal using only one ellipse, based on the eigenvalue decomposition of symmetric matrices. However, an ambiguity of two solutions exists as already indicated in Figure 3.2. To resolve this ambiguity multiple algorithms appear possible. Though, it has to be considered that the correct solution of the target normal approximation can be distorted by up to 10 degrees in the case of small targets.

The current method uses only one set of target normals which is computed from the ellipse with the biggest diameter and the highest diameter ratio (semi-major divided by semi-minor). This secures a clear separation of the two target normal approximations. To select the correct solution, the average radius and its standard deviation are computed by projecting ellipse points from all images onto the target plane. The solution with the smaller standard deviation of the radius is chosen as the correct

one. This turned out to be a very fast and robust method for practical applications. Additionally, the algorithm delivers an accurate value for the radius along the way.

The achievable accuracy of the target normal determination within practical application is presented in Chapter 7.2. Next, the distortional effect of the eccentricity on the bundle adjustment will be described.

5. Eccentricity Effect on Bundle Adjustment

Earlier investigations (Dold, 1996; Ahn et al., 1997) have studied the impact of the eccentricity error on a bundle adjustment. It was reported that in a free network adjustment with or without simultaneous camera calibration, the eccentricity error caused by moderately sized image targets is almost fully compensated by changes in the exterior orientation parameters (and the principal distance) without affecting the other estimated parameters (Ahn et al., 1999).

Network simulations performed by the author have shown good agreement with earlier findings, especially when employing test fields with little variation in the target normals. However, test fields with a significant range of target orientations and with medium to big-sized targets can show significant distortions within the triangulated object point coordinates. However, the relevance of the eccentricity effect is clearly dependent on the centroiding accuracy. If the size of the eccentricity falls below the centroiding precision, the resulting distortion will be considered as noise. This consideration demands in simulations that real images are computed rather than just ellipse centers. One way to create the required imagery is described in the following section.

5.1. Creating Simulated Images

It is assumed that the geometry of the network is given. Additionally the orientation of the virtual circular target and its size have to be selected. The first step of the creation process is to back project each circle into the images. The resulting conic sections can be directly computed by equations (3.23) and (3.24) or indirectly determined by back projecting five arbitrary points of the circle into the image. Using these five points the coefficients of a general polynomial of second degree are determined (see Appendix A3). The second approach has the advantage that a virtual lens distortion can be taken into account very easily.

In the next step the continuous ellipse equation has to be rasterised as a digital image. Therefore some knowledge about the electronic processes during the exposure is necessary. In digital cameras, CCD chips accumulate the mount of light which hits each pixel cell and they output corresponding intensity values. To simplify the matter, only greyscale images are considered here and their intensity values translate directly to grey values. To create an 8-bit image with maximum contrast, background pixels are set to black (grey value 0) and target pixels which are completely covered by the target ellipse are set to white (grey value 255). Linking the aforementioned facts it can be derived that the grey value of a pixel (gv) depends on the area of the pixel which is covered by the ellipse (A_{ell}) and a factor which represents the maximum grey value for a target pixel. Hence,

$$gv = I_{\max} \cdot A_{ell} + I_{Background} = 255 \cdot A_{ell} \tag{5.1}$$

where A_{ell} has the dimension pixel^2. Using this formula, images such as Figure 5.1 can be computed.

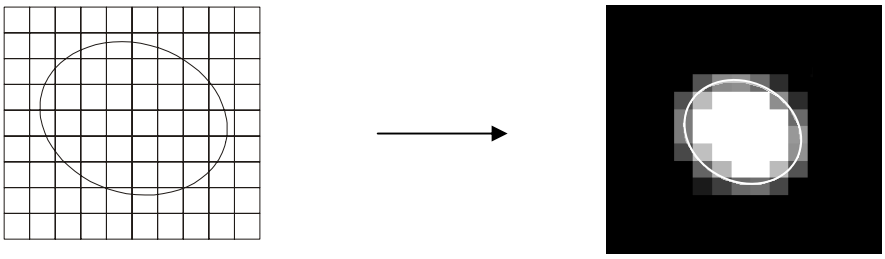

Figure 5.1: Simulated sample target including back projected target boundary

Though equation (5.1) is simple, the rigorous computation of the pixel area which is covered by the ellipse turns out to be difficult. There are many different cases of intersection of the ellipse with a pixel boundary.

The developed rasterising algorithm can be subdivided into two stages. First, the corners of each pixel are checked to see if they are inside the ellipse. Assuming that the ellipse is given in implicit form

$$E(x,y) = a_1 \cdot x^2 + a_2 \cdot xy + a_3 \cdot y^2 + a_4 \cdot x + a_5 \cdot y - 1 = 0 \tag{5.2}$$

x can be described as

$$x_{RightEdge/LeftEdge} = \frac{-a_4 - a_2 y \pm \sqrt{\left(a_4 + a_2 y\right)^2 - 4a_1\left(a_3 y^2 + a_5 y - 1\right)}}{2a_1} \tag{5.3}$$

and y can be described as

$$y_{UpperEdge/LowerEdge} = \frac{-a_5 - a_2 x \pm \sqrt{\left(a_5 + a_2 x\right)^2 - 4a_3\left(a_1 x^2 + a_4 x - 1\right)}}{2a_3} \tag{5.4}$$

To check if a certain point is inside the ellipse, its y coordinate is used to compute $x_{RightEdge/LeftEdge}$ of equation (5.3). If the points x coordinate is between $x_{LeftEdge}$ and $x_{RightEdge}$, then the point is inside the ellipse. The point-in-ellipse test can be equally performed employing equation (5.4). For completeness it should be mentioned that there is another neat solution to solve this problem by directly employing equation (5.2) and the given coordinates.

$$E(x,y)\begin{cases} > 0 \ldots\ldots \text{outside ellipse} \\ = 0 \ldots. \text{touching ellipse} \\ < 0 \ldots\ldots\ldots \text{inside ellipse} \end{cases} \tag{5.5}$$

The result of the corner check process is a matrix where each cell knows which of its corners is inside the ellipse. Therefore the corners are represented by bit values as indicated in Figure 5.2.

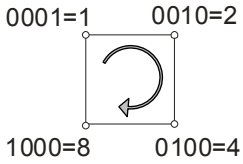

Figure 5.2: Corners of pixel are represented by bit values

Using the computed corner matrix (see Figure 5.3) the pixel area which is covered by the ellipse is now known for a great part of the pixels. Pixels with all corners inside the ellipse have to be completely inside the ellipse since the ellipse is a convex curve. For pixels with one and up to three 'ellipse' corners, the ellipse covered area has to be computed in the second stage. All other pixels are outside and hence have a grey value of 0. The last statement ignores rare cases where no corner is inside the ellipse although the ellipse intersects the pixel borders. However, these situations can be easily detected in the second stage and therefore treated correctly.

0	0	0	0	0	0	0	0	0	0
0	0	4	12	12	12	12	8	0	0
0	4	14	15	15	15	15	13	8	0
0	6	15	15	15	15	15	15	9	0
0	6	15	15	15	15	15	15	9	0
0	2	7	15	15	15	15	15	9	0
0	0	2	7	15	15	15	11	1	0
0	0	0	2	3	3	3	1	0	0
0	0	0	0	0	0	0	0	0	0

Figure 5.3: Example of corner matrix

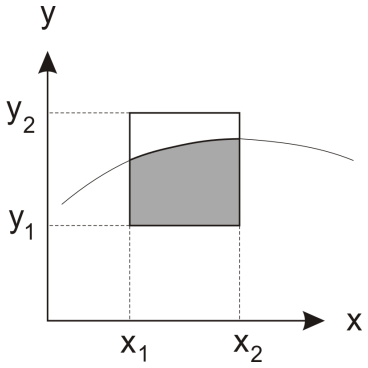

Figure 5.4: Integration allows a rigorous area determination

To compute the ellipse covered area rigorously, the ellipse equation has to be integrated (see Figure 5.4) which is possible with restriction only. As equations (5.3) and (5.4) show, there is no unique closed-from description of x depending on y, and y depending on x. Consequently, a distinction of cases must be made for the area calculation. For pixels in the lower area, the area follows as

$$A_{LowerEdge} = \int_{x_1}^{x_2} \left(y_1 - y_{LowerEdge} \right) dx = \int_{x_1}^{x_2} y_1 dx - \int_{x_1}^{x_2} y_{LowerEdge} dx = \left(x_2 - x_1 \right) y_1 - Y_{LowerEdge} \Big|_{x_1}^{x_2} \quad (5.6)$$

and in the upper part as

$$A_{UpperEdge} = \int_{x_1}^{x_2} \left(y_{UpperEdge} - y_2 \right) dx = \int_{x_1}^{x_2} y_{UpperEdge} dx - \int_{x_1}^{x_2} y_2 dx = Y_{UpperEdge} \Big|_{x_1}^{x_2} - \left(x_2 - x_1 \right) y_2 \quad (5.7)$$

In special situations (e.g. see right illustration in Figure 5.5) the area between the upper edge and the lower edge is needed, which can be computed by

$$A_{Between} = \int_{x_1}^{x_2} \left(y_{UpperEdge} - y_{LowerEdge} \right) dx = Y_{UpperEdge} \Big|_{x_1}^{x_2} - Y_{LowerEdge} \Big|_{x_1}^{x_2} \quad (5.8)$$

The required function $Y_{UpperEdge/LowerEdge}$ within equations (5.6) to (5.8) is defined by

$$Y_{UpperEdge/LowerEdge} = \frac{\pm 4a_3 \arctan\frac{n_2}{n_1} c_2 \mp n_1 n_2 - x\left(a_2 x + 2a_5\right) c_1^{\,3}}{4a_3 c_1^{\,3}} \tag{5.9}$$

using the following auxiliary variables

$$\begin{aligned} c_1 &= \sqrt{-a_2^{\,2} + 4a_1 a_3} \\ c_2 &= -4a_1 a_3 - a_1 a_5^{\,2} - a_3 a_4^{\,2} + a_2 a_4 a_5 + a_2^{\,2} \end{aligned} \tag{5.10}$$

$$\begin{aligned} n_1 &= c_1 \sqrt{\left(a_5 + a_2 x\right)^2 - 4a_3\left(a_1 x^2 + a_4 x - 1\right)} \\ n_2 &= -c_1^{\,2} x + a_2 a_5 - 2a_3 a_4 \end{aligned} \tag{5.11}$$

Whereas equation (5.6) and (5.7) integrate y with respect to x, it is likewise to integrate x with respect to y. Therefore $X_{RightEdge/LeftEdge}$ is needed which is, for completeness, listed below:

$$X_{RightEdge/LeftEdge} = \frac{\pm 4a_1 \arctan\frac{m_2}{m_1} c_2 \mp m_1 m_2 - y\left(a_2 y + 2a_4\right) c_1^{\,3}}{4a_1 c_1^{\,3}} \tag{5.12}$$

where m_1 and m_2 are defined as

$$\begin{aligned} m_1 &= c_1 \sqrt{\left(a_4 + a_2 y\right)^2 - 4a_1\left(a_3 y^2 + a_5 y - 1\right)} \\ m_2 &= -c_1^{\,2} y + a_2 a_4 - 2a_1 a_5 \end{aligned} \tag{5.13}$$

equations (5.6) to (5.13) embodys all formulae required for the area computation process. However, the major difficulty is the great variety of configurations which may appear. A few examples are illustrated in Figure 5.5. As indicated by the different coloured regions, the ellipse covered area has to be computed within stages.

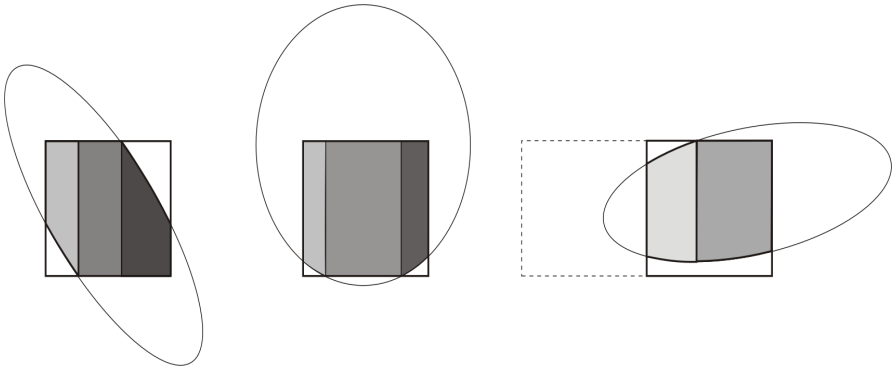

Figure 5.5: Various intersection configurations

An example of the configuration where no pixel corners are inside, although the ellipse partly covers the pixel area, can be seen at the dashed pixel on the right in Figure 5.5. If the algorithm

detects a double intersection of ellipse with one of the current boundary lines, the corresponding neighbour pixel is marked for the area computation as well.

As outlined, the rigorous area computation algorithm is sophisticated enough to tread all possible intersection configurations correctly. However, there is a simple test to check the correctness of the computations. The sum of all partial areas has to be equal to the ellipse area.

$$\sum_i A_i = \pi ab \tag{5.14}$$

where a is the semi-major and b is the semi-minor of the ellipse.

5.2. Eccentricity Effect on a Plane Test Field

In the following chapters it will be investigated how the eccentricity distorts certain network configurations that typically appear in surface inspections. As mentioned above, the centroided observations were used for the computations which allows more realistic quantifications of the effect for practical applications.

The calculations of all test fields were performed in the same manner. Specific object point and camera station arrangement was selected. Then the corresponding images were simulated and the controided observations determined. Using these observations a bundle adjustment employing self-calibration was performed. The final computed object point coordinates were then transformed onto the original error-free object points. The resulting discrepancy vectors allow an assessment of the eccentricity effect onto the current test field. Since the target size is the critical factor for the eccentricity, each test configuration was computed multiple times to estimate the influence of different target sizes.

It should be mentioned that a scale distance was also used within the bundle adjustments since a scale bar is often employed in high precision applications.

The plane test field has an extent of 3 by 5 meters and includes 68 points. For the bundle network, 16 camera stations were selected, as can be seen in Figure 5.7. The virtual camera, which was used to generate the images, is equivalent to a Kodak DCS 420 (resolution of 1524 x 1012 pixels) using a 20.5 mm lens.

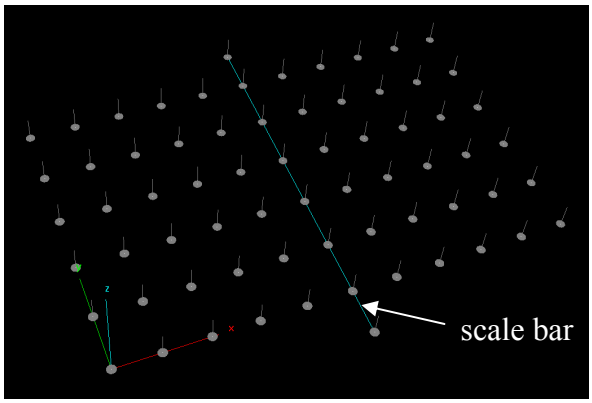

Figure 5.6: Plane test field (3m x 5m) with 68 points, including target normal and scale bar

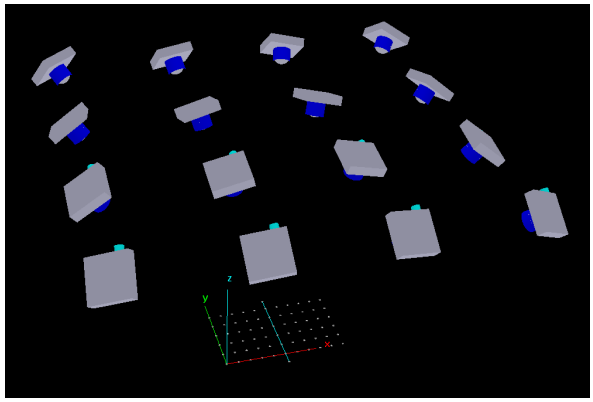

Figure 5.7: Configuration of the camera stations

The calculations were carried out with three different target sizes: r = 5 cm (Figure 5.6), r = 7 cm and r = 10 cm. The results are numerically listed and visually illustrated below.

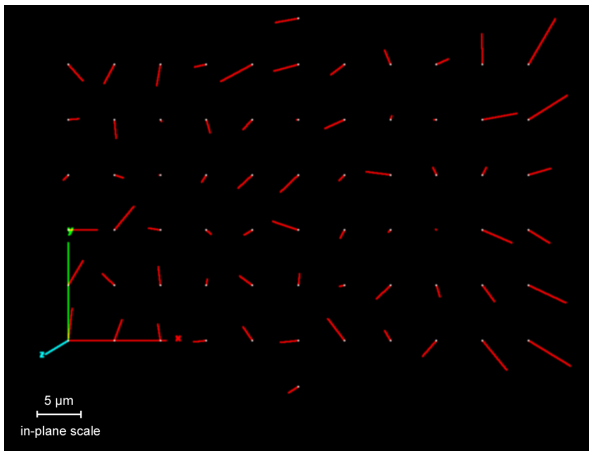

Figure 5.8: Discrepancy vectors 100,000 times inflated (5 cm target radius)

	Mean	Max
Average target radius within the images [pixel]	8.7	13.6
Average discrepancy in object space [µm]	2.7	6.1

Table 5.1: Numerical results (5 cm target radius)

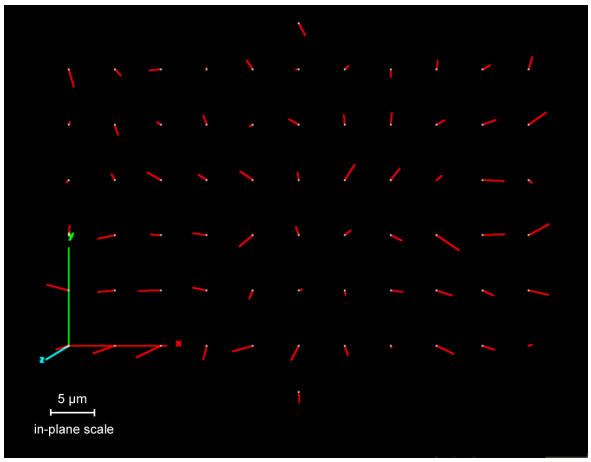

Figure 5.9: Discrepancy vectors 100,000 times inflated (7 cm target radius)

	Mean	Max
Average target radius within the images [pixel]	12.1	19.1
Average discrepancy in object space [µm]	1.7	4.7

Table 5.2: Numerical results (7 cm target radius)

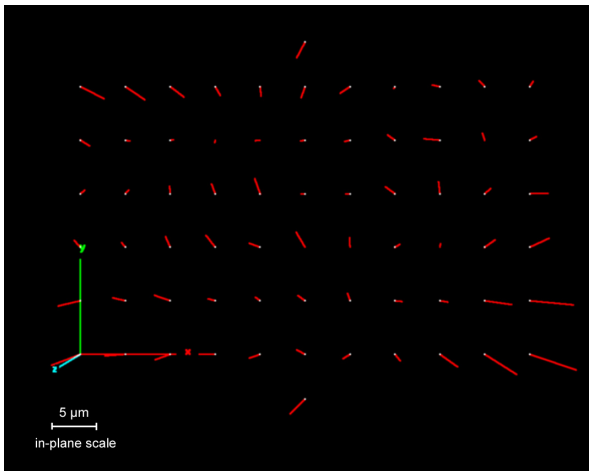

Figure 5.10: Discrepancy vectors 100,000 times inflated (10 cm target radius)

	Mean	Max
Average target radius within the images [pixel]	17.3	27.3
Average discrepancy in object space [µm]	1.9	6.1

Table 5.3: Numerical results (10 cm target radius)

From Figure 5.8 to Figure 5.10 the increase of the systematic part within the discrepancy vectors is clearly visible. For completeness it should be mentioned that the discrepancy vectors are three-dimensional which causes a warping of the plane test field. The three computational examples point up the conflict of choosing the correct target size for high precision applications as in today's VM systems. On the one hand, big targets are preferred to achieve accurate centroids. On the other hand, bigger targets cause bigger eccentricities. Hence, one has to find the ideal target size which results in the lowest errors if the eccentricity is not corrected. In this example, the 7 cm targets would deliver the best results.

Using quality photogrammetric equipment, typical triangulation accuracies of 1:100 000 can be obtained (Fraser 1997). In the case of this 5 m object, object point accuracies of 50 µm should be achievable. Hence, from a practical point of view, the size of the discrepancies can neglected in this or similar surveys.

Concluding this planar test field analysis, some remarks about the exterior orientation of the camera stations and the self-calibration should be made. A comparison of the changes of the projection centre coordinates was performed and the results are listed in Table 5.4. Additionally, the corresponding focal length resulting from the self-calibration is listed in the table.

Shift of projection centres	Mean [mm]	Max [mm]	Calibrated focal length c [mm]
5 cm targets	0.4	0.6	20.4995
7 cm targets	0.8	1.1	20.4990
10 cm targets	1.7	2.3	20.4982

Table 5.4: Differences between projection centre coordinates from the bundle adjustment and the original error-free values, and the corresponding focal length from the self-calibration

It can be clearly seen that the listed estimated EO parameters in the bundle adjustment 'drift away' from the original values with increasing target size. This effect is only caused by the eccentricity.

Errors within the exterior orientations are usually negligible within practical applications since this information is mostly ignored. However, in some applications the distorted self-calibration could lead to further errors within the intersection/resection process.

5.3. Eccentricity Effect on a Parabolic Antenna

The inspection of antennas is a common high-precision application of VM. Parabolic antennas are used for communication with satellites and spacecraft, as well as for exploration of the universe using radio telescopes. Hence, it is very useful to investigate the eccentricity effect on such a network.

The chosen antenna has a diameter of 1.4 m. 87 points were used to characterise the parabolic surface. As can be seen in Figure 5.12, 16 cameras stations were selected for the computations. The technical data of the virtual camera are similar to the first case. With a resolution of 1536 x 1024 pixels (pixel size 9 x 9 µm) and a 20 mm lens, the camera is equivalent to a GSI INCA 1.

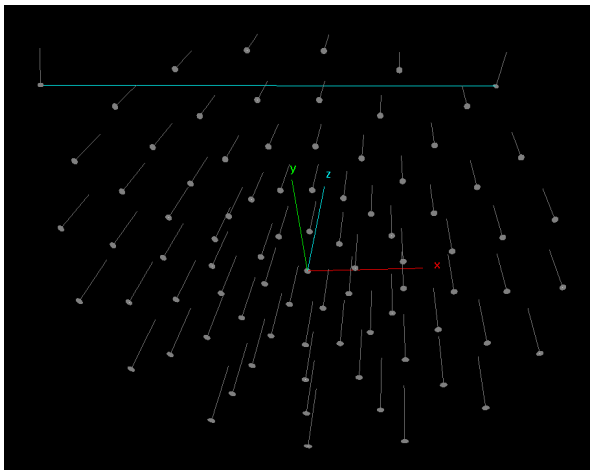

Figure 5.11: Arrangement of object points including target normals and scale bar (1.5 m)

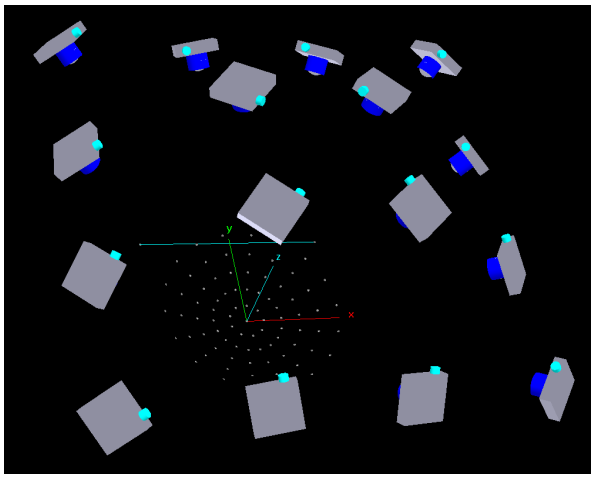

Figure 5.12: Configuration of the camera stations

Similar to the first test field analysis the calculations were performed with three different target sizes: r = 5 mm, r = 10 mm (Figure 5.11) and r = 20 mm. The results are given below, with the discrepancy vectors being inflated 10,000 times within the graphical views.

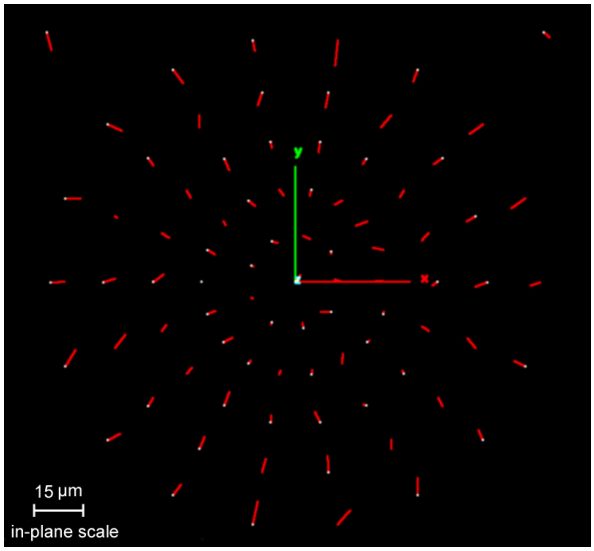

Figure 5.13: Discrepancy vectors 10,000 times inflated (5 mm target radius)

	Mean	Max
Average target radius within the images [pixel]	3.2	4.5
Average discrepancy in object space [µm]	3.6	7.3

Table 5.5: Numerical results (5 mm target radius)

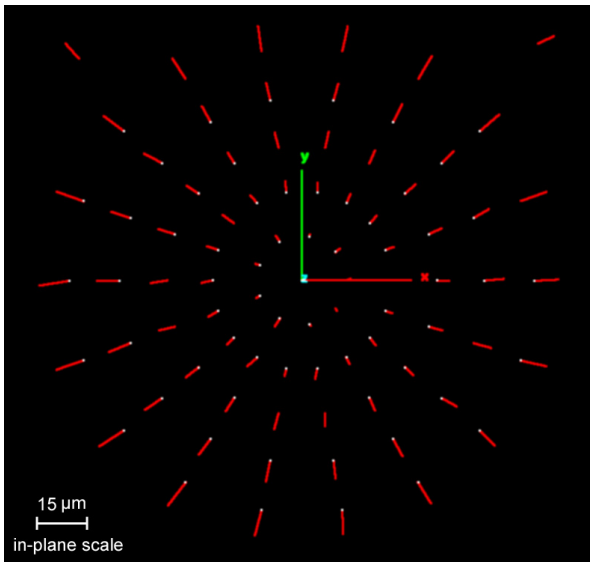

Figure 5.14: Discrepancy vectors 10,000 times inflated (10 mm target radius)

	Mean	Max
Average target radius within the images [pixel]	6.3	9.0
Average discrepancy in object space [µm]	5.6	10.4

Table 5.6: Numerical results (10 mm target radius)

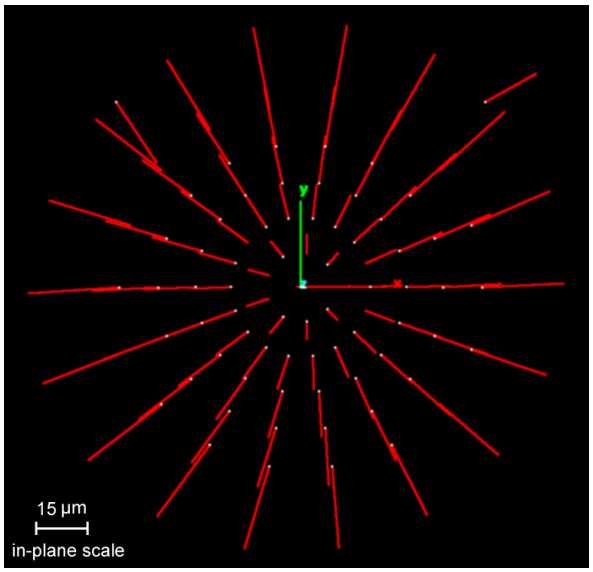

Figure 5.15: Discrepancy vectors 10,000 times inflated (20 mm target radius)

	Mean	Max
Average target radius within the images [pixel]	12.6	18.0
Average discrepancy in object space [µm]	22.1	47.9

Table 5.7: Numerical results (20 mm target radius)

In comparison to the planar test field case, it can be seen that there is a much higher distortional effect of the eccentricity considering equal target radii within the images. Applying the triangulation accuracy, a standard deviation of 15 µm for object points could be expected. Hence,

the target radius of 20 mm is clearly too big (average discrepancy exceeds 20 µm) if the observations are not compensated for the eccentricity. Already the 10 mm targets define the target size limit since the discrepancies reach up to 10 µm and in this simulation no other errors, as they appear in real applications, are considered.

A side view (Figure 5.16) of the discrepancies (20 mm targets) shows a clear systematic trend which would lead to an incorrect estimation of the focal length of the parabolic antenna.

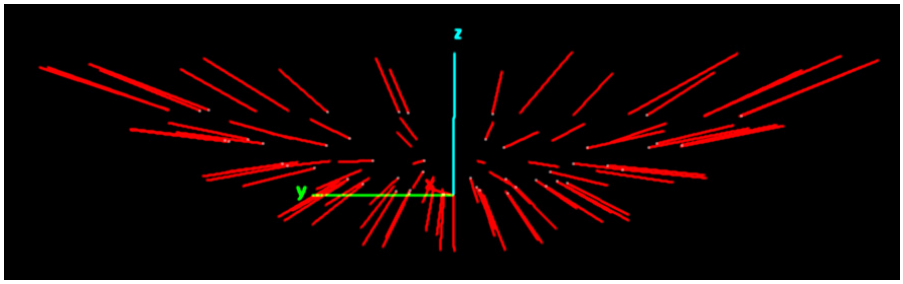

Figure 5.16: Side view of discrepancies (20 mm targets)

To check this visual assessment, a best-fit adjustment was performed and its results are listed in Table 5.8. As can be seen, the eccentricity causes an underestimation of the focal length. In the 20 mm target case, the error in the focal length is clearly outside the acceptable accuracy range.

	Focal length [mm]
Original error-free value	612.000
5 mm targets	611.996
10 mm targets	611.994
20 mm targets	611.799

Table 5.8: Focal length estimated from the final computed object point coordinates

The next test field analysis will consider the eccentricity effect on a cylinder combined with a 360 degree survey.

5.4. Eccentricity Effect on a Cylindrical Hull

The following test field analysis investigates the distortional eccentricity effect on a cylindrical hull which requires a 360 degree arrangement of the camera stations. A total of 36 view points were used to simulate the network of 52 object points. The selected cylindrical hull has a length of 1 m and a diameter of 0.5 m. The point arrangement and the chosen camera stations can be seen in Figures 5.17 and 5.18.

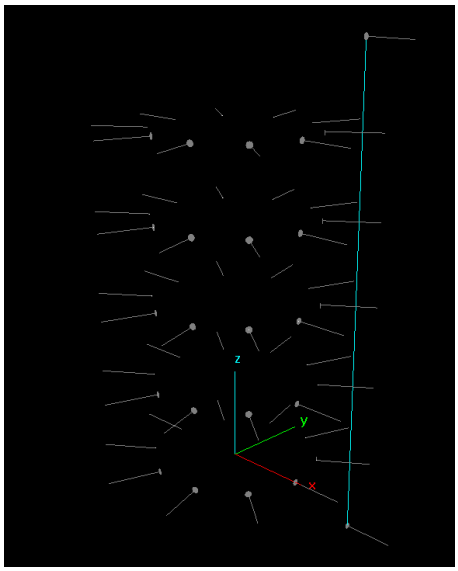

Figure 5.17: Cylindrical hull including target normals and scale bar (1.5 m)

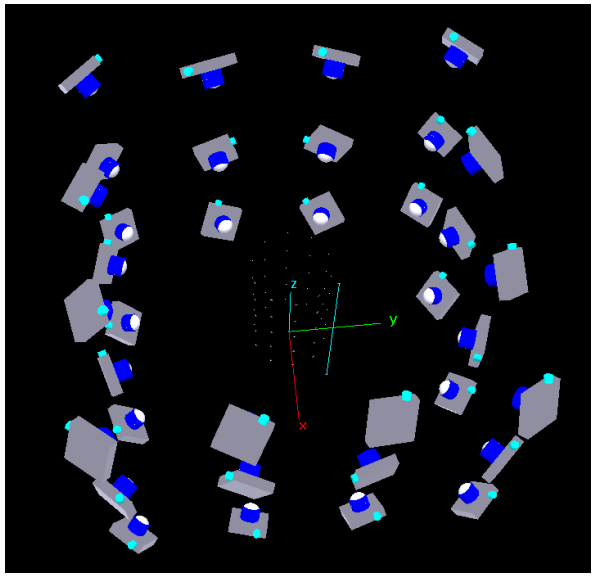

Figure 5.18: Configuration of the camera station

This time a camera with a higher resolution of 3000 by 2000 pixels (pixel size 9 x 9 µm) was taken to simulate the images. The resolution of 6 MegaPixels is typical for present-day high quality cameras.

The higher resolution of the virtual camera allows the use of smaller target. For simulation of the current test field network, the three target radii of 1 mm, 3 mm and 5 mm were used. The resulting discrepancy vectors are illustrated in Figures 5.19 to 5.21.

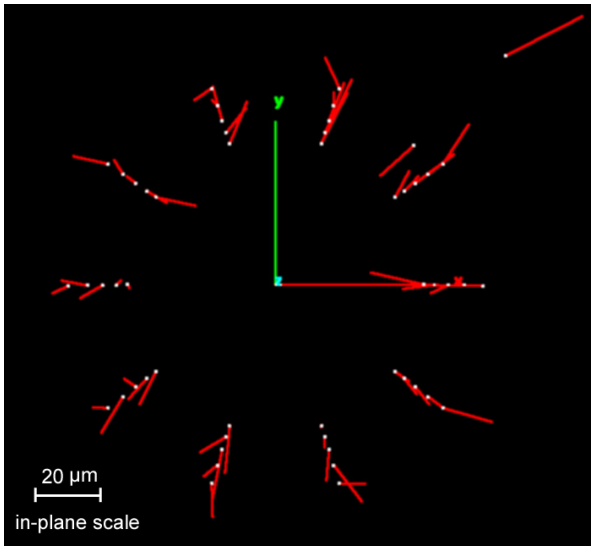

Figure 5.19: Discrepancy vectors 5,000 times inflated (1 mm target radius)

	Mean	Max
Average target radius within the images [pixel]	1.4	2.4
Average discrepancy in object space [µm]	10.3	19.8

Table 5.9: Numerical results (1 mm target radius)

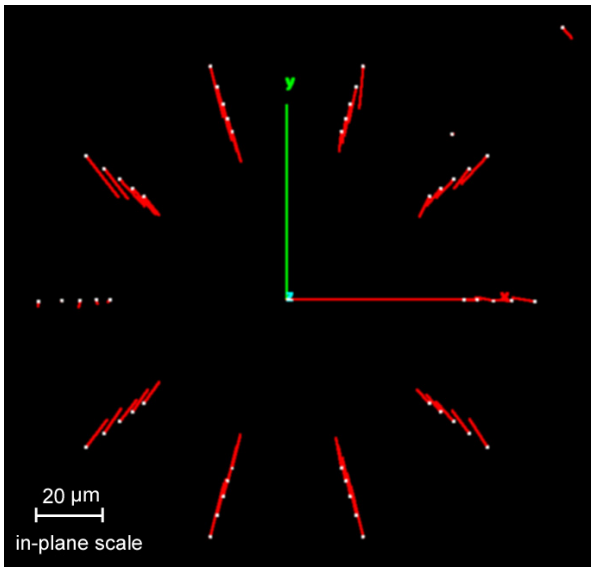

Figure 5.20: Discrepancy vectors 5,000 times inflated (3 mm target radius)

	Mean	Max
Average target radius within the images [pixel]	4.3	7.3
Average discrepancy in object space [µm]	6.9	11.2

Table 5.10: Numerical results (3 mm target radius)

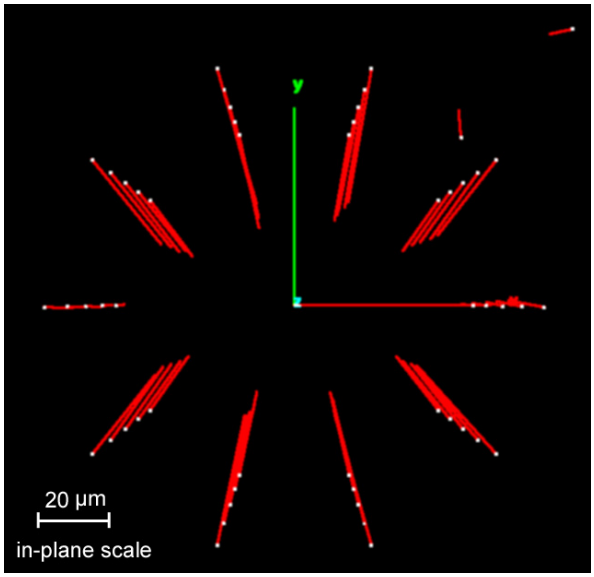

Figure 5.21: Discrepancy vectors 5,000 times inflated (5 mm target radius)

	Mean	Max
Average target radius within the images [pixel]	7.2	12.2
Average discrepancy in object space [µm]	18.6	28.3

Table 5.11: Numerical results (5 mm target radius)

Applying the triangulation accuracy rule, an object point precision of 10 µm could be expected from this network, which will be difficult to achieve as Table 5.9 to Table 5.11 show. One reason for the 'low' accuracy is the small amount and the low coverage of the object points in each image. Consequently more targets would be placed in a real application, especially on the surrounding of the cylindrical hull. For clearness of the discrepancy plots this extra data has been omitted. Nevertheless, a clear systematic trend can already be seen in the discrepancies of 3 mm targets (Figure 5.20), and using 5 mm targets the expected precision is clearly unattainable, if the eccentricity is not considered within the bundle adjustment.

Similar to the parabolic antenna project, the eccentricity will cause an incorrect estimation of the cylinder radius if it is derived from the final object point coordinates. As can be seen in Table 5.12, the network with 5 mm targets delivers a significantly underestimated radius of the cylindrical hull.

	Cylinder radius [mm]
Original error-free value	250.000
1 mm targets	250.004
3 mm targets	249.993
5 mm targets	249.981

Table 5.12: Cylinder radius estimated from the final iterated object point coordinates

In the following an interpretation of the results of the three different test fields cases, always using the biggest target size, will be made. In Table 5.13 the ratio of the average discrepancy to the triangulation accuracy is listed, as well as the average target radius within the images. Although the target size decreases within the images, the object point precision gets worse. Since the variation of the target normal increases from the first to the last test field, it may be concluded that the distortional effect of the eccentricity is higher in networks with a higher variation of target orientation.

	average discrepancy / expected triangulation accuracy	average target radius within the images [pixel]
Plane test field (10 cm targets)	0.04	17.3
Parabolic antenna (20 mm targets)	1.47	12.6
Cylindrical hull (5mm targets)	1.86	7.2

Table 5.13: Results of the first three test fields summarized

To verify this conclusion two more test field cases employing a higher degree of target orientation variation were investigated. The results from these simulations are presented in the following section.

5.5. Eccentricity Effect on a Sinus-Shaped Surface

The selected sinus-shaped surface has an extent of 5 by 3 meters. Similar to the planar test field 16 camera stations were used to image the 68 object points. The adopted virtual camera (1524 x 1012 pixels, 9 x 9 µm pixel size and 20.5 mm lens) is identical to the camera of the first test field case. As was presented from the first three cases, Figures 5.22 and 5.23 indicate the network configuration.

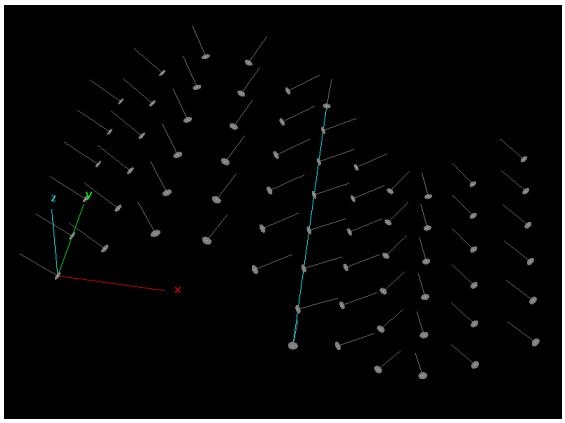

Figure 5.22: Sinus-Shaped surface including target normals and 4 m scale

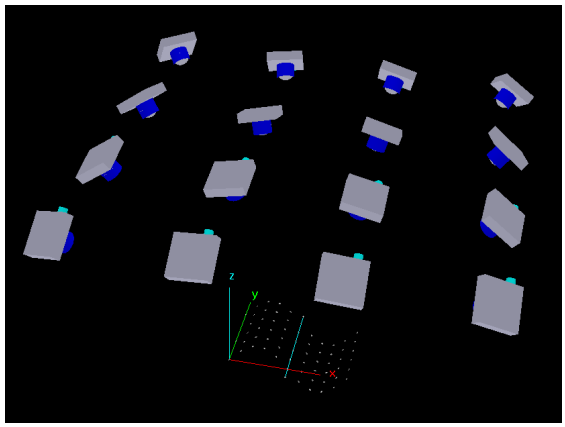

Figure 5.23: Configuration of camera stations

Again, the computations were performed with 3 three different target sizes. Radii of 30 mm, 50 mm (Figure 5.22) and 70 mm were employed. The resulting discrepancy vectors are illustrated and numerically summarised below.

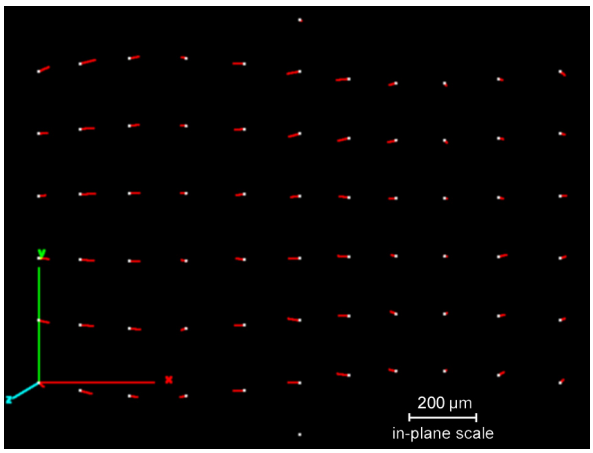

Figure 5.24: Discrepancy vectors 3,000 times inflated (30 mm target radius)

	Mean	Max
Average target radius within the images [pixel]	5.3	8.6
Average discrepancy in object space [µm]	29.5	49.1

Table 5.14: Numerical results (30 mm target radius)

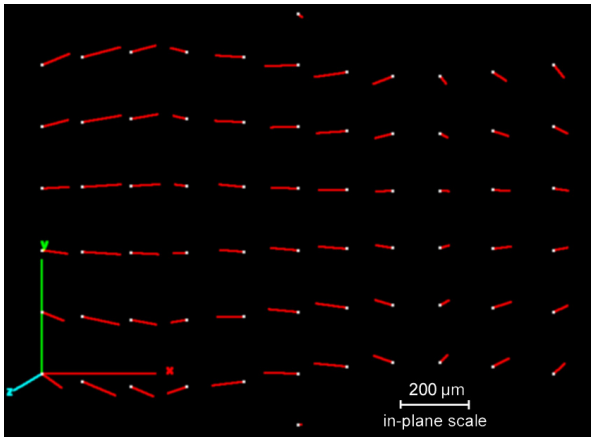

Figure 5.25: Discrepancy vectors 3,000 times inflated (50 mm target radius)

	Mean	Max
Average target radius within the images [pixel]	8.9	14.3
Average discrepancy in object space [µm]	78.7	123.7

Table 5.15: Numerical results (50 mm target radius)

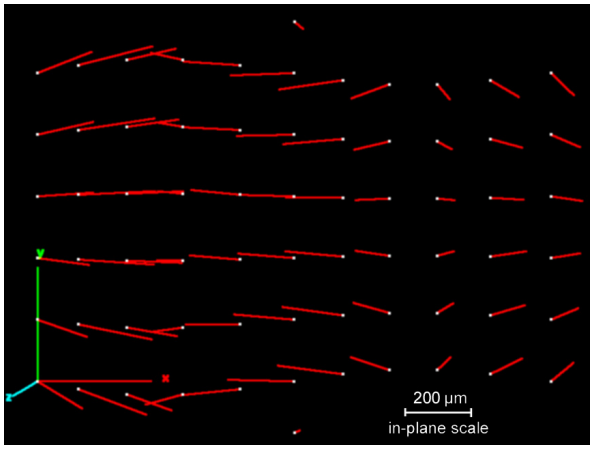

Figure 5.26: Discrepancy vectors 3,000 times inflated (70 mm target radius)

	Mean	Max
Average target radius within the images [pixel]	12.5	20.1
Average discrepancy in object space [µm]	156.0	242.8

Table 5.16: Numerical results (70 mm target radius)

Considering the triangulation geometry, an object point precision of 50 µm is expected. As can be seen in Table 5.14, the target size of 30 mm is already the upper limit if the expected accuracies are to be achieved. This is supported by Figure 5.24 where a clear systematics trend of the discrepancy vectors is visible. Similar to the first three test field projects, the eccentricity effect would lead to a distorted curvature if parameters of the surface were estimated from the object point coordinates, as indicated in Figure 5.27.

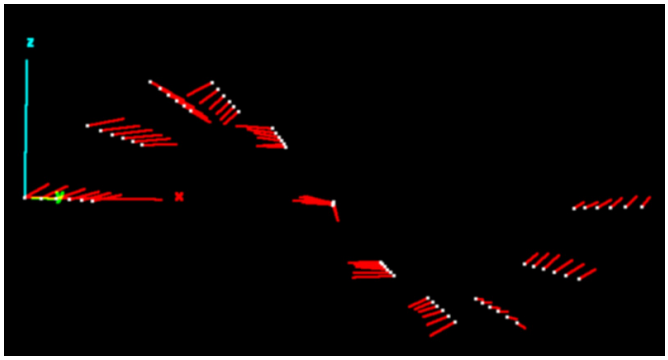

Figure 5.27: Side view of discrepancies (3,000 times inflated) of the 50 mm project

The results of this test field case support the contention that the distortional effect of the eccentricity is higher on networks with a higher variation in target orientation. It will be shown in the following and final simulation, that the geometry of the network plays a minor role for the distortion.

5.6. Eccentricity Effect on a Rough Plane Test Field

The network geometry of this final simulation case is identical to the first, plane test field. Whereas in the first test field simulation the target normals were all parallel to the z-axis, the targets in this case are orientated randomly. As can be seen in Figure 5.28, the target normals include angles between 0 and 34 degrees with respect to the z-axis (average angle is about 20 degrees).

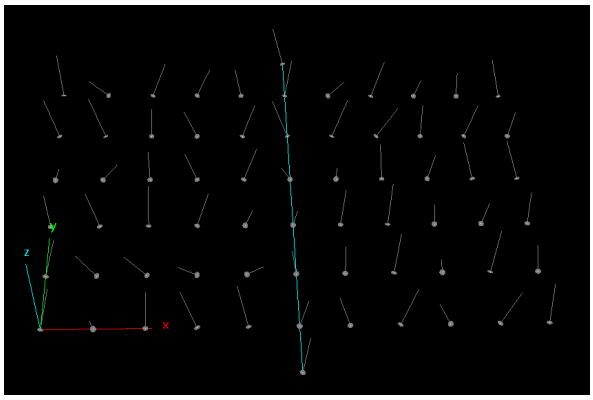

Figure 5.28: Test field (3m x 5m) with 68 points, including target normal and scale bar

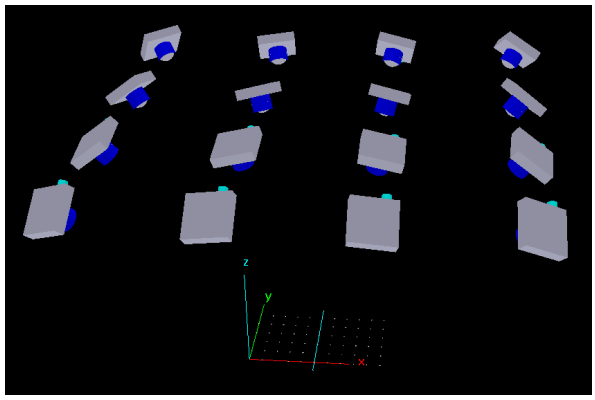

Figure 5.29: Configuration of camera stations

Such a surface point arrangement will not appear very often in real applications since in the case of such a rough surface the chosen point density would be much higher. However, the comparison of this simulation with the results of the first, planar network will show how much the eccentricity distortion is influenced by the variation in the target normals.

The employed virtual camera is identical to the one which was used in the first simulation test field (1524 x 1012 pixels, 9 x 9 µm pixel size and 20.5 mm lens). Again, three different target radii (30 mm, 50 mm and 70 mm) were used. The resulting discrepancy vectors are illustrated and numerically listed in the following.

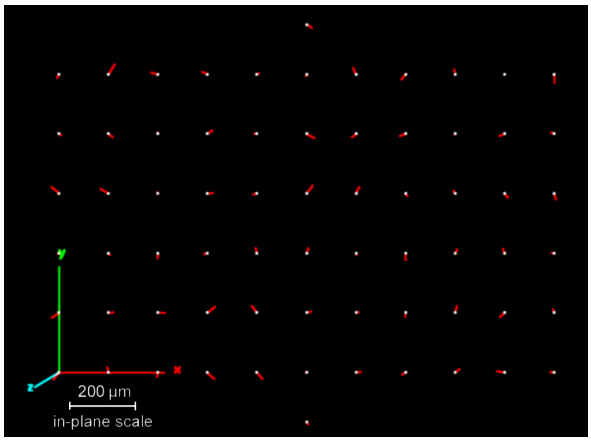

Figure 5.30: Discrepancy vectors 3,000 times inflated (30 mm target radius)

	Mean	Max
Average target radius within the images [pixel]	5.2	7.7
Average discrepancy in object space [µm]	20.6	41.4

Table 5.17: Numerical results (30 mm target radius)

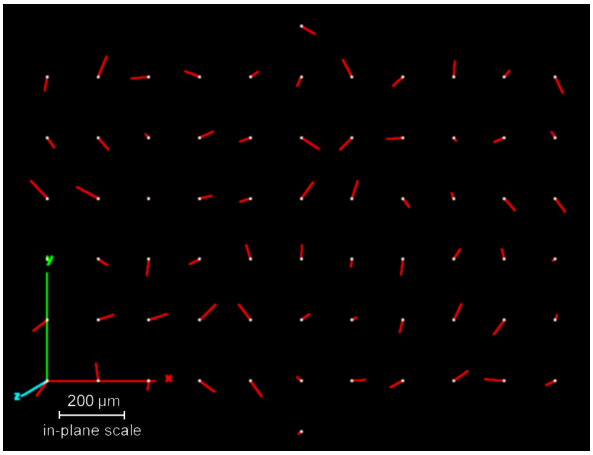

Figure 5.31: Discrepancy vectors 3,000 times inflated (50 mm target radius)

	Mean	Max
Average target radius within the images [pixel]	8.1	12.8
Average discrepancy in object space [µm]	50.2	89.2

Table 5.18: Numerical results (50 mm target radius)

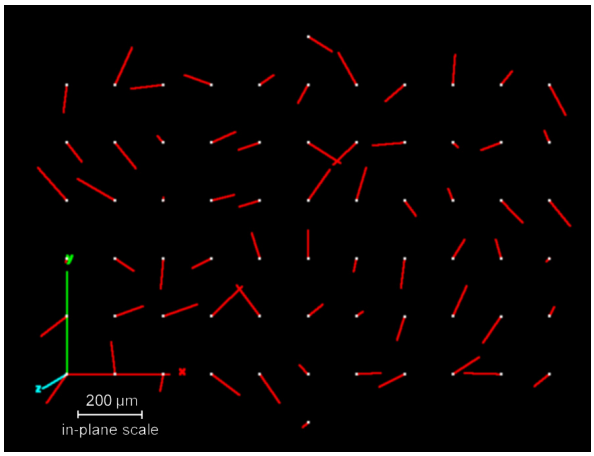

Figure 5.32: Discrepancy vectors 3,000 times inflated (70 mm target radius)

	Mean	Max
Average target radius within the images [pixel]	11.4	17.9
Average discrepancy in object space [µm]	97.8	175.0

Table 5.19: Numerical results (70 mm target radius)

Compared to the previous simulations no clear systematic trend is visible in the plots of discrepancy vectors shown in Figures 5.30 to 5.32. This should not come as a surprise since the orientation of the targets were randomly selected. However, there is a high level of correspondence between the vector distribution in the three figures shown above.

Considering the typical triangulation precision of 1:100,000 an object point accuracy of 50 µm would be expected. Comparing the result with the sinus-shaped surface test field, the distortional effect of the eccentricity is about 1/3 lower. Another interesting comparison can be made with the first, planar test field case. Though the network configuration is identical, the first simulation did not show any relevant distortion of the object point coordinates, whereas the current test field has generated a very noticeable eccentricity effect. This demonstrates that the eccentricity distortion is mainly dependent on the variation of the target orientation.

In summarising the interpretation of results of the five simulated test field cases, it has been shown that eccentricity effects in the bundle adjustment can lead to significantly distorted object point coordinates which are not detectable from the results of the adjustment itself. Eccentricity effects should therefore not be ignored in high accuracy VM. There are two factors which mainly influence the degree of distortion: the average size of the target within the images and the variation of the target orientation. Since the target planes are defined by the surveying object, the photogrammetrist has only the possibility of choosing the appropriate target size. Using the above presented results, the following rule for the target size can be derived if a photogrammetric system, which cannot correct for the eccentricity, is employed. To achieve the typical triangulation accuracy of 1 part in 100 000 the average target radius within the images should not exceed 4 pixels (8 pixel diameter). If this rule is applied for any survey it will ensure that the distortional effect of the eccentricity is within the expected measuring precision. However, continuing improvements in digital cameras (e.g. higher resolutions of the CCD chips) may require a refinement of this rule in the near future.

In addition, it should be recalled that the object point coordinates are not the only distorted parameter within the bundle adjustment (see Chapter 5.2). The estimates of the exterior orientation and the focal length can be substantially affected as well. Since this is of no concern in a typical surface inspection application, a detailed analysis of this effect has not been considered here. However, surveying strategies were unwanted deformation may appear can be envisaged.

6. Curved Targets and their Distortional Effect

If a photogrammetry system is capable of correcting the ellipse eccentricity, no restriction concerning the target size needs to be made. Bigger targets resulting in higher centroiding accuracies can be employed, which will eventually lead to better surveying precision. In some applications, however, limitations in the target size may be a requirement due to point density or due to the curvature of the surface to be surveyed. So far circular targets have always been considered as perfect planar circles in space. However, if a target is glued onto a surface, the planarity of the target edge is not guaranteed in general and it is convincing that bigger targets are more effected by the surface curvature than smaller. Since this thesis proposes the use of bigger targets for higher accuracy, it is well worth investigating the effect of curved targets on the measuring process. The derivation of the required formulas and an estimation of the effect will be described in this chapter.

For completeness, it should be mentioned that there are target size limitations from a practical point of view as well. Retro-reflective targets on rolls are usually manufactured only to a certain diameter. Additionally, bigger targets are more difficult to attach to the surface free of air bubbles.

Considering rigorousness, a target can be glued on a surface without folding only if the current part of the surface can be developed into a plane. Hence, planes, cones and cylinders are imaginable target positions. Since the carrier material of a retro-reflective target is usually flexible, the targets can also be affixed to other surfaces which describe the aforementioned surfaces only by approximation. This is of minor concern for the following derivations, because here it is only estimated how much curvature depending on target size is acceptable considering a given measuring precision. Also, only cylinders are considered since other conic surfaces will show similar distortional effects.

6.1. Derivations for Cylindrical Curved Targets

6.1.1. Continuous Derivations

To analyse the distortional effect of a target which is fixed on a cylindrical surface, a mathematical description of the target edge has to be found. To simplify the matter, the coordinate system was selected as indicated in Figure 6.1, where the origin was set to the target centre and the z-axis was selected parallel to the cylinder axis.

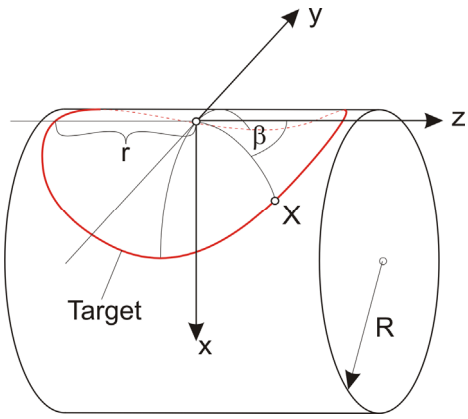

Figure 6.1: Circular target wrapped around a cylinder

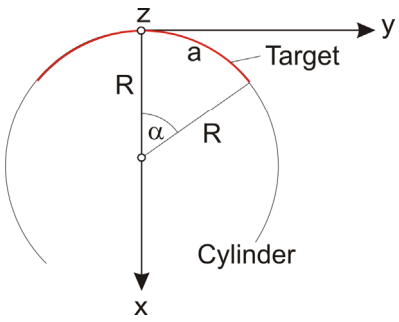

Figure 6.2: Side view of cylindrical target

If a parametric description can be found, it is simple to project the formula into images space. If the cylinder radius R is infinite, the target edge can be described by

$$\mathbf{X} = \begin{pmatrix} x \\ y \\ z \end{pmatrix} = \begin{pmatrix} 0 \\ r\sin\beta \\ r\cos\beta \end{pmatrix} \tag{6.1}$$

where r is the radius of the target and β is the curve parameter. In the case of a finite cylinder radius R, equation (6.1) has to be transformed. However, the z-coordinate does not change since the cylinder has no curvature in the direction of the z-axis. As can be seen in Figure 6.2, the length of the arc a has to be equal to y in equation (6.1) so that the circle condition is still fulfilled.

$$a = r\sin\beta \quad \Rightarrow \quad \alpha = \frac{r\sin\beta}{R} \tag{6.2}$$

Since r << R, x can be described and developed in a series expansion as follows

$$\begin{aligned} x &= R - R\cos\alpha = R\left(1-\cos\left(\frac{r\sin\beta}{R}\right)\right) = R\left(1-\left(1-\frac{r^2\sin^2\beta}{2!R^2}+\ldots\right)\right) \\ x &\approx \frac{r^2\sin^2\beta}{2R} \end{aligned} \tag{6.3}$$

The series expansion eliminates the recursion of trigonometric functions, which simplifies further derivation. The error which is made by the approximation is small for small angles α. This is secured by the expectation that the cylinder radius R will be bigger than the target radius r. A similar approach can be employed for the y-coordinate, which is defined by

$$y = R\sin\alpha = R\sin\left(\frac{r\sin\beta}{R}\right) \tag{6.4}$$

However, a series expansion of equation (6.4) would eliminate the condition that the curve is positioned on the hull of the cylinder. Using the cylinder equation and the approximation for x, it is possible to secure the cylinder condition without the unwanted trigonometric function recursion, as is apparent in equation (6.4).

$$(x-R)^2 + y^2 = R^2 \quad \Rightarrow \quad y^2 = 2Rx - x^2 \tag{6.5}$$

$$y \approx \pm\sqrt{r^2 \sin\beta - \frac{r^4 \sin^4\beta}{4R^4}} = r\sin\beta\sqrt{1 - \frac{r^2 \sin^2\beta}{4R^2}} \tag{6.6}$$

Theoretically, it is possible to approximate y first and then use the cylinder equation to express x. As numerical analysis shows, the presented approach delivers much more accurate results. In the case of R = 2r the 3D distance approximation error reaches a maximum of only 1 % of the target radius. Hence, employment of the approximated equation of the distortion estimation is allowed. Summarising equations (6.1) to (6.6), the target edge of a circular target on a cylindrical surface can be described by

$$\mathbf{X} = \begin{pmatrix} R - R\cos\left(\frac{r\sin\beta}{R}\right) \\ R\sin\left(\frac{r\sin\beta}{R}\right) \\ r\cos\beta \end{pmatrix} \approx \begin{pmatrix} \frac{r^2\sin^2\beta}{2R} \\ r\sin\beta\sqrt{1 - \frac{r^2\sin^2\beta}{4R^2}} \\ r\cos\beta \end{pmatrix} \tag{6.7}$$

As the 3D view of the approximated curve in Figure 6.3 shows, the curve is perfectly positioned at the cylinder surface, as modelled by equation (6.5).

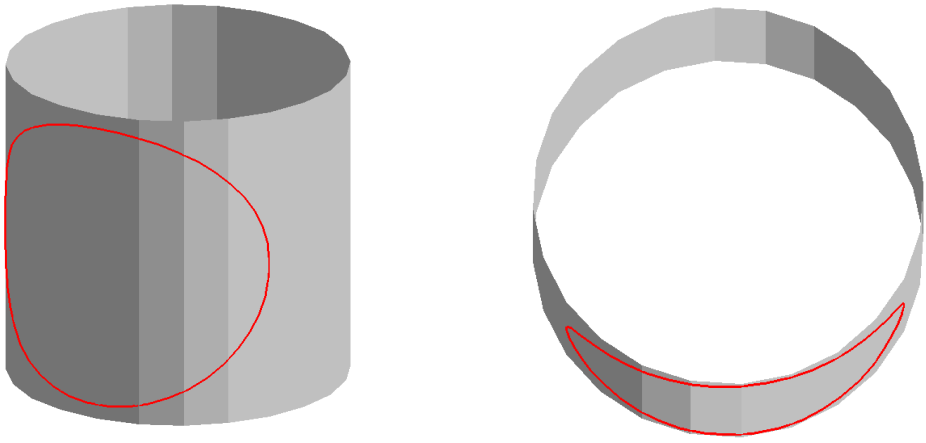

Figure 6.3: 3D view of approximated curve with the corresponding cylinder (R= r = 10 mm)

The transformation of equation (6.7) into image space is simply done by applying the collinearity condition (3.2). To perform the distortion estimation, a package of functions was implemented within the mathematical software *Maple* (*Maplesoft*, 2004). Using this package, it is easy to analyse certain target-image-configurations and display the results through figures. As an example, a typical configuration was selected and computed. The applied virtual camera had a focal length of 15 mm and an image area of 27 x 18 mm (represents CCD chip with 3000 x 2000 pixels and a pixel size of 9 x 9 µm). The distance between the target and the project centre was about 4.9 m and the target radius was 10 mm. The selected orientation of the camera station projected the target into the

upper-left corner of the image. The computations were repeated three times using three different cylinder radii (100 mm, 50 mm and 10 mm). The results can be seen in Figures 6.4 to 6.6. Beside the target edge (black solid curve), the corresponding best-fit ellipse (grey dashed curve) can be seen. Additionally, the real target centre (black solid circle), the centroid of the target edge (black spot) and the ellipse centre (grey dashed circle) are displayed. Whereas the ellipse centre and the centroid are nearly identical in all figures, the real target centre clearly moves to the left from Figures 6.4 to 6.6.

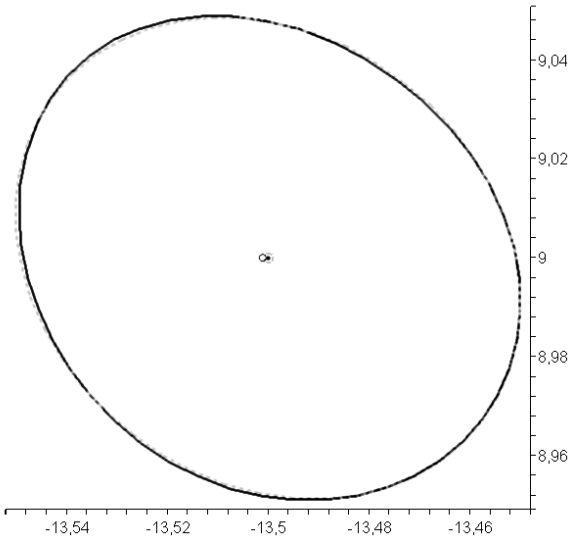

Figure 6.4: Target image using 100 mm cylinder radius

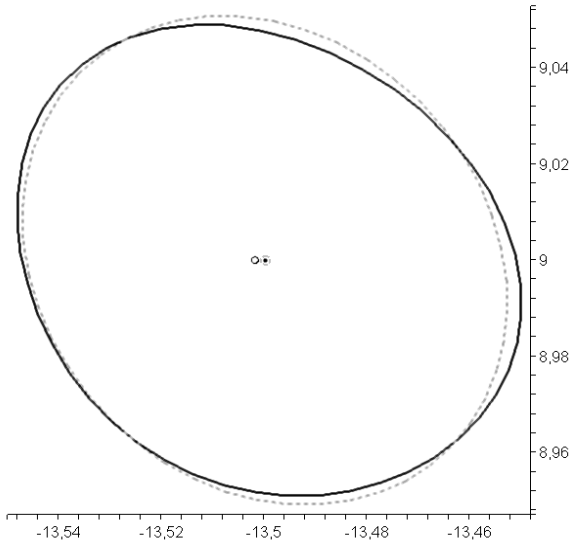

Figure 6.5: Target image using 50 mm cylinder radius

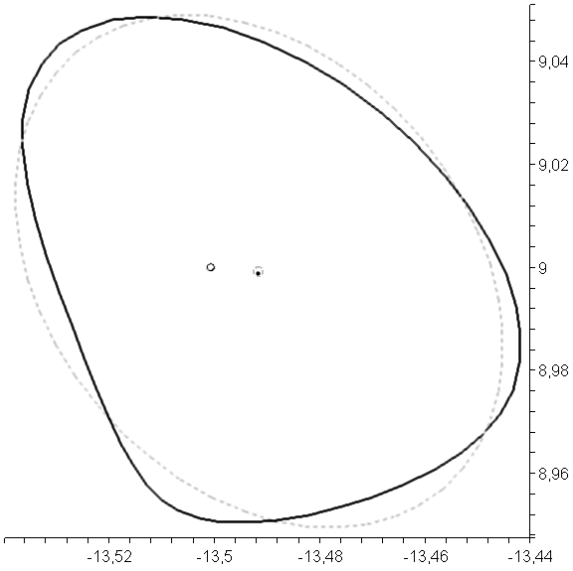

Figure 6.6: Target image using 10 mm cylinder radius

This first simulation already reveals the interesting fact that, even in the case of targets with curved surfaces, equivalent results are obtained using either the centroid of the target edge or the centre of the best-fit ellipse.

Since digital images comprise discrete pixel values with no continuous function, it is only partly meaningful to estimate distortional effect of curved targets by the above presented formulas. Hence, the *Maple* package was extended by rasterising functions. This is described in the following section.

6.1.2. Discrete Derivations

To achieve realistic estimates of the accuracy of bent targets (those with curved surfaces) within practical applications, it is necessary to rasterise the images of the continuous functions derived in the previous section. It has to be considered that on-axis illumination of targets will cause variation of the imaged target brightness, this depending upon the target orientation. The decisive factor is the angle between the viewing direction and the target normal. This well known characteristic is easy visible in real imagery, as indicated in Figure 6.7.

Figure 6.7: Changing brightness of retro-reflective targets on a cylindrical surface

The variable brightness effect will be analysed in detail for retro-reflective and plane white targets in the following. To do so, a survey project of each target type was carried out, including the developed target plane determination. Results of the Gaussian distribution fitting (see Chapter 4.2.2) and the viewing angle (i.e. the angle between the target centre-projection centre-vector and the target normal) were used as raw data for the investigation.

6.1.2.1. Intensity characteristics of retro-reflective targets

The test field, which was employed to investigate the intensity characteristics of retro-reflective targets, can be seen in Figure 6.8. The car door network, which comprised of 135 retro-reflective targets, was imaged with a GSI INCA camera using a ring flash to achieve high contrast images.

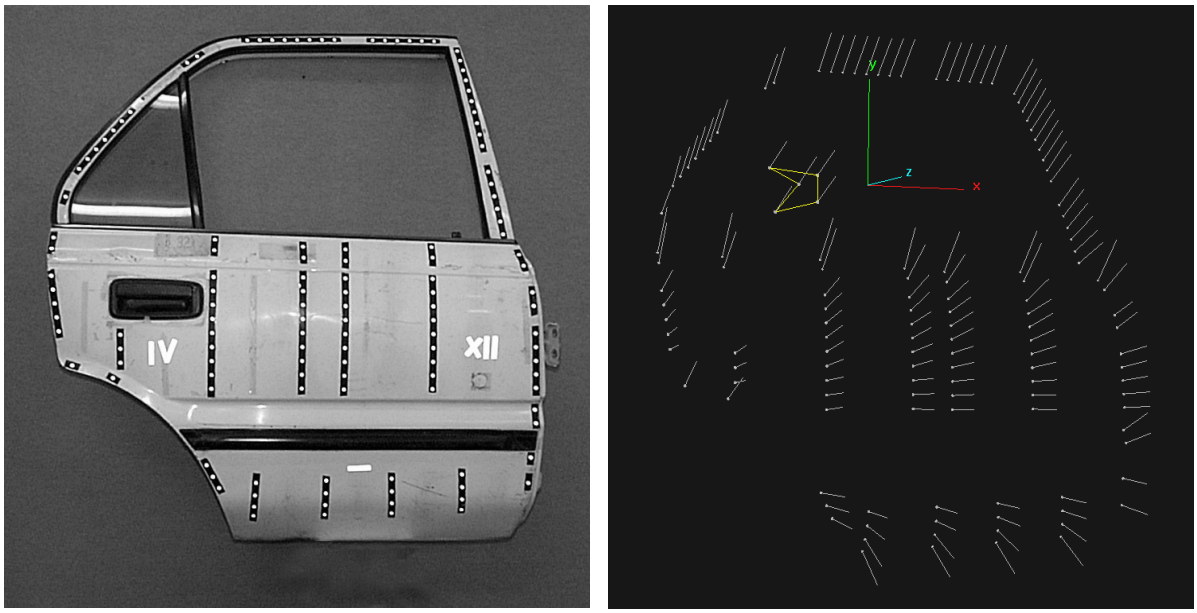

Figure 6.8: Test field for analysing the intensity characteristics of retro-reflective targets

In Figure 6.9, each ellipse is represented by a data point where the x coordinate is the viewing angle, as described above, and the y coordinate corresponds to the intensity factor of the target, which was computed by normalising the maximum brightness (defined by the scaling variable *s* in equation (4.18)) estimated in the 2D Gaussian distribution fitting. To simplify the matter, the normalisation process was performed for all images at once. Although an image-wise normalisation stage would result in a better overlap of the point from different images, the general characteristics of the intensity change are clearly visible and indicated as a black curve in Figure 6.9.

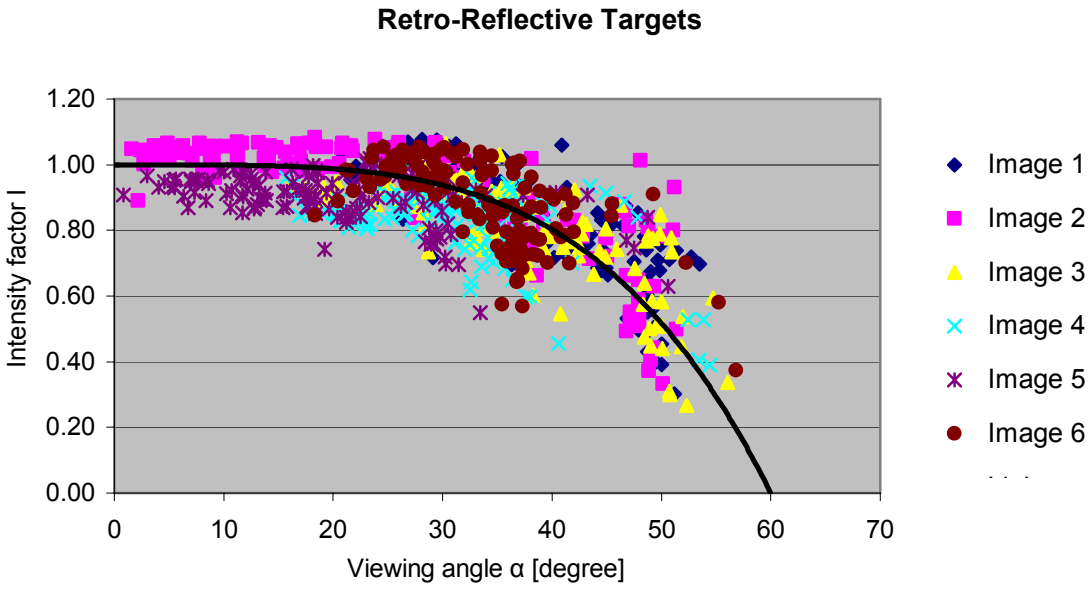

Figure 6.9: Intensity factor characteristics of retro-reflective targets, including best-fit curve

Retro-reflective targets show an interesting reflectivity behaviour. Between viewing angles of 0 to about 25 degrees, retro-reflective material returns nearly the same amount of light. Then the degree

of reflection slowly starts to decrease. At a viewing angle of 45 degrees the reflectivity is reduced to about 2/3. Half of the maximum reflection intensity is reached at about 50 degrees. And above 60 degrees there is essentially no reflection at all. The degradation of the intensity factor can be mathematically approximated by a polynomial of the 4th order, as it is was done in Figure 6.9.

$$I_{\text{RetroReflectiveTarget}} \approx -\frac{1}{60^4}\alpha^4_{[\text{degree}]} + 1 \tag{6.8}$$

It should be mentioned that a physical relationship of the intensity based on the irradiance within the image for Lambertian radiators exist (Kraus, 1996). This formula considers among other parameters the angle between the light source and the surface normal but also, the angle between the rays of the current image point and the principle point of the corresponding image. To simplify the matter only the viewing angle α was used to describe intensity degradation, as given by equation (6.8).

The distinctive intensity profile can be explained by the way light is reflected by retro-reflective material (the structure of retro-reflective targets is indicated in Figure 3.4). This physical process was intensively investigated by Zumbrunn (1995). If a glass sphere is viewed with a microscope using coaxial light, the sphere generates a bright ring with a small bright dot at the centre, whereas the centre dot can be neglected for the overall intensity (Figure 6.10). Zumbrunn determined the radius of the ring to be about 0.8 of the sphere radius.

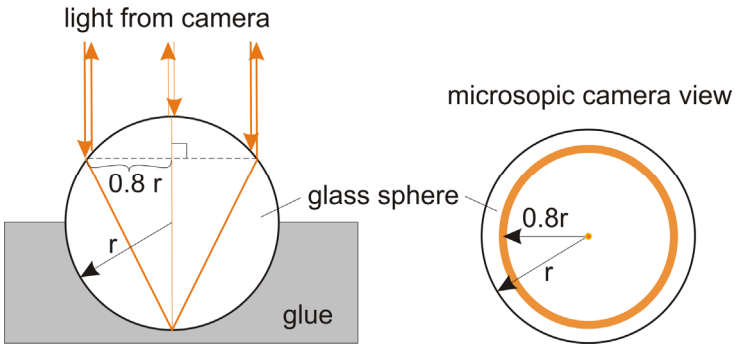

Figure 6.10: Physical process of light reflection at from a glass sphere

By applying this knowledge, it can be shown that the retro-reflective target delivers full reflection intensity, as long as the bright ring from each glass sphere is fully seen. After a certain viewing angle the glass spheres start occluding the bright rings of other spheres which causes the intensity reduction. Once more than half of each sphere is occluded, no further reflection will be visible, as indicated in Figure 6.11. This is why retro-reflective targets are visible to the low viewing angle of about 60 degrees only (always considering high contrast images).

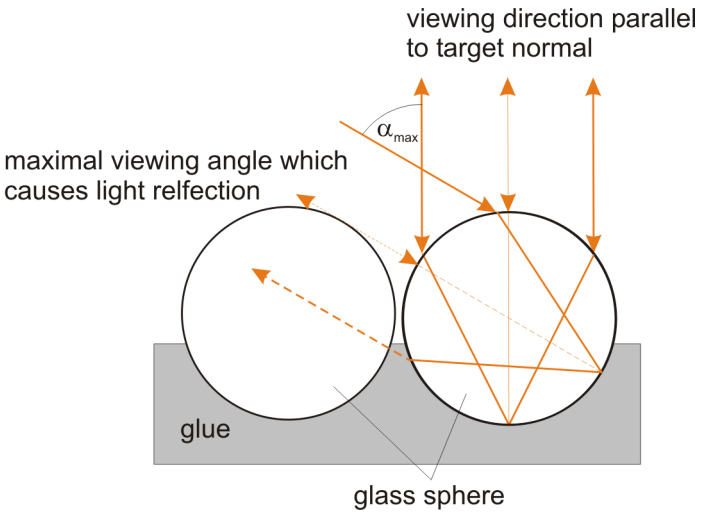

Figure 6.11: Maximal viewing angle which causes light reflection in the case of retro-reflective targets

For completeness, it should be mentioned that the intensity profile can vary for different retro-reflective materials. Intensity curve will remain as shown in Figure 6.9 of the reflectivity.

6.1.2.2. Intensity characteristics of plane white targets

The test field of 34 object points, which was used to estimate the characteristics of plane white targets, is illustrated in Figure 6.12. As before, a *GSI INCA* Camera was employed for the survey. Since the ring flash was not able to sufficiently illuminate the indoor test field, a different flash was used which produced brighter illumination. However, the flash was only partly able to homogeneously illuminate the test field. This can be seen in the left image of Figure 6.12, which was one of the project images.

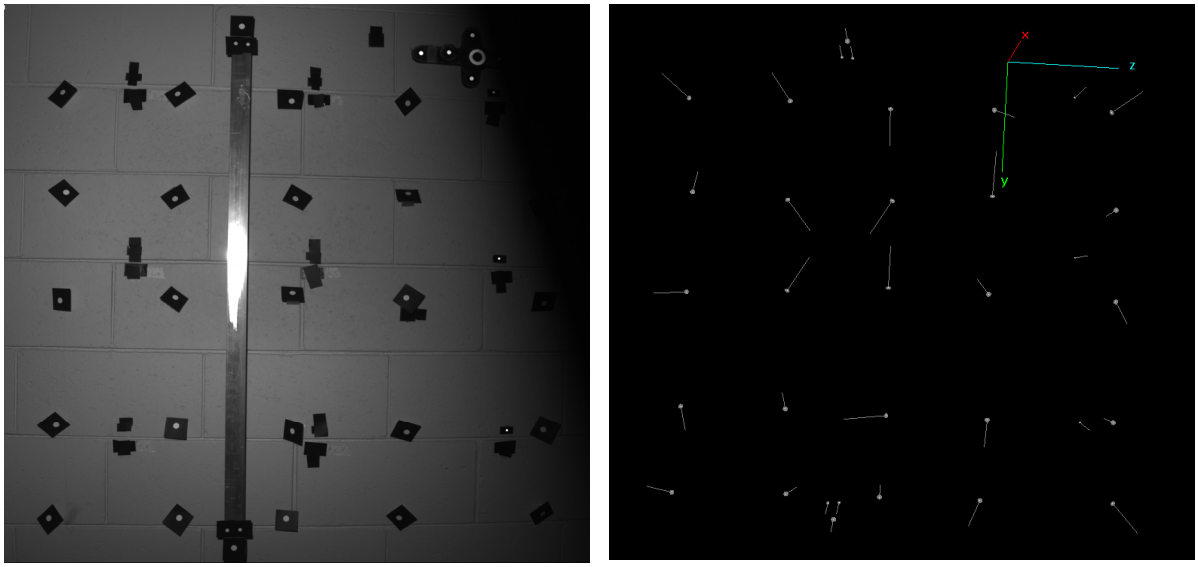

Figure 6.12: Test field for analysing the intensity characteristics of plane white targets

Consequently, only certain project images which showed a relatively homogenous illumination were selected for the analysis. The result of intensity analysis can be seen in Figure 6.13. The intensities were computed by a single normalisation process, identical to the retro-reflective target project. Although the data points show a clearly higher statistical spread than before, there is a very recognisable linear trend.

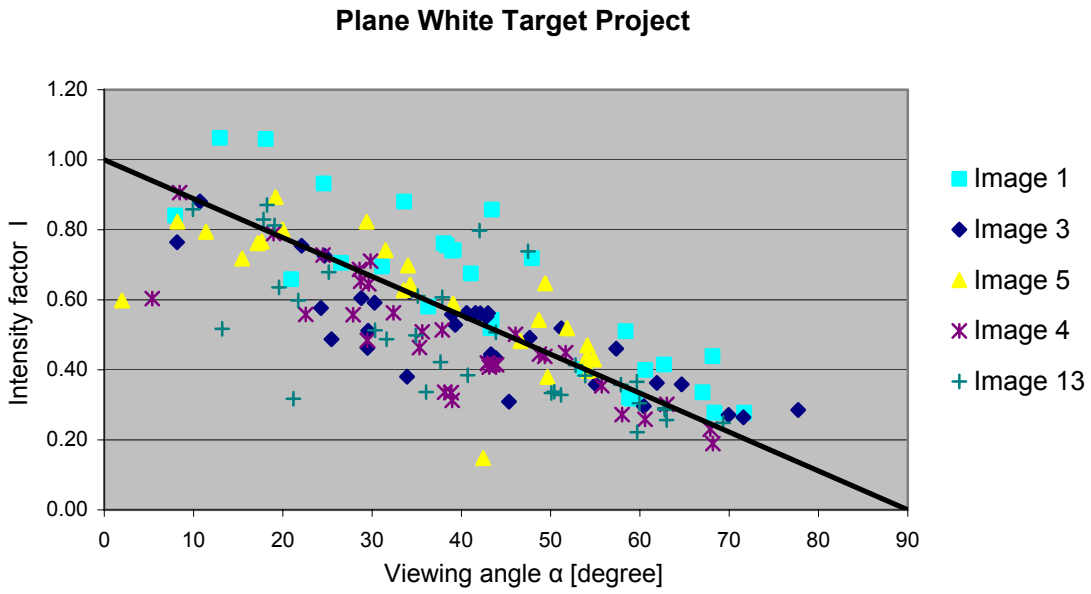

Figure 6.13: Intensity factor characteristics of plane white targets, including best-fit line

The intensity of the targets linearly decreases to zero at a viewing angle of 90 degrees. The intensity devolution of plane white targets can be approximated by

$$I_{\text{PlaneWhiteTarget}} \approx -\frac{1}{90}\alpha_{[\text{degree}]} + 1 \tag{6.9}$$

Theoretically, the intensity profile should follow the Lambert's cosine law, however, as indicated by Figure 6.13, only a linear trend was observed.

For completeness it should be mentioned that equations (6.8) and (6.9) are valid for on-axis illumination only. In summary, it is necessary to differentiate between the different target types for the distortion analysis of targets with curved surfaces.

6.1.2.3. Rasterising Algorithm

To generate virtual images for the analysis of curved targets, the imaged edge target has to be rasterised in a similar process to that described in Chapter 5.1. Whereas the ellipse covered pixel area was computed rigorously by integrating the ellipse equation, the sought-after areas for this investigation were computed by approximation. Since it is very complicated to derive a rigorous area equation, the edge curve was approximated by a dense poly line. As it turns out, the algorithm

to rasterise a polyline is much simpler than the one for the rigorous ellipse equation, as will now be outlined.

First the polyline which represents the continuous edge curve is computed to a certain precision. Then the polyline is intersected with all pixel boundaries and it is extended by the intersection points in the correct order, as indicated in Figure 6.14. During the pixel boundary intersection it is very efficient to build up a corner matrix (Figure 6.15) as described in Chapter 5.1. Additionally, a second matrix is generated which stores the index of intersection points. Since up to eight intersection points may appear, the indices have to be stored in a similar binary pattern as that used with the corner information. Using the polyline data along with the corner matrix and the index matrix, it is relatively straightforward to generate a sub-polyline representing the covered area for each pixel. Finally, using a standard algorithm the area of the sub-polyline is computed.

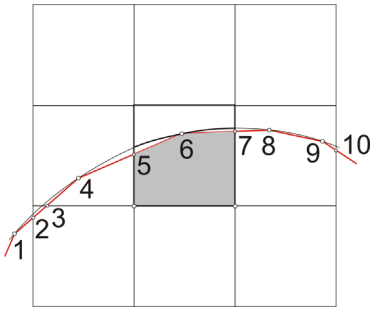

Figure 6.14: Approximation of edge curve

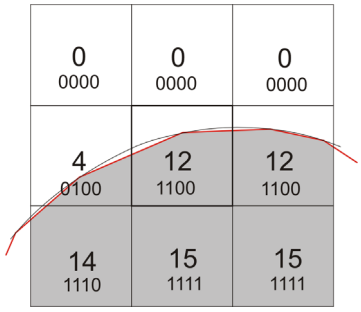

Figure 6.15: Corresponding corner matrix

Although the imaged edge is a high-order function, it is a convex curve assuming that occluded parts of the target edge are cut out and replaced by the target (i.e. cylinder) contour. This can appear in the case of high target curvature combined with oblique viewing directions. Consequently, it was considered within the Maple package, as indicated in Figure 6.16. The knowledge that the curve is convex simplifies the rasterizing algorithm at certain points.

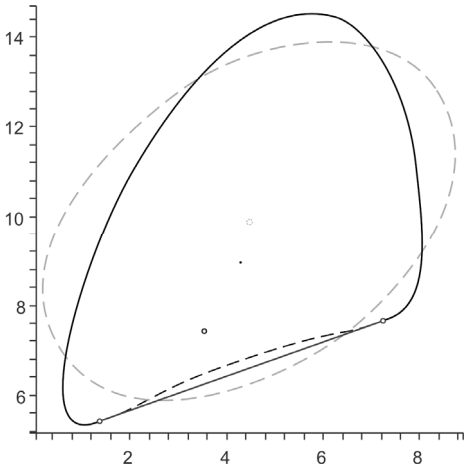

Figure 6.16: Replacing occluded parts of a target by its contour

The result of the rasterising is a matrix where each cell stores the area covered by the imaged target. In the next stage the intensity profile, as derived in the previous sections, is applied. Therefore, each cell area is simply multiplied by an average intensity. If rigorousness is considered, the average intensity has to be determined by integrating the intensity over the covered area. Since the intensity profile will be nearly linear across the pixel area considering small pixels the average intensity can be approximated by the intensity value of the centre of gravity of the covered area.

$$I_{average} = \frac{1}{A}\int_{A} I \cdot dA \approx I_{CenterOfA} \tag{6.10}$$

Hence, the grey value of a pixel can be computed by

$$gv = gv_{\max} \cdot I_{average} \cdot A + gv_{background} \approx 255 \cdot I_{CenterOfA} \cdot A \tag{6.11}$$

if maximum contrast without any background noise is desired.

Employing the described algorithm and the derived intensity profiles, the raster images of retro-reflective targets and plane white targets can be computed assuming a given network configuration. Whereas the intensity images of plane white targets (Figure 6.18) have a plane plateau at the target centre, retro-reflective targets (Figure 6.17) show a slightly curved plateau, as expected.

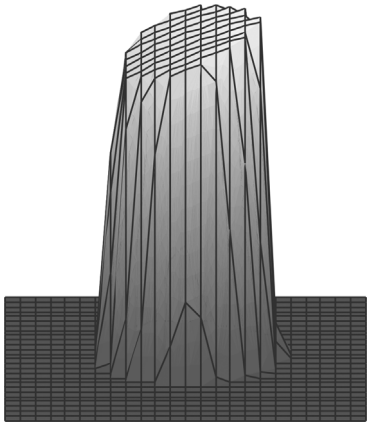

Figure 6.17: Intensity image of computed retro-reflective target

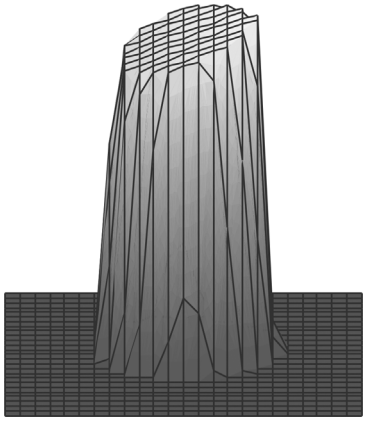

Figure 6.18: Intensity image of computed plane white target

6.1.2.4. Discrete Distortion Estimations

Theoretically it is possible to find a continuous distortion equation which also considers the derived intensity profile of the different targets. However, the formula is very complex and contains two-dimensional integrals which are only solvable numerically. Therefore it was decided to use the presented rasterising process to discretely estimate the distortional effect of bent targets. To compute the centroid shift which is only caused by the target curvature, the target was rasterised twice. The first centroid was computed by setting the cylinder radius to infinity. Then the process was repeated only changing the cylinder radius to the desired value. The difference vector of the

two centroids delivers the sough-after shift. As mentioned in Chapter 2.2.1, in high precision VM application centroiding accuracies of 2 to 5 percent of the pixel size can be achieved. Hence, the acceptable curvature error has to be clearly below the required centroiding precision. E.g. 1 percent of the pixel size.

Before results of the error estimation are presented, a curvature criteria is introduced. The curvature k of a cylindrical target can be described as "target radius-to-cylinder radius ratio" which also corresponds to a certain height of the circle segment h (see Figure 6.19).

$$k = \frac{r}{R}$$

$$h = x_{max} = R\left(1 - \cos\left(\frac{r\sin\beta}{R}\right)\right) = R\left(1 - \cos\frac{r}{R}\right) = R\left(1 - \cos k\right) \quad \Rightarrow \tag{6.12}$$

$$\frac{h}{r} = \frac{R}{r}\left(1 - \cos k\right) = \frac{1}{k}\left(1 - \cos k\right)$$

Since the absolute value of h is of minor interest, a relative term considering the target radius r is used. As derived above, the ratio h/r only depends on the curvature k. Some numerical examples of these variables can be seen in Table 6.1.

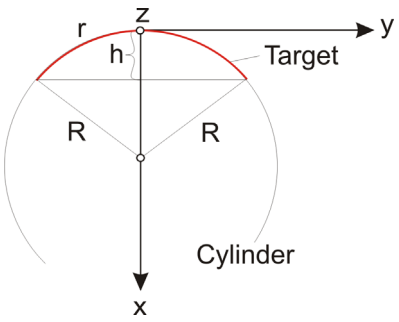

Figure 6.19: Relation between cylinder radius R, target radius r and height of the circle segment h

target radius r	cylinder radius R	k = r/R	h/r
10	50	0.2	10.0%
10	100	0.1	5.0%
10	200	0.05	2.5%
10	500	0.02	1.0%

Table 6.1: Numerical examples of target radius r, cylinder radius R and corresponding values for the curvature k and segment height h

The centre shift caused by the curvature depends on many parameters, for example the viewing angle, imaged target size, position of the imaged target within the image and the focal length of the camera. Additionally, the shift is strongly influenced by the angle between the viewing direction and the cylinder axis, as indicated in Figure 6.20. The two images were generated by projecting 12

identical (size and orientation) targets into the image. All targets were positioned equidistant to the project centre of the virtual camera, with a 20 mm lens. The image-targets configuration was kept identical between the left and the right image. The only difference is that the targets were rotated 90 degrees around their normal.

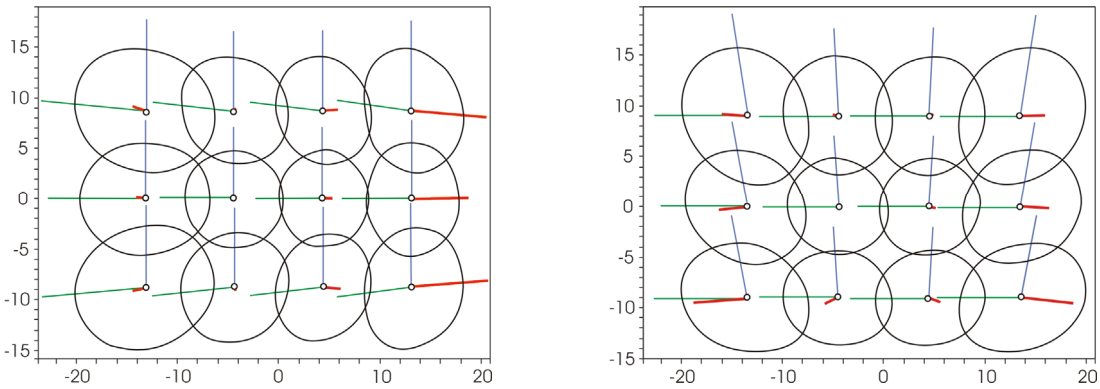

Figure 6.20: Distortion vectors (red) caused by target curvature (target radius = 10 mm, cylinder radius 100 mm) are inflated 1000 times. Target edge (black) is inflated 100 times. Image plane of left image is parallel to cylinder axis (blue lines). In the right image the targets were rotated around their normal by 90 degrees which caused the curvature direction of the target (green lines) to be parallel to the image plane

This computational example shows the complexity of the problem of selecting appropriate parameters for the quantitative description of the distortional shift. Since the aim of this analysis is to find a maximum acceptable curvature criteria rather than a rigorous correction formula, a pragmatic approach was chosen to analyse the problem. Using a typical network configuration and a certain cylinder radius, the distortion vectors were computed for all imaged targets within all images. Then, for each vector the viewing angle, the target radius within the images and the vector length were calculated. Considering these three parameters as three-dimensional coordinates, a point cloud can be generated, as indicated in Figure 6.21.

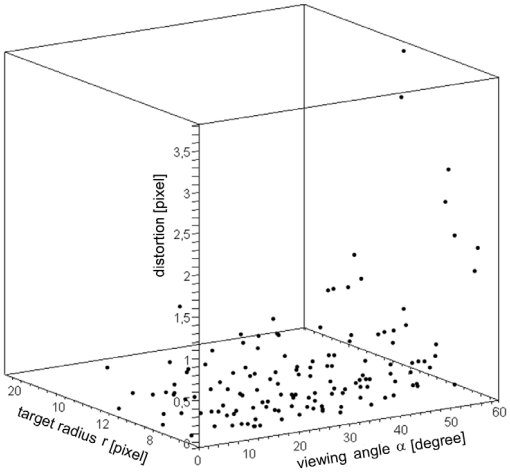

Figure 6.21: Distortion depending on target radius and viewing angle

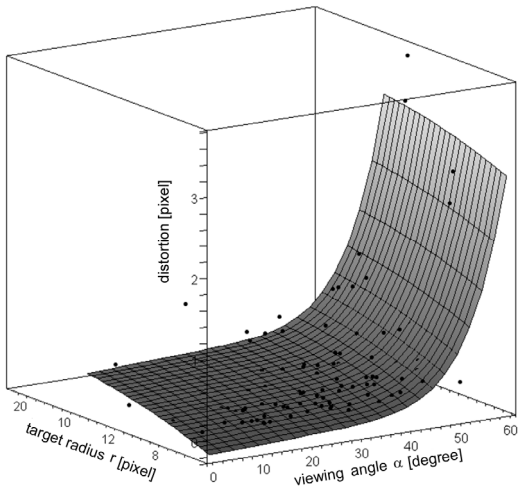

Figure 6.22: Point cloud and best-fit polynomial surface

Using a least-squares adjustment, a polynomial surface (see Appendix A4) can be fitted to the point cloud, where a polynomial of the following form turned out to be most appropriate:

$$z_{RRT}(\alpha, r) = a_0 + a_1 \cdot \alpha + a_2 \cdot r^2 + a_3 \cdot \alpha^8 \tag{6.13}$$

for retro-reflective targets and

$$z_{PWT}(\alpha, r) = a_0 + a_1 \cdot \alpha + a_2 \cdot r^2 + a_3 \cdot \alpha^2 \tag{F.14}$$

for plane white targets, where α is the angle between the target normal and the viewing direction, r is the target radius within the image and z is the length of the distortion vector. The adjusted equations are then used to asses the distortion by generating contour plots where certain error levels (unit pixels) are drawn, as indicated in Figure 6.23. In the following, various contour plots of different curvatures *k*, different target types and two different focal lengths are listed. Side by side figures are based on identical configurations but different target types. Left hand side plots are computed by using the retro-reflective target intensity profile, whereas figures on the right represent plane white targets. An interpretation of the results can be made from these figures.

In case of high precision VM applications, a maximum distortion error of 1 percent of the pixel size is acceptable. From this point of view the contour plots can be employed to identify a maximum acceptable curvature *k*, if a certain target radius within the image is given, or the other way around. As an example the following application is imagined: Using retro-reflective targets and a 20mm lens the curvature *k* may not exceed 0.05, if an average target radius of 4 pixel within the images is required (see Figure 6.27).

Whereas the viewing angle dependency is nearly negligible employing retro-reflective targets, the viewing angle must be considered if plane white targets are used. E.g. assuming plane white targets

and a curvature *k* of 0.05 the viewing angle must not exceed 20 degrees if centroiding errors up to 0.02 of the pixel size are accepted (compare Figure 6.36).

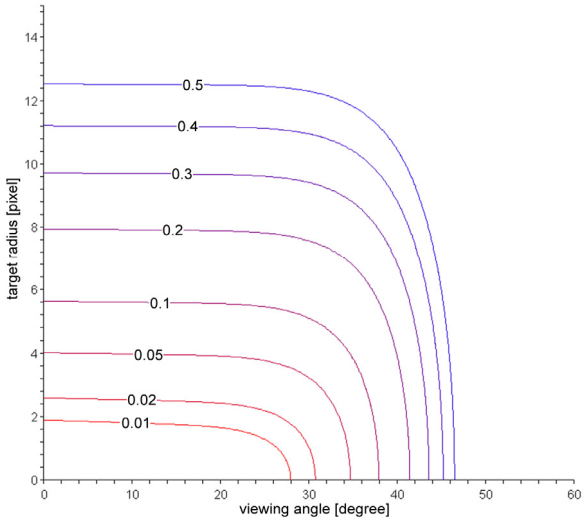

Figure 6.23:k = 0.2, c = 20 mm, retro-reflective targets

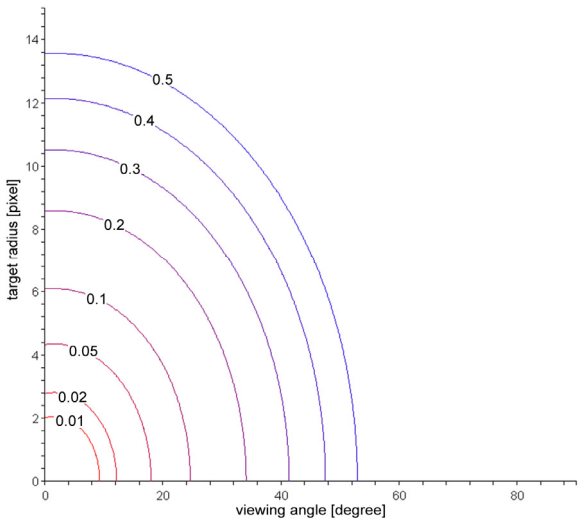

Figure 6.24:k = 0.2, c = 20 mm, plane white targets

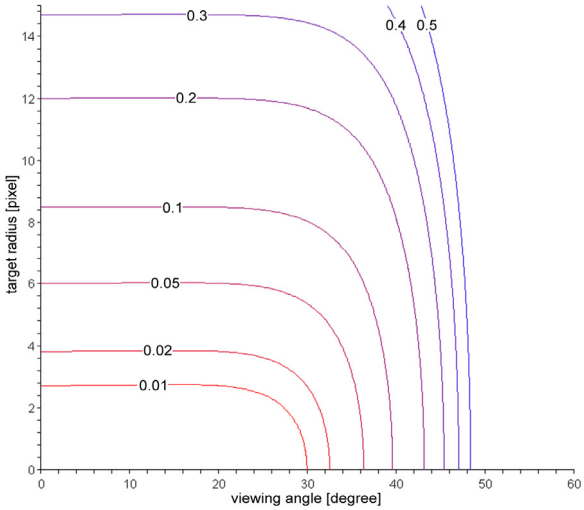

Figure 6.25:k = 0.1, c = 20 mm, retro-reflective targets

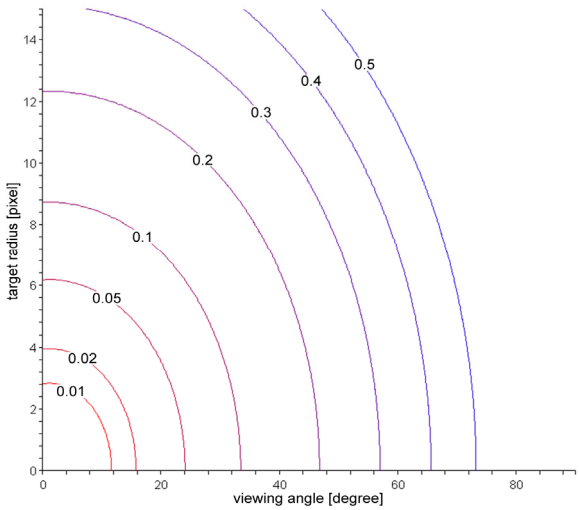

Figure 6.26:k = 0.1, c = 20 mm, plane white targets

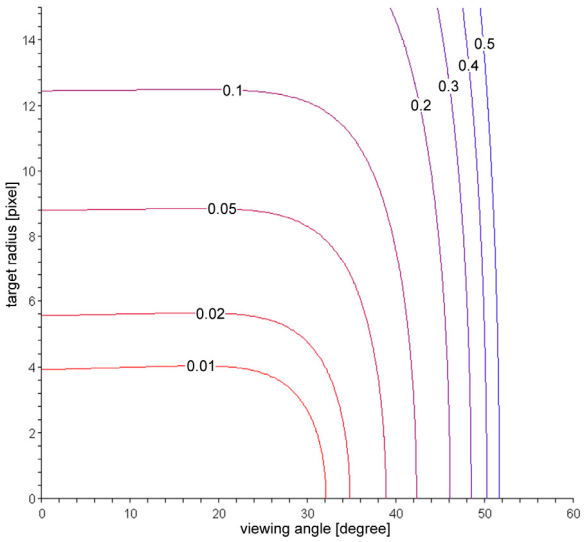

Figure 6.27:k = 0.05, c = 20 mm, retro-reflective targets

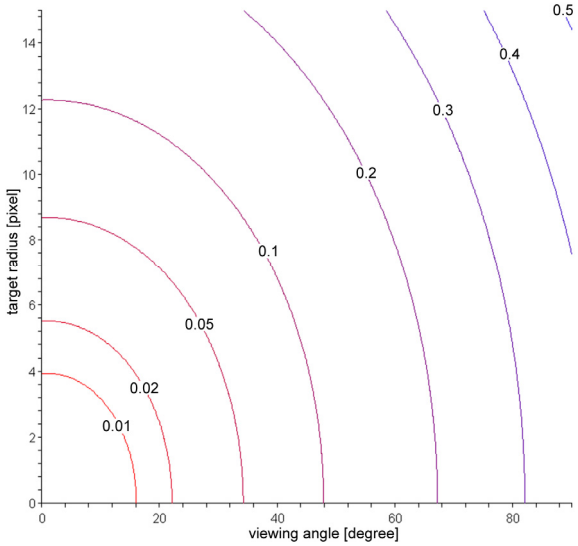

Figure 6.28:k = 0.05, c = 20 mm, plane white targets

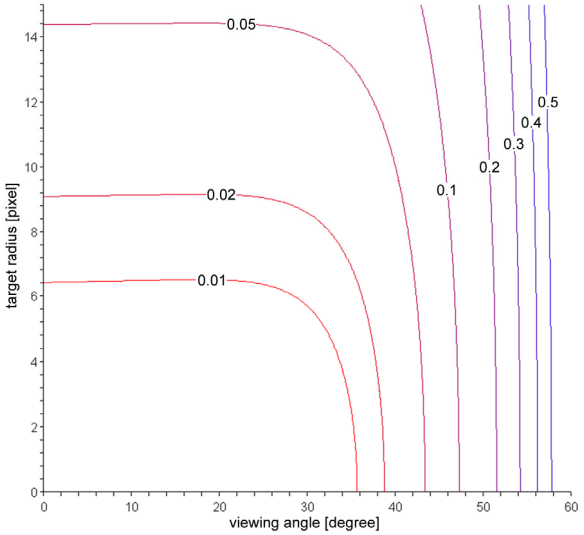

Figure 6.29:k = 0.02, c = 20 mm, retro- reflective targets

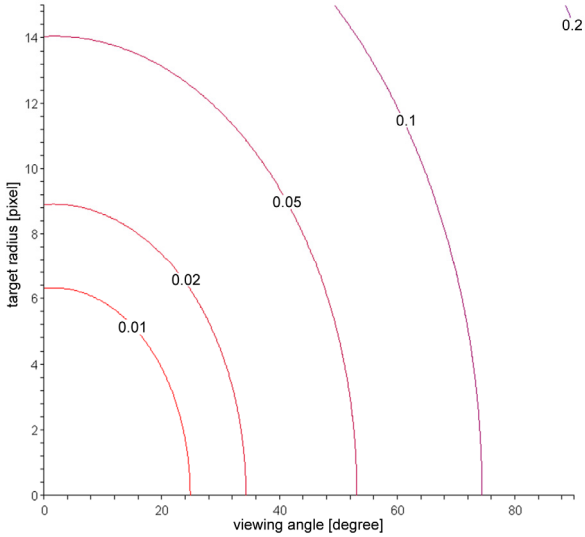

Figure 6.30:k = 0.02, c = 20 mm, plane white targets

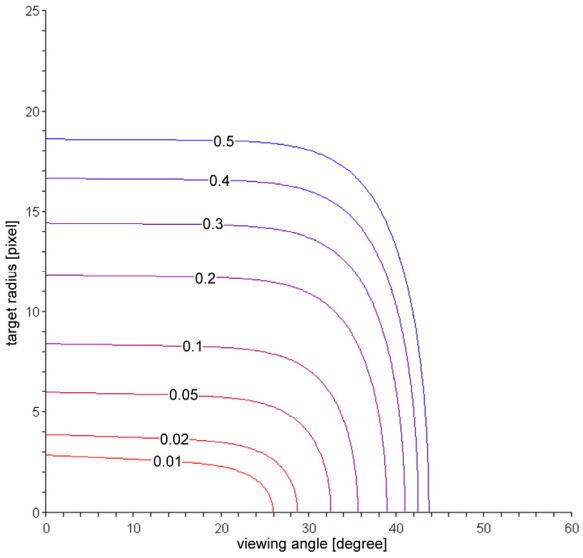

Figure 6.31:k = 0.2, c = 30 mm, retro-reflective targets

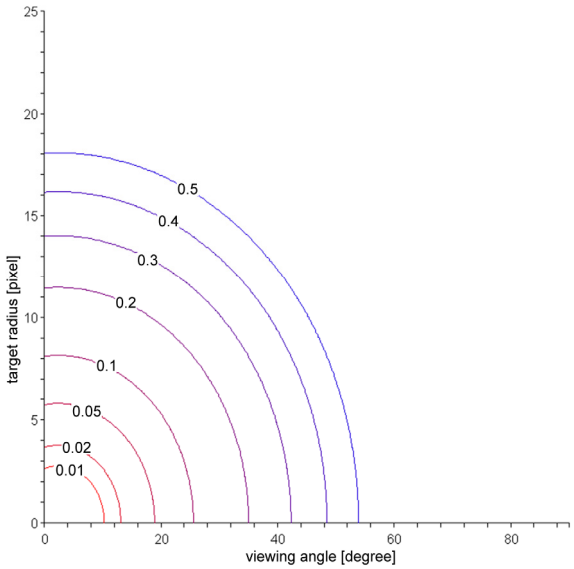

Figure 6.32:k = 0.2, c = 30 mm, plane white targets

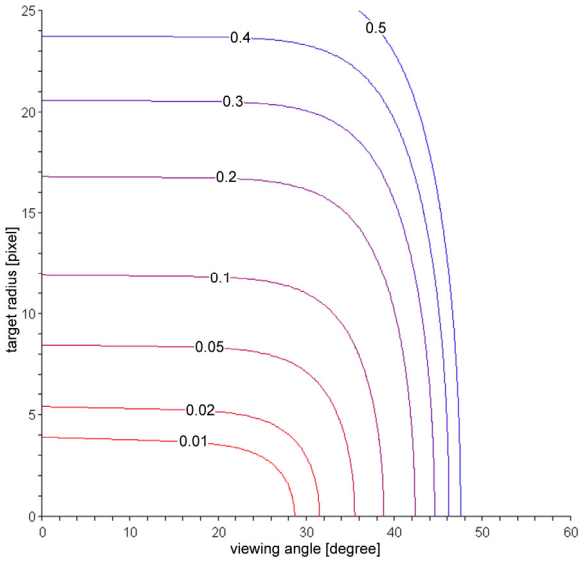

Figure 6.33:k = 0.1, c = 30 mm, retro-reflective targets

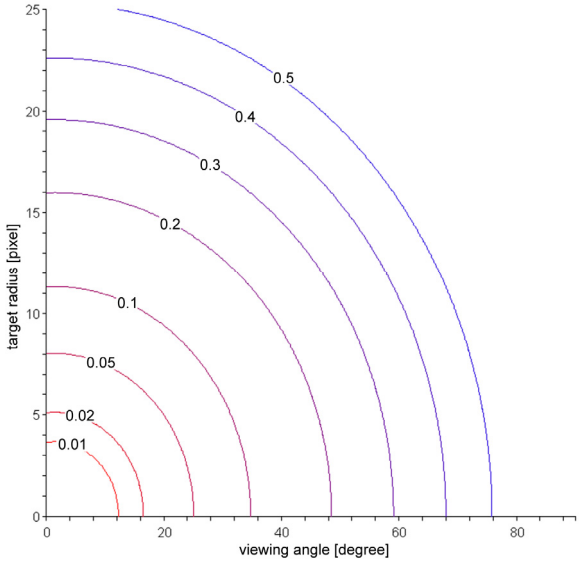

Figure 6.34:k = 0.1, c = 30 mm, plane white targets

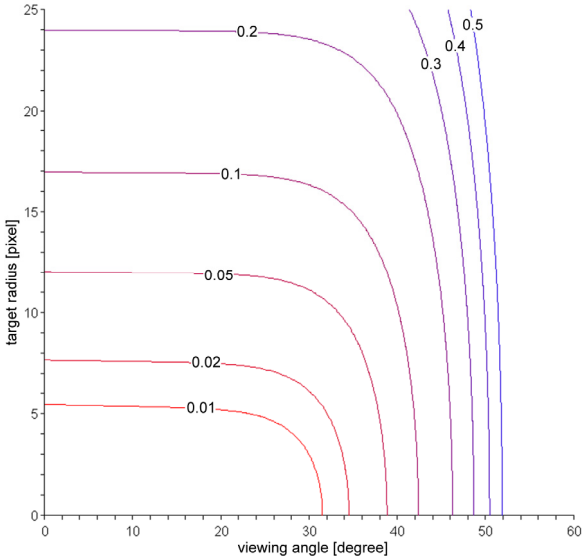

Figure 6.35:k = 0.05, c = 30 mm, retro-reflective targets

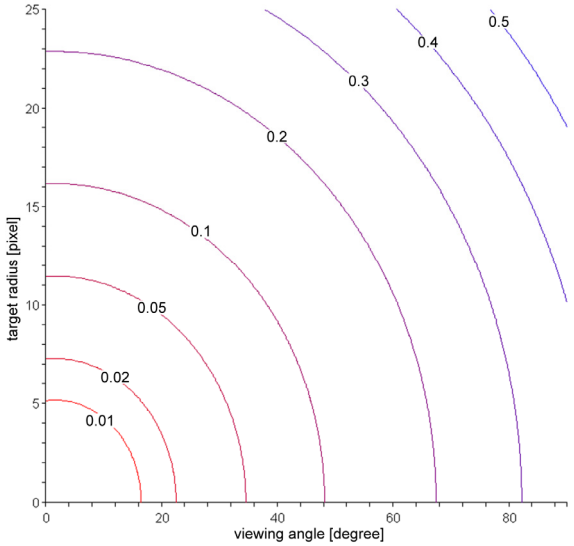

Figure 6.36:k = 0.05, c = 30 mm, plane white targets

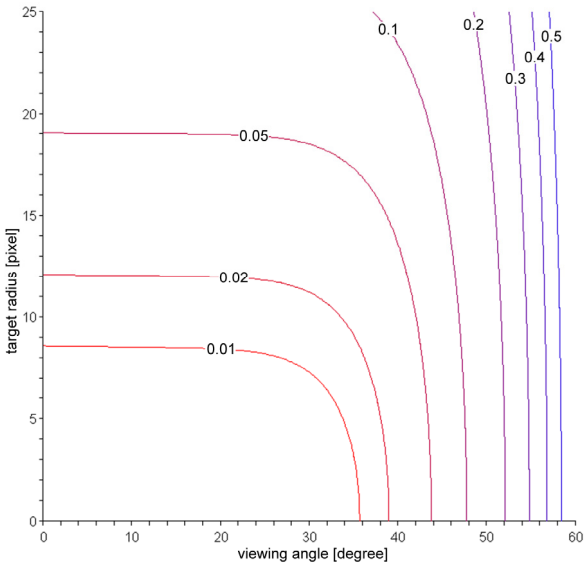

Figure 6.37:k = 0.02, c = 30 mm, retro-reflective targets

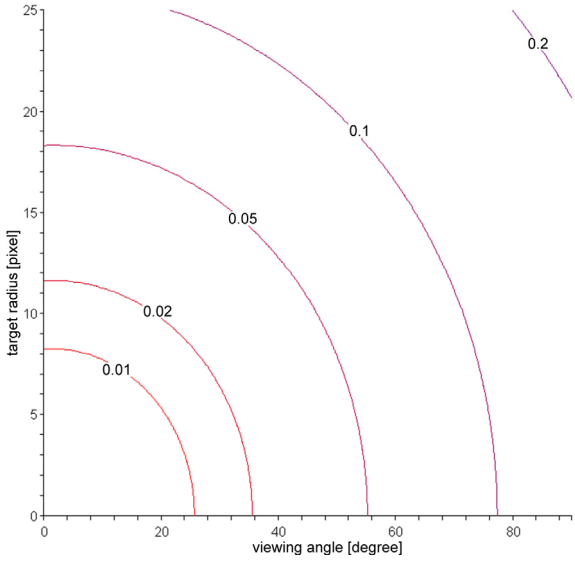

Figure 6.38:k = 0.02, c = 30 mm, plane white targets

After analysing the different contour plots, several conclusions can be drawn. First, there is a clear difference between retro-reflective and plane white targets which is evident considering the different intensity profiles. Second, there is no significant difference between 20 mm and 30 mm focal length regarding the intersection of contour lines with the viewing angle axis. However, for small viewing angles, identical target radii result in smaller distortion errors if higher focal lengths are employed. Third, the centroiding error caused by the target curvature is surprisingly high. This supports the knowledge that targets should be carefully glued, bubble-free and as flat as possible on to the surface if highest precision is to be achieved.

Finally, a tabular summary (Table 6.2) of the simulated distortion errors is given for retro-reflective targets. Listed results represent distortion errors at a viewing angle of zero. As mentioned, the viewing angle dependency is not relevant for practical applications and therefore not considered within this table. For plane white targets, a similar table can be generated. However, there the viewing angle must be considered. The corresponding tables are listed in Appendix B1.

	distortion error = 0.01 [pixel]		distortion error = 0.02 [pixel]		distortion error = 0.05 [pixel]	
	c = 20 mm	c = 30 mm	c = 20 mm	c = 30 mm	c = 20 mm	c = 30 mm
k = 0.2	1.9	2.8	2.6	3.9	4.0	6.0
k = 0.1	2.7	3.9	3.8	5.4	6.0	8.4
k = 0.05	3.9	5.5	5.6	7.6	8.8	12.0
k = 0.02	6.4	8.6	9.1	12.1	14.4	19.0

Table 6.2: Maximum target radii of imaged retro-reflective targets for certain configurations

This completes the discussion of the simulations performed for the thesis research. In the following, results gained from the target plane determination in real test fields are described.

7. Evaluation of Target Plane Determination

This chapter addresses practical aspects of the developed target plane determination process. The precision of the computed target planes will be reported. Initially, however, a short introduction to the photogrammetric software package *Australis* will be given, since all developed processes and algorithms were implemented and evaluated within this software system designed for VM.

7.1. Australis: An Ideal Evaluation Environment

Australis (*Photometrix* 2004) was originally developed at the Department of Geomatics, University of Melbourne, but it is now maintained and distributed *Photometrix Pty Ltd*. The software package is designed for off-line digital close-range photogrammetric image measurement, orientation, triangulation and sensor calibration. It is used to teach photogrammetric principles and practices and is a valuable tool for both research and practical measurement applications. At present there are more than 80 installations of Australis worldwide.

Australis uses images produced from digital cameras or digitally scanned imagery from film-based cameras. It is equally useful for high-precision metrology applications using 'metric' digital cameras (or scanned imagery) or low- to moderate-accuracy measurement employing off-the-shelf, amateur still video CCD cameras. The software offers manual, semiautomatic and fully automatic measurement techniques.

Since *Australis* provides all standard photogrammetric procedures, and a high degree of user interaction, it turned out to be an ideal tool to implement and evaluate the developed processes. The software is programmed in *Microsoft Visual C++*, which is why the new algorithms were also implemented in object-orientated code within the same language. Although a lot of research time was consumed by programming and evaluating the new algorithms, an attempt was made to focus on the theoretical and mathematical aspects of target mensuration. This explains why the users point of view of the new developments is presented, rather than a detailed account of the source code development. For completeness, it should be mentioned that all eccentricity simulations of Chapter 5 were also performed using *Australis*.

At the current state the target plane determination is performed as a post-processing stage to the normal photogrammetric orientation process. This gives the user the option to employ the corrective process only, if required. Additionally, a fully resolved network simplifies certain stages of the target plane determination.

7.1.1. Ellipse-Fitting Process in Australis

First, the ellipse information for each target is extracted for all images. This step does not require any triangulation information from the network. One could argue that the ellipse-fitting process should be automatically performed during the image scanning. This is basically correct, but disadvantages for such a practice would arise in this case. A scanning algorithm combined with intensity-weighted centroiding (see Chapter 2.2.1) is very efficient concerning computing time. With today's computers it takes minimal effort to successfully extract the observations of a high-contrast image in less than a second (Otepka, 2001). Additionally, the overall scanning time is, to a great extent, independent of the target size. The computing time is clearly higher, if the developed Gaussian distribution fitting is employed to determine the ellipse parameter. It should also be mentioned that the developed process usually takes between 3 and 4 iterations to converge. Additionally, the performance is also highly dependent upon the imaged size of the target, as indicated in Table 7.1. Each additional target pixel requires an additional observation within the adjustment and consequently increases the calculation time. To see the overall ellipse fitting time, consider the following test field case. If 50 object points are imaged from 10 camera stations, 500 ellipses must be fitted. Assuming an average computing time of 0.08 seconds per ellipse, 40 seconds can be required for the overall process. Considering that such a project is fully processed by the automated measurement methods within *Australis* in 20 seconds, it shows the relatively poor time performance of the developed Gaussian distribution fitting.

Average target radius [pixel]	Average Gaussian distribution fitting time per target [s]
2.3	0.08
4.0	0.18

Table 7.1: Average computing time on a *Pentium 4 Mobil Processor* with 1.8 GHz for different target radii, determined in typical VM projects

As described in Chapter 4.2, the Gaussian distribution fitting delivers the most accurate ellipse information compared to other algorithms. However, it was also mentioned that in the case of bigger target (imaged target radius > 7 pixels), the best-fit ellipse algorithm of intensity levelled points computes equally accurate results. Since this algorithm needs only a fraction of the computing time of the Gaussian distribution fitting, performance improvements in the overall process are possible by using the accurate algorithm for small targets and the fast algorithm for bigger targets. No such optimisation had been implemented in *Australis* up until this research, because this is of minor interest from a purely scientific point of view.

In the following some additional details about the ellipse fitting process are presented. Based on the given centroid coordinates of a target, it is easy to extract the target pixel region from the image. Then, a algorithm grows the region to secure all edge pixels, and a background noise boundary is added. Finally, the Gaussian distribution fitting makes use of all pixels of the grown region to determine the sought-after ellipse parameter.

While the ellipse fitting process can take several minutes to execute, it is necessary to inform the user about the current computational status, as indicated in Figure 7.1. The best way to do so within C++ is to run the ellipse algorithm as an independent thread which communicates with the application via a status object (Otepka, 2001). This allows addition of termination mechanisms and they have been implemented within *Australis*.

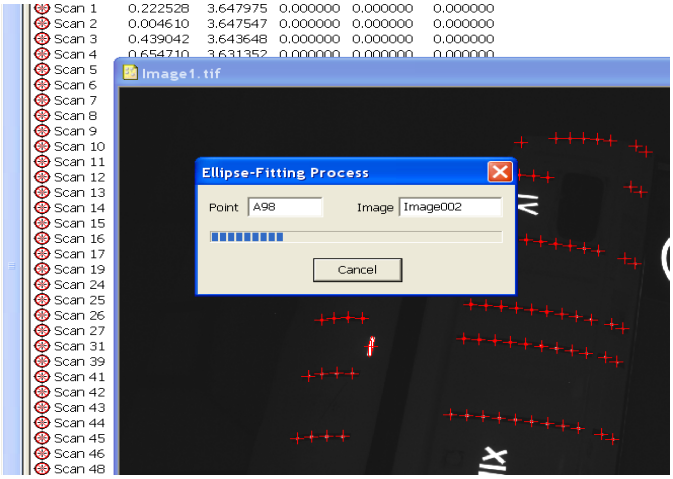

Figure 7.1: Status bar of ellipse-fitting process within *Australis*

7.1.2. Target Plane Determination in Australis

Once all ellipses are determined, the actual target plane determination can be performed. Assuming that the imagery of surveying project is fully measured, the required exterior orientations of all camera stations can be given. Then, the target plane is estimated point-wise using the adjustment as described in Chapter 4.3.2. Considering mathematical rigorousness, the process must be performed during the bundle adjustment because it affects the object point coordinates which, again, affects the exterior orientation within the bundle. However, practical tests have shown that the influence of the changed exterior orientation on the final target plane estimates is negligible. Hence, the following solution was pursued within *Australis*. First, a standard bundle adjustment is computed. Then, the target plane determination is performed. Finally, another bundle adjustment is performed using the eccentricity corrected observations. To compute an eccentricity correction, the real target centre and the target circle (equations (3.23) and (3.24)) are projected into the image. The difference between the imaged target centre and the imaged ellipse centre is used as a correction vector (the used ellipse centre is computed by converting the implicit ellipse parameter into parametric form via equation (A.3)).

Before discussing the performance of the target plane determination, first consider Table 7.2. As can be seen the computing time increases with an increasing number of images. Considering a VM project with 50 targets and 14 camera stations, the target plane determination is performed within 9 seconds. Hence, this process is not as expensive in computing time as the ellipse fitting stage.

	Camera stations	Computing time per target [s]
Project 1	6	0.06
Project 2	14	0.18
Project 3	36	0.43

Table 7.2: Average computing time of the target plane determination on a *Pentium 4 Mobil Processor* with 1.8 GHz for different VM projects

The implementation of the target plane determination is solved in a similar way to the ellipse-fitting process within *Australis* (see Figure 7.2). The program again presents a status dialog with the option to cancel the computation.

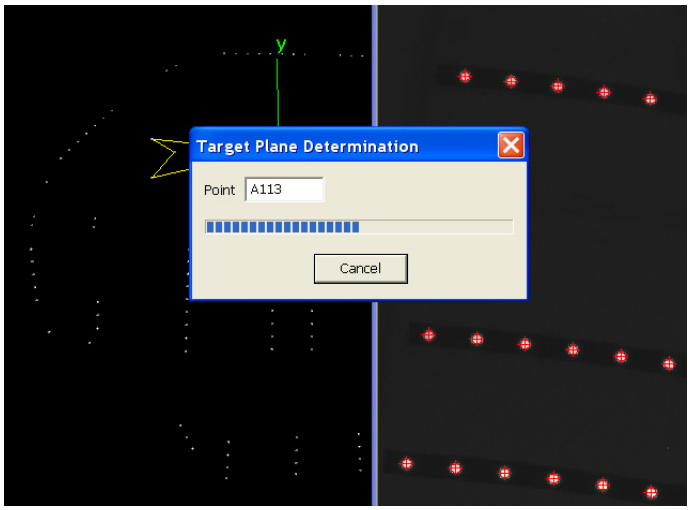

Figure 7.2: Status bar of the target plane determination within *Australis*

This concludes the description of the implementation of the overall target plane determination process within *Australis*. In the following section, the achievable accuracy of the developed process within real VM projects will be presented.

7.2. Accuracy of the Target Plane Determination within Real Applications

For the analysis of real imagery, objects with exact known surfaces were surveyed. The first test field comprised on a calibration table which had a machine-levelled surface. The table was kindly

made available by *Boeing Australia Limited* at a factory in Melbourne. Secondly a cylinder was surveyed to analyse the influence of the curvature on the plane determination process.

7.2.1. Test Project 1: Calibration Table

The degree of flatness which was required for the first test field was relatively low. As derived from the simulated surveys, if the surface normal varies less than 0.05 degrees, then its accuracy is well below the measurement precision of the plane determination process. An angle error of 0.05 degree at a 2 m test field is equal to a 0.9 mm sag in the middle of a planar test field . The table employed was at least a factor of 0.1 better than this. This was verified by a best-fit plane adjustment to the 3D coordinates of the test field: The RMS of the out-of-plane residuals was 0.02 mm.

The targets of the test field were arranged in a 4 by 4 grid, and four 4 different target sizes were used (3, 5, 6.35 and 9.39 mm). Thus, the test field consisted of the 64 inspection targets and some additional system-required targets.

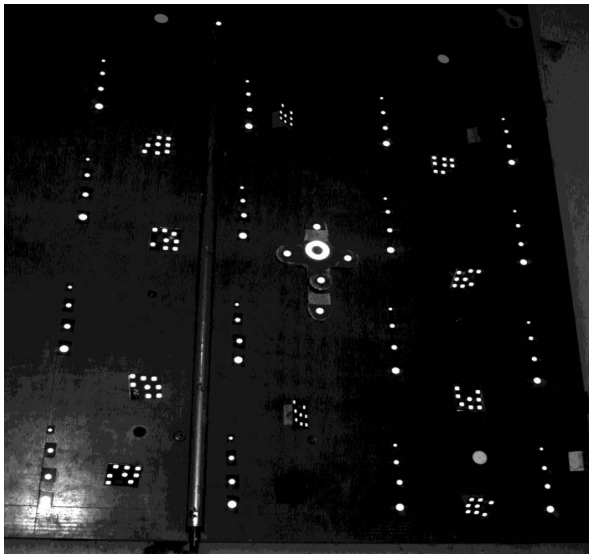

Figure 7.3: Calibration table at *Boeing*

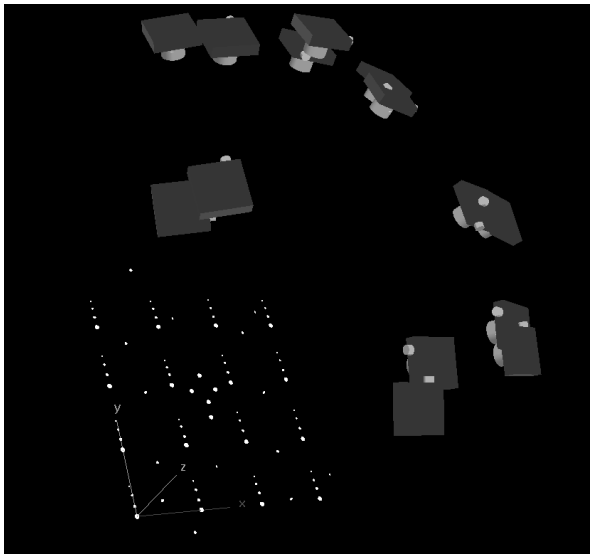

Figure 7.4: Position of the 14 camera stations

The results of the computation are listed in Table 7.3. As expected, the bigger the target size the more accurately the target normal can be determined. Whereas the results of the first three target classes are considered satisfactory, the target normals of the smallest targets are undoubtedly not as good. These targets contain only very limited elliptical information (Figure 7.5), but it is nevertheless quite impressive how accurately the target normals can still be determined.

Average Target Diameter [pixel]	Average Angle Error [degree]	Standard Error of Angle Error [degree]
13.2	0.43	0.25
8.6	0.57	0.27
7.1	1.09	0.48
4.2	3.06	1.20

Table 7.3: Target normal angle error of the different sized targets

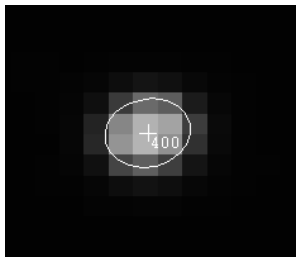

Figure 7.5: Target image of the smallest target group including the determined best-fit ellipse

7.2.2. Test Project 2: Cylindrical Hull

Whereas the first test field was designed to investigate the correspondence between target size and accuracy of the target normal, the cylindrical hull project was used to analyse the influence of surface curvature on the plane determination process.

Figure 7.6: An old theodolite 'bomb' as cylindrical survey object

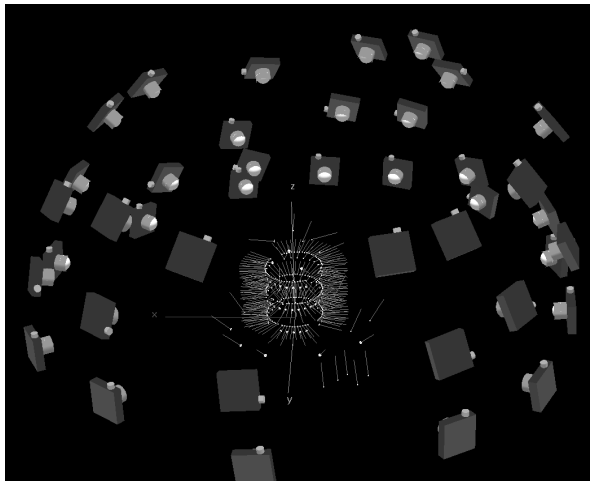

Figure 7.7: Final 3D view including target normals and all 40 camera stations

For this project only two different target sizes were used (3 and 6.35 mm). As before, the quality of how well the surface fits to a cylinder was checked as satisfactory. The results of the plane determination process are listed in Table 7.4.

Average Target Diameter [pixel]	Average Angle Error [degree]	Standard Error of Angle Error [degree]
10.0	1.16	0.61
5.9	2.33	1.59

Table 7.4: Accuracies of the target normal

As it can be seen in the table, the small targets deliver an accuracy of the target normal which corresponds to the results obtained in the first survey. However, the bigger targets with an average target diameter of 10 pixels result in less accurate target normals as expected. An average angle error of about 0.5 degrees would fit to the results from the planar test field project. This reduced

accuracy can only be based on the curvature being ignored within the target plane determination. In the following, the results corresponding to the error estimations made in Chapter 6.1.2.4 are analysed.

The cylinder project was surveyed with a *GSI INCA* camera using a 20 mm lens and the bundle adjustment delivered an rms of the adjusted observations of 0.21 µm (= 2.2 % of pixel size). The cylinder radius of the theodolite 'bomb' was computed to be about 109 mm. The radii of the retro-reflective targets were 1.5 mm and 2.5 mm. Hence, the curvature *k* amounted to 0.01 for the small, and 0.02 for the big targets. This means that Figure 6.29 is indicating the corresponding curvature errors for the 2.5 mm targets. As can be seen, a target radius of 5 pixels will displace the centroid by less than 1 % of a pixel. Hence, the object point accuracy should not be seriously effected by the curvature. Analysis of the bundle adjustment results shows that the object point rms is identical for both small and big retro-reflective targets, although the bigger targets are nearly twice as large as the small ones. This leads to the conclusion that the 1 % curvature error determines an actual limit which should not be exceeded if high precision VM measurement is to be achieved. However, it seems that the target plane determination is effected more by the curvature than the actual triangulation process. An analysis of the effect should form a part of future research.

7.3. Accuracy Gain by Considering the Eccentricity Effect

One aim of the research was to show that the accuracy of the bundle adjustment can be improved by correcting the observations for the eccentricity error. As simulations have shown (see Chapter 5), it was expected that only high-precision applications with large target orientation variation in conjunction with medium-sized targets will benefit from the developed process. Applying this knowledge, a specific test field was generated, similar to the rough table test field presented in Chapter 5.6. To determine if the corrected observations result in higher accuracies, a scale bar (see Figure 7.8) was surveyed in two different positions within the test filed. After performing the bundle adjustment the distance differences between the two virtual scale bars was calculated and compared.

Figure 7.8: Photogrammetrist at work surveying a test field with a high variation in target orientation

Figure 7.9: Aluminium corners were used to achieve the required target plane variation

First, the test field was surveyed employing retro-reflective targets. Then, the measurement process was repeated using plane white targets. Unfortunately, only small targets were available. The retro-reflective target size of r = 4.7 mm resulted in an average target radius of 5.1 pixels within the images. The plane white targets had a radius of 6.5 mm which imaged to an average radius of 7.4 pixels. As the simulation results in Table 5.18 show, the imaged target radius has to be bigger than 8 pixels for the error, caused by eccentricity to exceed the triangulation accuracy of 1:100 000. Consequently, the distortion was expected to be at the edge of the measurement precision for plane white targets, and below for retro-reflective targets. It turned out that there was no significant change in the computed length of the scale bars, irrespective of whether the bundle adjustment was computed by employing or not employing the eccentricity corrections. However, there was a significant distance difference of approximately 30 µm between the horizontal and vertical scale bar. Whether this was caused by a physical deformation of the scale bar or for some other reason could not be determined at the time.

Because there was no direct way to prove the accuracy gain by correcting for eccentricity, an indirect method, based on the simulations of Chapter 5, was employed to demonstrate the improvement. Therefore a transformation was computed where the object points from a bundle adjustment without the eccentricity corrections were transformed onto the object points from a bundle adjustment which included the eccentricity corrections. The procedure was repeated using the image simulator and the exact same network configuration. Then, the discrepancies of the two transformations were overlaid. As indicated in Figures 7.10 and 7.11, the discrepancies of the real data are visualised in white colour. The corresponding vectors of the simulation are drawn in grey. As can be seen, there is a very good correspondence between the two sets of distortion vectors. This leads to the conclusion that there is a real accuracy gain if the correction is employed. Additionally, it should be mentioned that object point accuracies of the plane white targets obtained from bundle adjustments (corrected and uncorrected) are within the same range as indicated by the

discrepancies in Figures 7.10 and 7.11. Hence, the bundle adjustment estimates of the object point accuracy will be too optimistic if the observations are not corrected for the eccentricity.

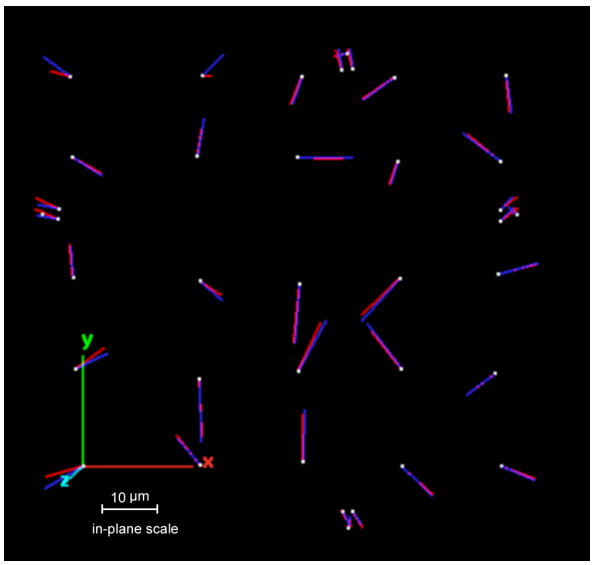

Figure 7.10: Real (red) and simulated (blue) eccentricity error vectors in the case of plane white target.

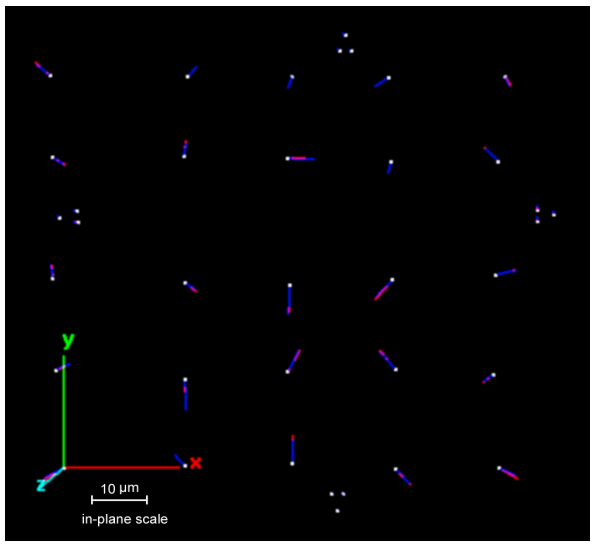

Figure 7.11: Real (red) and simulated (blue) eccentricity error vectors in the case of retro-reflective targets

Unfortunately, there were no resources available to repeat the survey with bigger targets, which should have shown the eccentricity effects more clearly. However, it was indirectly proved that the triangulation accuracy can be increased by correcting the observations for the eccentricity. For completeness, it should be mentioned that in the case of the retro-reflective targets only, the centre eccentricity was corrected, but not the retro-reflective edge shift (see Chapter 3.2) since it had no significant influence on the results. To further analyse the effectiveness of this correction formula, additional test fields are required.

8. Conclusions

The thesis has dealt with the fact that the centre of circular targets do not project onto the centre of their image in a central projection. Although this eccentricity is well-known, it is universally ignored in today's Vision Metrology system. A mathematical formula has been derived which describes the relationship between the circle in object space and the projected conic section in image space. Furthermore, a set of equations were derived which facilitate the extraction of the ellipse information with high precision from digital imagery. This made it possible to develop a target plane determination process which was implemented and evaluated within the photogrammetric software package *Australis*. It turned out that the target plane can be estimated with high accuracy if medium to large-sized targets are employed.
The derived formulas delivered, as a by-product, an equation to correct the image observations for the eccentricity error, which was also added to the bundle adjustment process in *Australis*. This more rigorous observation model should finally lead to higher accuracies in the VM triangulation process.

To estimate the distortional effect of the eccentricity several simulated networks were computed. The quantity of the distortion was shown to depend on the target size and the network configuration. However, it was realised that this effect is also highly influenced by the degree of variation of the target orientation.

Since the eccentricity can be corrected by the described process, any target radius limitations caused by the eccentricity can be discarded. However, there is one radius limitation remaining which is based on the surface curvature. In many VM applications, circular targets are directly glued onto the surveying object which causes curved targets. To estimate acceptable target curvatures, a module within the mathematical software *Maple* was developed. Because the results are greatly influenced by the reflection property of the target material, the computations were performed separately for retro-reflective and plane white target. By employing the developed module, various error graphs were generated which facilitated selection of the maximum acceptable target radius for a certain curvature. Summarizing it can be said that small target curvatures can cause relatively high centroiding errors.

Two ways in which VM projects should benefit from the thesis outcomes will now be described.

8.1. Benefits for Practical Applications

As already mentioned, in high accuracy application domains it should be possible to achieve even better object point accuracy via the improved observation model. To date, one has always had to find a compromise between big (high centroiding accuracy) and small targets (small eccentricity

error). The proposed method resolves this problem and allows the use of larger targets without the impact of eccentricity error. As mentioned, a target radius limitation will apply, this being based on target curvature only.

On the other hand, even medium accuracy applications can benefit in the case of surface inspections where targets are placed onto the surface of interest. The computed 3D coordinates of the object points are always positioned above the sought-after surface. This eccentricity is equal to the target thickness. So far, the computation of surface points needed additional information about the object surface shape or at least a degree of user interaction to define an adequate mathematical surface description.

Employing the target normal, the corresponding point on the surface can be directly computed. For an estimation of how accurate the target normal needs to be known, following considerations were made:

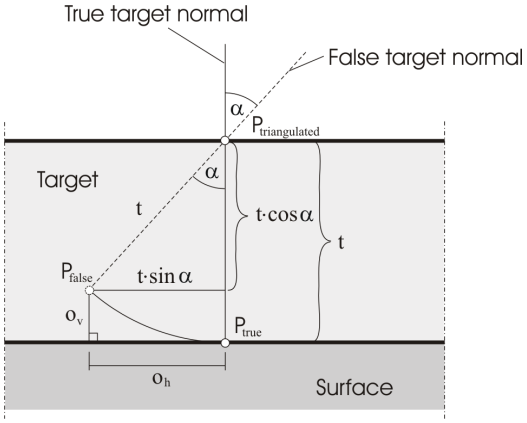

Figure 8.1: False surface point in the case of an incorrect target normal

As shown in Figure 8.1 a false target normal can lead to an incorrect surface point P_{false}. Assuming the target thickness t, the horizontal offset o_h and the vertical offset o_v can be described by

$$\begin{aligned} o_v &= t - t \cdot \cos\alpha = t \cdot (1 - \cos\alpha) \\ o_h &= t \cdot \sin\alpha \end{aligned} \tag{8.1}$$

Using a typical target thickness of 0.11 mm, Table 8.1 was generated. As can be seen, an angle error of 5 degrees results in a horizontal offset of only 10 µm.

α [degree]	o_v [mm]	o_h [mm]
1	0.000	0.002
5	0.000	0.010
10	0.002	0.019
25	0.010	0.046
65	0.064	0.100

Table 8.1: Various angle errors and their corresponding offsets

The object point accuracy of 10 µm is nowadays pretty much the measurement limit within VM. Thus, even in high precision surveys the target normal does not have to be known more accurately than 5 degrees (using targets with about 0.1 mm thickness). Additionally, it should be mentioned, that only the vertical offset is critical for most surface inspections. In these cases, the target normal can be much more distorted.
As the derivations above and the result from the test projects in Chapter 7.2 show, the computation of surface points by the presented process is applicable for VM projects of any accuracy level.

8.2. Future Research Aims

So far the author was not able to directly show an accuracy gain in real test fields by correcting the eccentricity. Although the strategy of scale bar comparisons (see Chapter 7.3) should allow a verification of the improved accuracy, a different method is also suggested to prove this. As the simulations have shown, it is not possible to recognise the distortional effect of the eccentricity only by analysing the bundle adjustment results. The errors are mostly compensated by adjustment parameters and therefore not 'visible'. Nevertheless, the full amount of the distortion effect can be determined if ultra-precise reference (checkpoint) coordinates of object points are given.

In Chapter 3.2 the retro-reflective edge shift was derived. All considerations there were based on the report by Zumbrunn (1995). However, the significance of such a shift could not be observed so far, since this distortion is covered by the centre eccentricity above a certain target size. Future research should investigate especially small networks (< 50 cm) where the retro-reflective edge shift is much more relevant.

In Chapter 6 the distortional effect of curved targets on the computed centroid was estimated. This allowed high measurement precision to be achieved in applications where curved targets are employed. The target plane determination is also effected by an incorrect centroid. However, there are several other parameters which distort the result of the determination process. Consequently, it would be interesting to derive some rules which secure a certain target plane accuracy, similar to what was carried out in the centroid process.

Appendix A1: Conversion of Ellipse Parameters

An ellipse can be described in implicit form as a general polynomial of second degree

$$a_1 \cdot x^2 + a_2 \cdot xy + a_3 \cdot y^2 + a_4 \cdot x + a_5 \cdot y - 1 = 0 \tag{A.1}$$

or in parametric from as

$$\begin{pmatrix} x \\ y \end{pmatrix} = \begin{pmatrix} M_x \\ M_y \end{pmatrix} + \begin{pmatrix} \cos\theta & \sin\theta \\ -\sin\theta & \cos\theta \end{pmatrix} \begin{pmatrix} A\cos\alpha \\ B\cos\alpha \end{pmatrix} \tag{A.2}$$

where M_x, M_y are the centre coordinates, θ is the bearing of the semi-major axis, A and B are the semi major and semi minor axes of the ellipse.

By the following equations the implicit parameters can be converted to ellipse parameters:

$$\begin{aligned} M_x &= \frac{a_2 \cdot a_5 - 2 \cdot a_3 \cdot a_4}{4 \cdot a_1 \cdot a_3 - a_2^{\,2}} \\ M_x &= \frac{a_2 \cdot a_4 - 2 \cdot a_1 \cdot a_5}{4 \cdot a_1 \cdot a_3 - a_2^{\,2}} \\ \theta &= -\frac{1}{2}\arctan\frac{a_2}{a_1 - a_3} \end{aligned} \tag{A.3}$$

$$\begin{aligned} A &= \sqrt{\frac{1 - \frac{a_4}{2} M_x - \frac{a_5}{2} M_y}{a_1 \cdot \cos^2\theta - a_2 \cdot \sin\theta \cdot \cos\theta + a_3 \cdot \sin^2\theta}} \\ B &= \sqrt{\frac{1 - \frac{a_4}{2} M_x - \frac{a_5}{2} M_y}{a_3 \cdot \cos^2\theta + a_2 \cdot \sin\theta \cdot \cos\theta + a_1 \cdot \sin^2\theta}} \end{aligned} \tag{A.4}$$

The reverse conversion can be performed by

$$\begin{aligned} \overline{a_1} &= \frac{\cos^2\theta}{A^2} + \frac{\sin^2\theta}{B^2} \\ \overline{a_2} &= 2 \cdot \cos\theta \cdot \sin\theta \cdot \left(\frac{1}{B^2} - \frac{1}{A^2} \right) \\ \overline{a_3} &= \frac{\sin^2\theta}{A^2} + \frac{\cos^2\theta}{B^2} \\ d &= 1 - M_x^{\,2} \cdot \overline{a_1} - M_x \cdot M_y \cdot \overline{a_2} - M_y^{\,2} \cdot \overline{a_3} \end{aligned} \tag{A.5}$$

$$\begin{aligned} a_1 &= \frac{\overline{a_1}}{d} \qquad a_4 = -\frac{2 \cdot M_x \cdot \overline{a_1} + M_y \cdot \overline{a_2}}{d} \\ a_2 &= \frac{\overline{a_2}}{d} \qquad a_5 = -\frac{2 \cdot M_y \cdot \overline{a_3} + M_x \cdot \overline{a_2}}{d} \\ a_3 &= \frac{\overline{a_3}}{d} \end{aligned} \tag{A.6}$$

Appendix A2: Conversion of Variance-Covariance Matrices of Different Ellipse Parameters

Using equations (A.3) to (A.6) and the error propagation principle (see equation (4.13)) a variance-covariance matrix Σ_I of the implicit parameters can be transformed into the corresponding variance-covariance matrix Σ_E of the ellipse parameters and vice versa. First, the linearised equations are needed, as listed below (**J**(**x**, **y**) is called the Jacobian matrix of **x** with respect to **y**):

$$\mathbf{F}_{\mathbf{I}\to\mathbf{E}} = \mathbf{J}\left(\begin{pmatrix} a_1 & a_2 & a_3 & a_4 & a_5 \end{pmatrix}^T, \begin{pmatrix} M_x & M_y & \phi & A & B \end{pmatrix}^T\right) = \begin{pmatrix} \frac{\partial a_1}{\partial M_x} & \frac{\partial a_1}{\partial M_y} & \frac{\partial a_1}{\partial \phi} & \frac{\partial a_1}{\partial A} & \frac{\partial a_1}{\partial B} \\ \frac{\partial a_2}{\partial M_x} & \frac{\partial a_2}{\partial M_y} & \frac{\partial a_2}{\partial \phi} & \frac{\partial a_2}{\partial A} & \frac{\partial a_2}{\partial B} \\ & & \vdots & & \\ \frac{\partial a_5}{\partial M_x} & \frac{\partial a_5}{\partial M_y} & \frac{\partial a_5}{\partial \phi} & \frac{\partial a_5}{\partial A} & \frac{\partial a_5}{\partial B} \end{pmatrix} \tag{A.7}$$

$$\mathbf{F}_{\mathbf{E}\to\mathbf{I}} = \mathbf{J}\left(\begin{pmatrix} M_x & M_y & \phi & A & B \end{pmatrix}^T, \begin{pmatrix} a_1 & a_2 & a_3 & a_4 & a_5 \end{pmatrix}^T\right) \tag{A.8}$$

The sought-after transformation can be performed by

$$\mathbf{\Sigma}_{\mathbf{E}} = \mathbf{F}_{\mathbf{I}\to\mathbf{E}} \cdot \mathbf{\Sigma}_{\mathbf{I}} \cdot \mathbf{F}_{\mathbf{I}\to\mathbf{E}}^{\mathbf{T}} \tag{A.9}$$

$$\mathbf{\Sigma}_{\mathbf{I}} = \mathbf{F}_{\mathbf{E}\to\mathbf{I}} \cdot \mathbf{\Sigma}_{\mathbf{E}} \cdot \mathbf{F}_{\mathbf{E}\to\mathbf{I}}^{\mathbf{T}} \tag{A.10}$$

For completeness it should be mentioned that

$$\mathbf{F}_{\mathbf{I}\to\mathbf{E}} = \mathbf{F}_{\mathbf{E}\to\mathbf{I}}^{-1} \tag{A.11}$$

and vice versa. This can be proven by substituting (A.9) in (A.10).

Appendix A3: Best-fit Ellipse Adjustment

A best-fit ellipse adjustment can be computed in various ways. A very efficient way is to use a general polynomial of second degree.

$$a_1 \cdot x^2 + a_2 \cdot xy + a_3 \cdot y^2 + a_4 \cdot x + a_5 \cdot y - 1 = 0 \tag{A.12}$$

Because equation (A.12) is linear in its coefficients, an adjustment can be solved in one iteration to determine these coefficients.

If there are n given points with coordinates (x_i/y_i) the corresponding design matrix **B** and vector of the observations **l** for the best-fit adjustment follow as

$$\mathbf{B} = \begin{pmatrix} x_1^2 & x_1 y_1 & y_1^2 & x_1 & y_1 \\ x_2^2 & x_2 y_2 & y_2^2 & x_2 & y_2 \\ & & \vdots & & \\ x_n^2 & x_n y_n & y_n^2 & x_n & y_n \end{pmatrix} \tag{A.13}$$

$$\mathbf{l} = \begin{pmatrix} 1 \\ 1 \\ \vdots \\ 1 \end{pmatrix} \tag{A.14}$$

Using least-squares, the sought-after parameters can be computed by

$$\mathbf{x} = \begin{pmatrix} a_1 & a_2 & a_3 & a_4 & a_5 \end{pmatrix}^T = \left(\mathbf{B}^\mathbf{T}\mathbf{B}\right)^{-1}\mathbf{B}^\mathbf{T}\mathbf{l} \tag{A.15}$$

The parametric from of the ellipse equation (A.2) can be found via conversion, as described in Appendix A1.

Although, this model is the only one which can provide ellipse parameters without iteration, various other models can be found in the literature. The presented model has two disadvantages which can lead to problems in certain applications. First, a general polynomial of second degree describes a conic section and not an ellipse in general. Secondly, the ‘observations’ of the model are zeros. This makes a geometric and stochastic interpretation of the observations impossible.

Appendix A4: Best-fit Polynomial Surface Adjustment

A given three-dimensional point cloud (x_i, y_i and z_i) should be approximated by a polynomial surface which can be written as

$$p(x, y) = a_0 + a_1 \cdot x + a_2 \cdot y + a_3 \cdot x^2 + a_4 \cdot xy + a_5 \cdot y^2 \cdots \tag{A.16}$$

Since equation (A.16) is linear in its coefficients, the adjustment can be solved within one iteration, without approximations for the coefficients. Hence, it is a straightforward matter to derive the required design matrix **B** and vector of observations **l**.

$$\mathbf{B} = \begin{pmatrix} x_1 & y_1 & x_1^2 & x_1 y_1 & y_1^2 & \\ x_2 & y_2 & x_2^2 & x_2 y_2 & y_2^2 & \\ & & \vdots & & & \cdots \\ x_n & y_n & x_n^2 & x_n y_n & y_n^2 & \end{pmatrix} \tag{A.17}$$

$$\mathbf{l} = \begin{pmatrix} z_1 \\ z_2 \\ \vdots \\ z_n \end{pmatrix} \tag{A.18}$$

Using least-squares, the sought-after coefficients can be computed by

$$\mathbf{x} = \begin{pmatrix} a_0 & a_1 & a_2 & a_3 & a_4 & a_5 & \cdots \end{pmatrix}^T = \left(\mathbf{B}^{\mathrm{T}}\mathbf{B}\right)^{-1}\mathbf{B}^{\mathrm{T}}\mathbf{l} \tag{A.19}$$

As can be seen, such a surface approximation is very easy to compute. However, it is well known that polynomial approximations are very sensitive against the degree of the used equation. High order polynomials tend to ‘swing’, especially at regions with few data points. On the other hand low-order approximations may not be able to describe the characteristics of the point cloud. Hence, it is essential to select the appropriate order of the polynomial function.

Appendix B1: Tables of Distortion Errors for Plane White Targets

The following tables contain a tabular summary of the simulated distortion errors for plane white targets which were derived in Chapter 6. Whereas the viewing angle dependency of the distortion errors is nearly irrelevant for retro-reflective targets (compare Table 6.2), there is a high dependency in the case of plane white targets. This is why three different tables for three different viewing angle are listed. At cells where no value is listed, the maximum allowed distortion error cannot be achieved.

	distortion error = 0.01 [pixel]		distortion error = 0.02 [pixel]		distortion error = 0.05 [pixel]	
	c = 20 mm	c = 30 mm	c = 20 mm	c = 30 mm	c = 20 mm	c = 30 mm
k = 0.2	-	0.7	1.7	2.7	3.7	5.2
k = 0.1	1.5	2.3	3.1	4.2	5.7	7.5
k = 0.05	3.2	4.3	5.0	6.7	8.4	11.1
k = 0.02	5.9	7.7	8.6	11.2	13.9	18.1

Table B.1: Maximum target radii of imaged plane white targets for viewing angles up to 10 degree

	distortion error = 0.01 [pixel]		distortion error = 0.02 [pixel]		distortion error = 0.05 [pixel]	
	c = 20 mm	c = 30 mm	c = 20 mm	c = 30 mm	c = 20 mm	c = 30 mm
k = 0.2	-	-	-	-	-	-
k = 0.1	-	-	-	-	3.5	5.0
k = 0.05	-	-	2.4	3.5	7.1	9.5
k = 0.02	3.9	5.3	7.4	9.8	13.1	17.2

Table B.2: Maximum target radii of imaged plane white targets for viewing angles up to 20 degree

	distortion error = 0.01 [pixel]		distortion error = 0.02 [pixel]		distortion error = 0.05 [pixel]	
	c = 20 mm	c = 30 mm	c = 20 mm	c = 30 mm	c = 20 mm	c = 30 mm
k = 0.2	-	-	-	-	-	-
k = 0.1	-	-	-	-	-	-
k = 0.05	-	-	-	-	4.3	5.8
k = 0.02	-	-	4.4	6.4	11.7	15.5

Table B.3: Maximum target radii of imaged plane white targets for viewing angles up to 30 degree

References

Ahn, S. J. and Kotowski, R., 1997. Geometric image measurement errors of circular object targets. *Optical 3-D Measurement Techniques IV* (Eds. A. Gruen and H. Kahmen). Herbert Wichmann Verlag, Heidelberg. 494 pages: 463–471.

Ahn, S.J., Warnecke, H.-J. and Kotowski, R., 1999, Systematic Geometric Image Measurement Errors of Circular Object Targets: Mathematical Formulation and Correction*, Photogrammetric Record*, 16(93), pp 485-502

Baltsavias E. P., Stallmann D., 1991, *Trinocular Vision for Automatic and Robust Three-Dimensional Determination of the Trajectories of Moving Objects*. PERS, Vol. 57, No. 8, pp. 1079 - 1086.

Dold, J., Maas H.-G., 1994, *An application of epipolar line intersection in a hybrid close range photogrammetric system*, IAPRS, Vol. 30/5, Melbourne, pp. 65-70

Dold, J., 1996. Influence of large targets on the results of photogrammetric bundle adjustment. *International Archives of Photogrammetry and Remote Sensing*, 31(B5): 119–123

Fraser, C.S., 1997, *Automation in Digital Close-Range Photogrammetry*, 1st Trans Tasman Surveyors Conference, Fryer J (ed), Proceedings of the 1st Trans Tasman Surveyors Conference, 1: 8.1 - 8.10. Newcastle, NSW: Institute of Surveyors, Australia.

Fraser, C.S. and Shao, J., 1997, *An Image Mensuration Strategy for Automated Vision Metrology*, Optical 3D Measurement Techniques IV, Heidelberg, Germany: Wichmann Verlag, 187-197

Gruen A., Baltsavias E. P., 1988, *Geometrically Constrained Multiphoto Matching*, PERS, Vol. 54, No. 5, pp. 633 - 641.

Ho, C.-S., 1983, Precision of Digital Vision Systems. IEEE Transactions on Pattern Analysis & Machine Intelligence, Vol. PAMI-5, No. 6, 593-601

Kager H., 1981, *Bündeltriangulation mit indirekt beobachteten Kreiszentren*. Geowissenschaftliche Mittelungen Heft 19, Institut für Photogrammetrie der Technischen Universität Wien

Kraus, K., 1996, *Photogrammetry*, Volume 2, Advanced Methods and Applications, with contributions by J. Jansa and H. Kager, 4th edition, Dümmler/Bonn.

Luhmann, T., 2000, *Nahbereichsphotogrammetrie*, Grundlagen, Methoden und Anwendungen, Herbert Wichmann Verlag, pp 408-413

Maplesoft, 2004, Web site: http://www.maplesoft.com/ (accessed October 2004)

Mikhail, E.M., 1983, Photogrammetric Target Location to Sub-Pixel Accuracy in Digital Images. 39th Photogrammetric Week., Stuttgart, Sept. 19-24, 25 pages.

Mikhail, Edward M. and Ackermann, F., 1996, *Observations and Least Squares*, IEP-A Dun-Donnelley Publisher

Otepka, J., 2001, Algorithms and their Implementation in an Automated Close-Range Photogrammetric System, Master Thesis, University of Technology Vienna

Otepka, J., Hanely, H.B., Fraser, C.S, 2002, *Algorithm Developments for Automated Off-Line Vision Metrology*, Proceedings of the ISPRS Commission V Symposium 2002

Photometrix, 2004, Web site: http://www.photometrix.com.au (accessed October 2004).

Shortis, M.R., Clarke, T.A. and Short, T., 1994*, Comparison of some techniques for the subpixel location of discrete target images*, SPIE Proceedings Vol. 2350, Paper #25

Trinder, J.C., 1989. *Precision of digital target location*. Photogrammetric Engineering & Remote Sensing, Vol. 55, No 6, June, pp. 883-886

Trinder, J.C., Jansa, J. and Huang, Y., 1995, *An assessment of the precision & accuracy of methods of digital target location*. ISPRS Journal of Photogrammetry and Remote Sensing, 50(2): 12-20

Zumbrunn, R., 1995, *Systematic pointing errors with retroreflective targets*. Optical Engineering, 34(9), pp. 2691–2695.

Curriculum Vitae

Johannes Otto Otepka

Date of Birth: 29.10.1975 - Vienna

Education

1981-1985	Volksschule Unterstadt in Imst
1985-1993	BRG in Imst
15.6.1993	Reifeprüfung
Since 1993	"Vermessung und Geoinformation" at the University of Technology Vienna
9.6.1997	1. Diplomprüfung
2000-2001	Exchange semester for Diploma thesis at the Melbourne University, Australia
29.10.2001	2. Diplomprüfung
Since December 2002	PhD at the University of Technology Vienna and the Melbourne University "Precision Target Mensuration in Vision Metrology"

Working Experience during Studies

1994, 95 and 97	*Vermessung AVT, Imst*: cadastral and technical surveying
1995, 96 and 97	*TU, Vienna:* tutor for "Structured Programming in Turbo Pascal"
1996	*ÖAI (**Ö**sterreichisches **A**rchäologisches **I**nstitut), Turkey:* surveying at the archaeological side Ephesos
1995-1997	*ÖH (**Ö**sterreichische **H**ochschülerschaft), Vienna:* "Studienrichtungsvertreter"
1997-2000	*ÖH*, *Vienna:* member of the "Studienkommission"
1998	*Vermessungsbüro Bauer, Linz:* cadastral and rail track surveying
1999 and 2000	*IDC-EDV, Imst:* programming adjustment module for surveying software *Geosi*
1999	*IPF (**I**nstitut für **P**hotogrammetrie und **F**ernerkundung), Vienna:* self-employed programming for the "Berghöfekataster" project in conjunction with the BEV (**B**undesamt für **E**ich- und **V**ermessungswesen).

Professional Records

2001-2002 Self-employed programming and research

- *IDC-EDV:* adjustment module for surveying software *Geosi*
- *IPF and BEV:* continuing project of the "Berghöfekataster" project
- *Melbourne University:* further developments for the digital close-range photogrammetric software *Australi*s

June 2002-November 2002 *IPF, Vienna*: interface programming for *SCOP* (digital terrain data program) and the Oracle® Spatial Database